UNIVERSITÀ DEGLI STUDI DI MILANO

Ph.D. school in Physics, Astrophysics and Applied Physics

Department of Physics

XXIX Cycle

Radionuclides for medicine

Excitation functions for the production of ^{99m}Tc, ^{89}Zr and ^{103}Pd

Scientific disciplinary sector FIS/07

Academic Advisor:

Prof. Flavia M. Garlandini Groppi

Director of the Doctoral School:

Prof. Francesco Ragusa

Candidate:

Simone Manenti

Academic Year 2016-2017

Contents

Introduction **1**
Radionuclides in medicine 1
Nanotechnology and nanomedicine 3
Aim of the Ph.D. work 4

1 Elementary nuclear reactions theory **7**
1.1 Energetics of nuclear reactions 7
1.1.1 The mass energy 8
1.1.2 The Coulomb barrier 11
1.1.3 Summary 14
1.2 Mechanisms of nuclear reactions 15
1.2.1 Scattering reactions 15
1.2.1.1 Elastic scattering reactions 16
1.2.1.2 Inelastic scattering reactions 16
1.2.2 Compound Nucleus and Direct reactions 16
1.2.2.1 Compound Nucleus reactions 17
1.2.2.2 Direct reactions 18

2 Fundamental physical, radiochemical and quantitative informations **19**
2.1 Cross-section 19
2.1.1 Nuclear cross-section and irradiation yield 22
2.2 Stopping power and range 24
2.3 Thin target yield 32
2.4 Thick Target Yield 32
2.5 γ-spectrometry with HPGe detectors 34
2.5.1 Efficiency calibration 34
2.5.1.1 Absolute full-energy peak efficiency 35
2.6 Experimental activity, cross-section and yield evaluation 37
2.7 Main radiochemical parameters 38
2.7.1 A_S, C_A and IDF 38
2.7.1.1 A_S specific activity 38
2.7.1.2 C_A activity concentration 39

2.7.1.3 *IDF*: isotopic dilution factor 40
2.7.2 Radiopharmaceutical preparation 40

3 Irradiation facilities 43
3.1 Ispra cyclotron 43
3.1.1 Cyclotron Set-up 43
3.2 ARRONAX cyclotron 47
3.2.1 Cyclotron Set-up 47
3.3 Beam profile 47
3.3.1 Cyclone 50
3.3.2 Beam "picture" 52

4 The excitation functions of ^{100}Mo(p,x)^{99}Mo and ^{100}Mo(p,2n)^{99m}Tc nuclear reactions 55
4.1 Introduction 55
4.2 Experimental 56
4.3 Results and Discussion 58
4.3.1 ^{99}Mo 60
4.3.2 Determination of the absolute intensity 140.511 keV γ-ray emission of ^{99}Mo 61
4.3.3 ^{99m}Tc 62
4.3.4 Thin and Thick Target Yield 65
4.3.5 Radionuclidic impurities: ^{96}Nb, ^{97g,cum}Nb and ^{99g}Tc 68
4.3.5.1 ^{99g}Tc 69
4.4 Conclusions 72

5 The excitation functions of the ^{89}Y(d,2n)^{89}Zr nuclear reaction 73
5.1 Introduction 73
5.2 Experimental 74
5.3 Results 77
5.3.1 ^{89}Y(d,2n)^{89}Zr 79
5.3.2 ^{89}Y(d,3n)^{88}Zr 79
5.3.3 ^{89}Y(d,x)^{88}Y 80
5.4 Conclusions 80

6 The excitation function and yield for the ^{103}Rh(d,2n)^{103}Pd nuclear reaction 83
6.1 Introduction 83
6.2 Experimental 84
6.3 Results 89
6.3.1 ^{103}Rh(d,2n)^{103}Pd 89
6.3.2 ^{103}Rh(d,4n)^{101}Pd 94
6.3.3 ^{103}Rh(d,x)^{102m,g}Rh 94
6.3.4 ^{103}Rh(d,x)^{101m,g}Rh 95
6.3.5 ^{103}Rh(d,x)^{100g,cum}Rh 97
6.3.6 ^{103}Rh(d,2p)^{103}Ru 98
6.3.7 Specific Activity for ^{103}Pd production 98
6.4 Conclusions 101

Summary of the conclusions **102**

References **105**

List of Figures **115**

List of Tables **119**

Introduction

Radionuclides in medicine

Radioactivity, discovered by Henri Becquerel in 1896, has revolutionized the whole scientific world and, especially, it played a fundamental role in the life sciences starting from the last century until today. In particular, it is possible to say that the impact of radioactivity on Medicine was extraordinary and it is precisely in Nuclear Medicine, a well established branch of medicine, where radioactivity had, and still has, its most important applications.

In fact, radioactivity is widely used as diagnostic and therapeutic powerful tool in medicine. The reason for this importance is very simple: in the ideal physiological experiment the subject or system should not be disturbed. Radioactive tracers, due to their sensitivity and due to the fact that isotopic labelling does not significantly alter the chemical properties of the molecule, provide the perfect tool for this approach. Thus, this is the reason why it didn't take long, after the discovery of radioactivity until it was used in life sciences [Stöcklin et al., 1995].

Furthermore, radiation therapy has gained a greater and greater important role. Actually, it is mostly performed using external beams (i.e. electrons, x-rays, γ-rays from radioactive sources or hadrons). In addition to external radiation therapy, some radionuclides are used internally to achieve the therapeutic effect. This could involve introducing a radionuclide in a given part of the body either mechanically or via a biochemical pathway. The mechanical introduction takes place through injection of conglomerates or colloids or as solids in the form of seeds or stents: ^{192}Ir implants are used in wire form to treat head, neck, ovarian, and breast cancers, ^{125}I and ^{103}Pd implants are used to treat malignant tumours of the prostate during their incipient phases. This form of therapy is often known as brachytherapy.

The use of a biochemical pathway to deliver a therapeutic radioisotope to a spe-

cific organ is termed as endoradiotherapy or targeted radionuclide therapy. This type of radiotherapy is a unique cancer treatment modality. It is systemic and non-invasive; it delivers soluble radioactive substances to tissues either by ingestion or via intravenous, intraperitoneal, or intratumoural administration of tumour targeting carriers (such as antibodies or biocompatible materials). In systemic radiotherapy, tumour targeting can be achieved by exploiting metabolic processes (e.g., ^{131}I for thyroid cancer, ^{32}P for polycythaemia vera, ^{131}I metaiodobenzylguanidine for neuroblastoma), extracellular mechanisms (e.g., boneseeking agents such as radiolanthanide complexes with ligands bearing phosphonate groups, different radiolabelled cells), or cell surface receptors (e.g., hormones, peptides, antibodies, aptamers, liposomes, dendrimers). These techniques represent a new paradigm for cancer treatment, and combine developments in molecular biology, nanotechnology, nanomedicine, and radiopharmacy [Dearling and Pedley, 2007]. So target radionuclide therapy combines the specificity of cancer cell targeting with the anti-tumour effects of ionising radiation.

The major criteria for the choice of a radionuclide for endotherapeutic use are suitable decay characteristics and suitable biochemical reactivity. As regards decay properties, the desired half-life is between $6\,h$ and $7\,d$ and the emitted corpuscular radiation should have a suitable linear energy transfer (LET) value and range in the tissue. The ratio of non-penetrating to penetrating radiation should be high. The daughter should be short-lived or stable. As regards biochemical reactivity, the situation is similar to that for diagnostic radiopharmaceuticals. However, the stability of the therapeutical is demanded over a much longer period than that in the case of a diagnostic pharmaceutical. The basis for successful endoradiotherapy thus incorporates:

- good and selective concentration and prolonged retention of the radiotherapeutical in the tumour; typically, radiononmetals are excreted from the cells again, while radiometals are trapped in the lysosomes, leading to longer tumour retention times [Koppe et al., 2004].

- minimum uptake in normal tissue.

As a result of the above mentioned criteria, the choice falls on about 30 radionuclides [Qaim, 2016] for which two important parameters are the biological half-life, correlated to the retention, and the ranges of the emitted particles are suitable.

Unlike conventional cancer therapies, targeted radionuclide therapy has the potential to simultaneously eliminate tumour at the primary site and tumour that

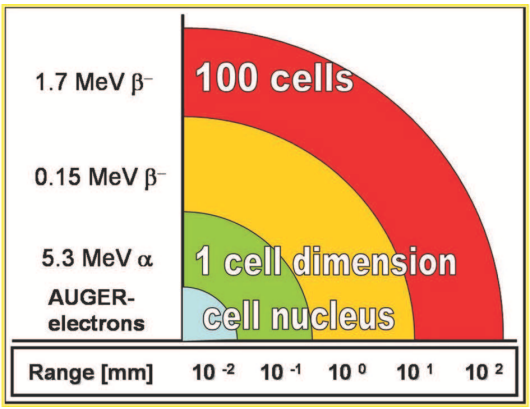

Figure 1: Correlation between type and energy of corpuscular radiation and the range in tissue [Stöcklin et al., 1995].

has spread throughout the body (metastases), concentrating the radiation energy in the tissues of interest without affecting surrounding healthy tissues.

The ranges of different types of emitted corpuscular radiation in the tissue are shown in Figure 1. The Auger electrons have a range of about 10 μm and can have a therapeutical effect only if they reach the cell nucleus, e.g. by bringing the radioactive source atom to the DNA. The α-particles, on the other hand, have a range of about 100 μm and can have a therapy effect already if they reach the cell membrane, e.g. by attachment of the α-emitter to a receptor ligand. The β^--particles have ranges of about 1 mm and more, depending upon their energies. They can lead to therapeutical effects even if they reach the cell environment. Evidently, achieving the therapy effect with Auger electrons and α-particles involves a very subtle approach and demands great skills in biochemistry, radiopharmacology and radiotherapeutical production and application. In the case of β^--particles, the therapeutic applications have been more straightforward, though not very specific.

In endoradiotherapy, the radioactive decay data thus play a very important role. In particular, a knowledge of the energy and intensity of the ionising radiation is crucial. The effect of low-energy but high intensity electrons, emitted following EC and IT, is not negligible. For widely used therapeutic radioisotopes therefore all sources of secondary electrons must be taken into account.

Nanotechnology and nanomedicine

Over the last few decades, nanotechnology has been frequently used for various applications in different fields such as agriculture, textiles, forensic science, elec-

tronics, the space industry, and medical therapeutics.

Nanomedicine can be defined as the design of diagnostic and/or therapeutic devices on the nanoscale, the purpose being to improve transport and delivery of active species within biological systems for the treatment, prevention, and diagnosis of disease.

Radiolabelled nanoparticle-based contrast agents are increasingly being used as a valuable tool in biomedical research. Compared to conventional contrast agents, nanoparticles promise to improve in vivo detection and enable more efficient targeting due to increased circulation times, evasion of clearance pathways, and multimeric binding capacity [Prokop and Davidson, 2008]. In fact, nanoparticles are have sizes of less than 100 nm and they selectively increase the localisation and concentration of radiopharmaceuticals in the tumour: the small size enables them to penetrate the discontinuous endothelium lining the vasculature of tumour tissues and accumulate there due to impaired lymphatic drainage and the enhanced permeability and retention effect effect [Ngoune et al., 2016]. In this way, nanocarriers are able to carry high radioactive doses to the target cells, resulting in effective tumour cell killing, even with relatively low levels of target receptor expression. Furthermore, nanoparticles have high loading capacities, and, unlike antibodies for example, they can carry more than one type of radioisotope: they are particularly suited to targeted cancer therapy that requires a combination of radionuclides emitting different energies.

Liposomes are small vesicles in which one or more concentric lipid bilayers enclose discrete aqueous spaces; they are spontaneously formed when (phospho)lipids are suspended in aqueous media. With respect to the radiolabelling strategy used to incorporate/attach the radionuclide into/to the liposomes: the radionuclide can be trapped in the inner aqueous cavity of the liposomes, trapped in the lipid membrane, or attached to the surface of the liposome.

Aim of the Ph.D. work

In this work, I have decided to investigate the production routes of ^{99m}Tc, ^{89}Zr and ^{103}Pd.
From a chronological point of view, my work started with the analysis of the optimization of the production of ^{99m}Tc, then I worked on ^{103}Pd and, at the end, on ^{89}Zr. Here, in this thesis, I decided to present them in a different sequence:

for first a well known diagnostic nuclide (^{99m}Tc, Chapter 4), a promising β^+-emitter radionuclide for labelling monoclonal antibodies, bio-distribution studies, and immuno-PET imaging (^{89}Zr, Chapter 5) and then a nuclide used for cancer brachytherapy that has innovative strategy of use under development, for example ^{103}Pd@Au nanoparticles distributed in the diseased tissue (^{103}Pd, Chapter 6).

I decided to focus on these radionuclides because:

- technetium-99m is considered the "workhorse" of radiopharmaceutical imaging. Nearly 80 % of nuclear medicine imaging procedures are currently performed with ^{99m}Tc-labelled compounds. ^{99m}Tc has a favourable γ-energy (141 keV), which penetrates soft tissue but simultaneously delivers relatively low radioactive doses to the patient or experimental animal. In addition, it has a favourable half-life of 6.02 h and well-known coordination chemistry. In recent years there was a worldwide shortage of ^{99}Mo/^{99m}Tc, which is produced in highly enriched uranium targets via fission of ^{235}U in nuclear reactors. This shortage boosted the interest in verifying alternative routes. One method is the cyclotron production of ^{99m}Tc via the nuclear reaction ^{100}Mo(p,2n)^{99m}Tc;

- zirconium-89 has 23 % positron branching and emits a low-energy positron ($E_{\beta^+}, max = 0.897$ MeV), which is favourable for achieving high spatial resolution in imaging studies. As I said before, its relatively long half-life (78.4 h) makes it a useful candidate for labelling monoclonal antibodies, bio-distribution studies, and immuno-positron emission tomography (PET) imaging. Furthermore, it is possible to prepare simultaneously paramagnetic and pharmaceutical probes of ^{89}Zr-labelled liposomes for simultaneous PET and magnetic resonance tumour imaging. Cross-sections of the proton-induced reactions on ^{89}Y were measured many times and the experimental data are relatively consistent. In contrast, the excitation functions of the deuteron-induced nuclear reactions are rather scattered and I have decided to re-measure in detail excitation functions of the ^{89}Y(d,x) reactions up to 18 MeV;

- palladium-103 is a radionuclide having a half-life of 16.99 d and decaying 100 % by the electron capture (EC), which is suitable for brachytherapy, particularly for the prostate and eye cancer therapy. With the rapid development of nanoscience and nanotechnology, it becomes appealing to make injectable nano-scale brachytherapy seeds: a new strategy under development to replace millimetre-size implants, consist in injecting radioactive NPs in the affected

tissues. Nowadays, the development of ^{103}Pd@Au NPs distributed in the diseased tissue, could increase the uniformity of treatment (compared with massive seeds), while enhancing the radiotherapeutic dose to the cancer cells (through Au-mediated radiosensitisation effect). Nowadays the most widely used accelerator production method is based on high-flux, 18 MeV proton irradiation of a ^{103}Rh target in cyclotrons. The use of a deuteron beam appears to be attractive for the production of this radionuclide since the (d,2n) reaction cross section in the medium to high mass region is generally higher than that of the (p,n) reaction.

The Chapters 1–3 will introduce the experimental parts that are described in the later ones: I will present in Chapter 1 an elementary nuclear reactions theory, in Chapter 2 the physical quantities that will be used in the Chapters 4–6 and in Chapter 3 a description of the irradiation facilities.

Chapter 1

Elementary nuclear reactions theory

A nuclear reaction is a process in which a nucleus reacts with another nucleus, an elementary particle, or a photon to produce, within a time limit of $10^{-12}\,s$ or less, one or more other nuclei, and possibly other particles. The variety of reactions that have been studied is bewildering, as may be readily perceived from a consideration of the variety of bombarding particles available. They include neutrons, protons, photons, electrons, various mesons and nuclei ranging from deuterons to uranium nuclei.

The scientist who first discovered the phenomenon of nuclear reactions was Rutherford, in 1919, when he observed that in the bombardment of nitrogen with the $7.69\,MeV$ α particles of $RaC'(^{214}Po)$, scintillations of a zinc sulphide screen persisted even when enough material to absorb all the α particles was interposed between the nitrogen and the screen. Further experiments proved the long-range particles causing the scintillation to be protons, and the results were interpreted in terms of a nuclear reaction between α particles and nitrogen producing oxygen and protons [Friedlander et al., 1981, Rutherford, 1919].

From that moment on, a series of new nuclear reactions were discovered and these led us to better understand the infinitely small world of the nuclei.

1.1 Energetics of nuclear reactions

Reactions between an atomic nucleus and another particle are called, as said before, nuclear reactions. In some such reactions, new nuclei are formed (*nuclear transmutations*); in others, the original nucleus is excited to a higher energy state (*inelastic scattering*); in a third situation, the nucleus is unchanged (*elastic scattering*) (see

§1.2). In any case, for a nuclear reaction to occur some *conservation laws* must be valid [Choppin et al., 2002]:

- the conservation of total energy: $\Delta E = 0$
- the conservation of linear momentum: $\Delta p = 0$
- the conservation of total charge: $\Delta Z = 0$
- the conservation of mass number: $\Delta A = 0$
- the conservation of spin: $\Delta I = 0$.

In this specific case I am especially interested in the first two quantities. So let us analyse them.

1.1.1 The mass energy

Most nuclear reactions are studied by inducing a collision between two nuclei, where one of the reacting nuclei is at rest (the *target* nucleus) while the other nucleus (the *projectile* nucleus) is in motion. Such nuclear reactions can be described generically as:

Projectile P + Target T → emitted particles X and residual nucleus R.

For example, the first reaction discovered, as discussed above, might occur by bombarding ^{14}N with α particles to generate an emitted particle, the proton, and a residual nucleus, the ^{17}O. A shorthand way to denote such reaction is, for the general case,

$$T(P,X)R$$

or for the specific example

$$^{14}N(\alpha,p)^{17}O.$$

For the general nuclear reaction $T(P,X)R$, neglecting the electron binding energies, the energy balance in the reaction is:

$$m_P c^2 + T_P + m_T c^2 = m_R c^2 + T_R + m_X c^2 + T_X$$

where T_i is the kinetic energy of the ith particle and m_i represents the mass of the ith species.

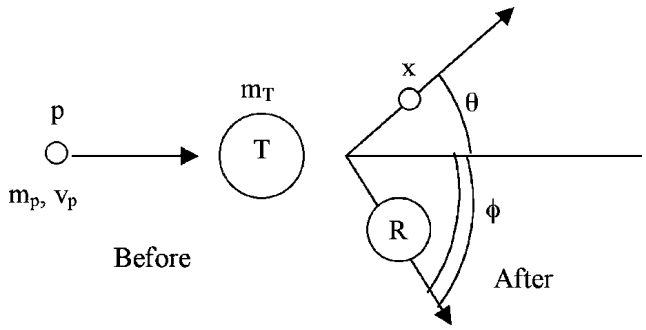

Figure 1.1: Schematic diagram of a nuclear reaction.

The *Q-value* of the reaction [Loveland et al., 2006] is defined as the difference in masses of the product and the reactants, that is:

$$Q = [m_P + m_T - (m_X + m_R)]c^2 = T_X + T_R - T_P \qquad [MeV], \tag{1.1}$$

and in general is:

$$Q = \left[m_P + m_T - \left(\sum_i m_{X_i} + \sum_i m_{R_i}\right)\right]c^2.$$

Note that if Q is positive, the reaction is *exoergic*, while if Q is negative, the reaction is *endoergic*. A necessary, but not sufficient, condition for the occurrence of a nuclear reaction is:

$$Q + T_P > 0.$$

This equation suggests that Q is an important quantity for nuclear reactions.

However, I can show, using conservation of momentum, that only T_X and the angle θ of X with respect to the direction of motion of P suffice to determine Q in these two-body reactions.

In a laboratory system, a typical nuclear collision can be depicted as shown in Figure 1.1. Conserving momentum in the x direction, it is possible to write:

$$m_P v_P = m_X v_X \cos\theta + m_R v_R \cos\phi; \tag{1.2}$$

conserving the momentum in the y direction:

$$0 = -m_X v_X \sin\theta + m_R v_R \sin\phi \tag{1.3}$$

where m_i and v_i are the mass and the velocity of the ith species [Krane, 1988].

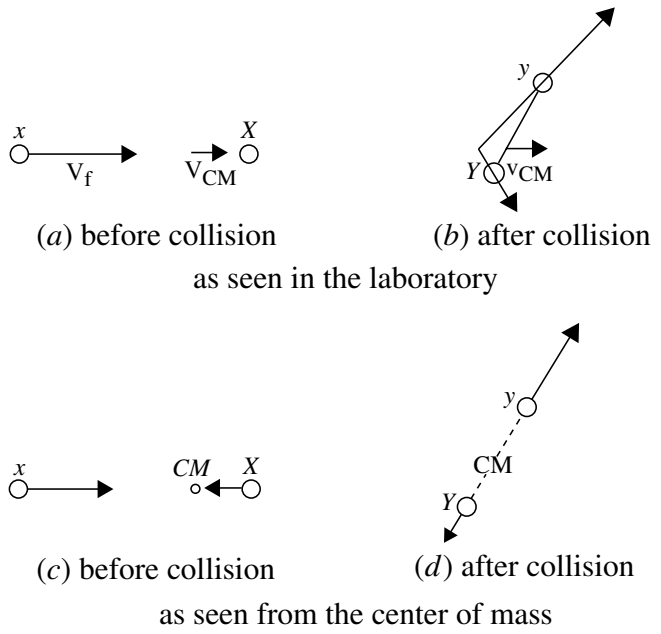

Figure 1.2: Schematic view of a nuclear reaction in the laboratory and center of mass system.

But, the momentum is $p = mv = (2mT)^{1/2}$, so it is possible to substitute in the equations (1.2) and (1.3) and obtain:

$$(m_P T_P)^{1/2} - (m_X T_X)^{1/2} \cos\theta = (m_R T_R)^{1/2} \cos\phi \quad (1.4a)$$

$$(m_X T_X)^{1/2} \sin\theta = (m_R T_R)^{1/2} \sin\phi. \quad (1.4b)$$

If we now square the equations (1.4), sum them up and solve them for T_R, we have:

$$T_R = \frac{m_P T_P - 2(m_P T_P m_X T_X)^{1/2} \cos\theta + m_X T_X}{m_R} \quad (1.5)$$

Finally, inserting the equation (1.5) in the (1.1), we can get the so-called Q *equation*:

$$Q = T_X\left(1 + \frac{m_X}{m_R}\right) - T_P\left(1 - \frac{m_P}{m_R}\right) - \frac{2}{m_R}(m_P T_P m_X T_X)^{1/2} cos\theta.$$

The Q equation shows that if we are able to measure the kinetic energy of the emitted particle X and the angle at which it is emitted in a reaction and we presume to know the identities of the reactants and of the products involved in the reactions, we can determine the Q value of the reaction itself.

Now, in order to better understand how nuclear reactions work and, in particular, the quantities that play an important role, let us consider the same reaction as described in the *center of mass* (cm) coordinate system (Fig. 1.2). In such system, the total momentum of the particles is zero, before and after the collisions. Thus, the kinetic energy of the center of mass is:

$$T_{cm} = \frac{(m_P + m_T)v_{cm}^2}{2} \qquad [MeV],$$

where $v_{cm} = v_P m_P/(m_P + m_T)$ is the speed of the center of mass. We can now write the kinetic energy of the cm as:

$$T_{cm} = \frac{1}{2}(m_P + m_T)\left[\frac{m_P v_P}{m_P + m_T}\right]^2 = \frac{1}{2}m_P v_P^2\left(\frac{m_P}{m_P + m_T}\right) = T_{lab}\left(\frac{m_P}{m_P + m_T}\right)$$

where T_{lab} is the kinetic energy in the lab system before the reaction.

The kinetic energy carried in by the projectile, T_{lab}, cannot be fully dissipated in the reaction. Instead, an amount T_{cm} must be carried away by the center of mass. Thus, the available energy that must be dissipated is $T_{lab} - T_{cm} \equiv T_0$. The energy available for the nuclear reaction is $Q + T_0$; so, to make the reaction work, the sum $Q + T_0$ must be greater than or equal to zero. Finally, rearranging a few terms of the previous equations [Ehmann and Vance, 1991], the condition to make the reaction occur is:

$$T_P \geq -Q\frac{m_P + m_T}{m_T} \equiv E_{th} \qquad [MeV]; \tag{1.6}$$

the minimum kinetic energy that the projectile must have to make the reaction work is called the *threshold energy* E_{th}. This is another important parameter in order to comprehend the behaviour of a nuclear reaction.

1.1.2 The Coulomb barrier

In the previous section we concluded that a reaction occurs if the projectile has a kinetic energy greater than the threshold energy of the reaction itself. This is not completely true. In fact, if the projectile is a positively charged particle (i.e. protons, alphas etc...), it experiences the Coulomb repulsion caused by the nucleus.

This means that the incoming projectile must possess sufficient kinetic energy to overcome any repulsion [Choppin et al., 2002]. Let us understand the phenomenon by using an example: consider a reaction of a positively charged particle (m_P, Z_P, v_P) with a target atom $(m_T, Z_T, v_T \approx 0)$. We can now make two simpli-

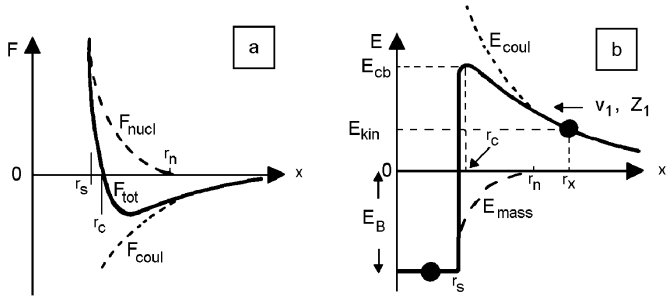

Figure 1.3: Forces (a) and energy (b) conditions when a charged projectile (Z_P, v_P) reacts with a target nucleus.

fying assumptions: the target nucleus is in the center of the coordinate system and relativistic mass correction can be neglected. Since both projectile and target have positive charges, they must repel each other according to the Coulomb law:

$$F_{Coul} = \frac{1}{4\pi\epsilon_0}\frac{Z_P Z_T \mathbf{e}^2}{x^2}$$

where ϵ_0 is $8.854187817... \cdot 10^{-12} F \cdot m^{-1}$ [Mohr et al., 2015]. This force is shown as a function of the distance between the particles in Figure 1.3. At a distance greater than the nuclear radius r_n only the Coulomb repulsive force is in operation; however, for distances less than r_n both the attractive nuclear force F_{nucl} and the repulsive Coulomb act upon the system. Thus, the total force (i.e. the solid line in the Figure) is given by the sum of these two forces: $F_{tot} = F_{nucl} + F_{Coul}$. At some particular distance called, r_c the forces balance each other and, at shorter distances $(x < r_c)$, the attractive nuclear force dominates. The distance r_c is known as the Coulomb radius; but to be more precise, r_c is the sum of the projectile and target radii.

In Figure 1.3 we can observe the energy condition of the system when a charged particle reacts with a target nucleus; at long distances from the target nucleus the kinetic energy of the projectile is decreased due to the Coulomb repulsion. Since for such distances the nuclear force can be neglected, the energetic equation can be written as:

$$E^0_{kin} = E_{kin} + E_{Coul},$$

where E^0_{kin} is the original kinetic energy of the projectile and E_{Coul} is the Coulomb potential energy, which depends on the distance:

$$E_{Coul} = -\frac{1}{4\pi\epsilon_0}\frac{Z_P Z_T \mathbf{e}^2}{x} \qquad [J].$$

As the projectile approaches the target nucleus, the Coulomb repulsion causes the potential energy to increase as the kinetic energy of the particle decreases. If the kinetic energy reaches a value of zero at any distance greater than r_c, the particle is reflected away from the nucleus before it is close enough to experience the attractive nuclear force. Thus, a necessary condition for charged projectiles to cause nuclear reactions is that E^0_{kin} exceeds the Coulomb barrier height E_{cb}:

$$E_{cb} = \frac{1}{4\pi\epsilon_0}\frac{Z_P Z_T \mathbf{e}^2}{r_c}.$$

This is the general formula for the calculation of the Coulomb barrier. It is possible to express the radius as a function of the mass number of the particles; experimentally, the nuclear radius is given by $r = r_0 A^{1/3} fm$. But, in nuclear physics r_0 assumes three different values depending on which nuclear radius constants (i.e. r_s, r_c, r_n) I'm interested in. Experiments have indicated that the values of r_0 are approximately 1.1 for the radius r_s of constant nuclear density, 1.3 for the Coulomb radius r_c and 1.4 for the nuclear radius r_n, which include surface effects.

Now, in order to calculate the Coulomb barrier let us use a model in which the target nuclei and the projectile are just touching so that r_c is taken as the sum of the radii of the projectile and the target nucleus [Choppin et al., 2002]. With this model, the Coulomb barrier energy is shown by the equation:

$$E_{cb(min)} = 1.109(A_P + A_T)\frac{Z_P Z_T}{A_T(A_P^{1/3} + A_T^{1/3})} \qquad [MeV]. \tag{1.7}$$

$E_{cb(min)}$ is the minimum energy that a projectile of mass A_P and charge Z_P must have in order to overcome the Coulomb barrier of a target nucleus of mass A_T and charge Z_T in a collision.

It is important to note that the barrier exists both for the incoming projectile and the emitted particle if the latter is charged. For this reason, a charged particle has to be excited to a rather high energy level inside the nucleus before it can leak through the barrier with appreciable probability.

Finally, a last consideration must not be forgotten: it has been found that nuclear reactions sometimes occur at energy level less than that required by the Coulomb barrier. This behaviour relates to the wave mechanical nature of the particles involved in a nuclear reaction. As a projectile approaches a target nucleus, the probability that there will be overlapping and, hence, interaction in their wave functions, increases. This phenomenon is well known as the *tunnel effect* or *quantum-mechanical tunnelling*, but it is important to stress that the probability of this phenomenon occurring drops rapidly as the energy of the incoming particle

decreases, compared to the value of the Coulomb barrier.

1.1.3 Summary

In the previous sections (see §1.1.1 and §1.1.2) it was shown that a reaction occurs only if the kinetic energy of the incoming projectile is:

- larger than or equal to the threshold energy;
- in case of positive charge particle, not less than the Coulomb barrier.

I have also said that a reaction with a charged particle may happen even if the kinetic energy is lower than the Coulomb barrier, thanks to the tunnel effect. So, how can we describe the behaviour of the probability function that a nuclear reaction occurs depending on the values of the threshold energy and the Coulomb barrier? In order to understand the general behaviour of this function, we must consider two different situations: the threshold energy is lower than the Coulomb barrier or vice-versa.

In the first case (Fig. 1.4(a)) we see that in the energy interval between the E_{th} and the E_{cb} the reaction occurs only due to the tunnel effect and so the probability is very low. However, just after the Coulomb barrier the probability increases rapidly to the maximum value.

In the second case (Fig. 1.4(b)), instead, the probability is zero until the E_{th} and then increases rapidly to the maximum value.

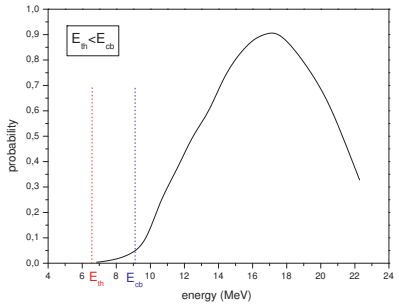

(a) Example of probability function behavior for $E_{th} < E_{cb}$.

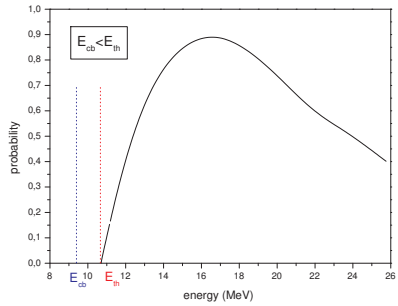

(b) Example of probability function behavior for $E_{th} > E_{cb}$.

Figure 1.4: Example of probability function behavior: in (a), $E_{th} < E_{cb}$, it is shown how the function assumes low values in the interval between the theshold energy and the Coulomb barrier where the tunnel effect dominates. For higher energies, the function increases more rapidly. In (b), $E_{cb} < E_{th}$, it is possible to see that the function starts from zero and reaches the maximum very rapidly.

What we have just shown are the very general cases for these two types of reactions; of course, the probability function may have more than one maximum value but what we wanted to stress is the behaviour of this function around the threshold energy of the Coulomb barrier.

1.2 Mechanisms of nuclear reactions

Nuclear reactions can occur via different mechanisms: in Figure 1.5 the relationships between the various nuclear reaction mechanisms are illustrated.

Considering a general nuclear reaction T(P,X)R, two broad groups of particle-induced nuclear reactions may be identified: the ones in which the nuclei X and R may be identical to P and T and all the others. Let us analyse these two families focusing our attention on the second one.

1.2.1 Scattering reactions

Scattering reactions are a type of reaction in which an incoming particle is deflected, or scattered away from the target nucleus. This interaction results in a change of direction for the projectile involved, but no change in the identity of either the incident particle or the target nucleus. Scattering reactions are either elastic or inelastic [Ehmann and Vance, 1991].

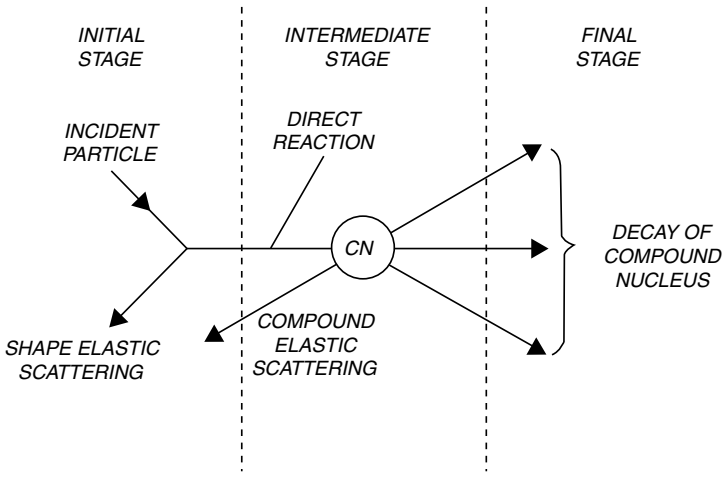

Figure 1.5: Conceptual view of the stages of a nuclear reaction [Weisskopf, 1957].

1.2.1.1 Elastic scattering reactions

In *elastic scattering*, the projectile-target system has essentially the same total kinetic energy before and after the interaction (i.e. $Q = 0$). Small kinetic energy losses, such as those to atomic or molecular excitations, may slightly alter the energy balance. The general notation for elastic scattering is:

$$T(P,P)T.$$

What I have just explained suggests that in a strict sense, elastic scattering is not a real nuclear reaction, but merely a "billiard-ball" scattering event.

1.2.1.2 Inelastic scattering reactions

In *inelastic scattering*, part of the kinetic energy of the projectile is transferred to the target nucleus, as excitation energy, without changing the values of A and Z of either the target or the projectile. The excitation energy can be emitted as γ photon (route a) or remanis in the target atom (route b):

$$P + T \quad \begin{cases} a \longrightarrow & P + T + \gamma \\ b \longrightarrow & P + T^* \end{cases} \qquad Q < 0$$

The latter exists in an excited state and may transform to the ground state quite rapidly or may exist for a measurable time as an isomer [1]. In any case, the energy relationships in inelastic scattering are the same as for other nuclear reactions.

1.2.2 Compound Nucleus and Direct reactions

When a projectile approaches a target nucleus, a two-body collision may occur between the projectile and some nucleon of T, raising the nucleon of T to an unfilled level (Fig. 1.5). If the struck nucleon leaves the nucleus, a direct reaction is said to have occurred; if the struck nucleon does not leave the nucleus, further two-body collisions may happen, and eventually the entire kinetic energy of the projectile may be distributed between the nucleons of the $P + T$ combination leading to the formation of a compound nucleus CN (Fig. 1.5).

[1] Any of two or more nuclei with the same mass number and atomic number that have different radioactive properties and can exist in any of several energy states for a measurable period of time.

1.2.2.1 Compound Nucleus reactions

Most low-energy nuclear reactions proceed via formation of the compound nucleus which model was proposed in 1936 by Niels Bohr [Bohr, 1936]. As an example of this type of reaction, let us consider the first nuclear reaction discovered by Rutherford:

$$^{14}_{7}N + ^{4}_{2}He \rightarrow [^{18}_{9}F]^{*} \rightarrow ^{17}_{8}N + ^{1}_{1}H$$

where the compound nucleus of fluorine is in square brackets to indicate its transitory nature and marked with an asterisk to indicate that is excited.

Let us now study this model a little closer: if the projectile has an incoming kinetic energy E^0_{kin} greater than $E_{cb(min)}$, the attractive nuclear force dominates and the particle is absorbed by the target nucleus. This means that the projectile adds its kinetic energy and binding energy to the target nucleus so that the compound nucleus is in an excited state and the nuclear excitation energy E_{exc} can be expressed as:

$$E_{exc} = Q + E^0_{kin}.$$

It should be noted that the height of the Coulomb barrier does not influence the excitation energy of the nucleus in any other way than that the projectile must have a kinetic energy greater than the E_{cb} before the reaction can occur.

The energy brought in by the projectile is transferred to the other nucleons through numerous collisions until a state of equilibrium is reached; this implies two important aspects:

- the compound nucleus represents a relatively long-lived reaction; in fact, we can say that the CN must live for at least several times the time it would take a nucleon to traverse the nucleus (i.e. $10^{-22}s$). Thus, the time scale of compound nuclear reactions is of the order of 10^{-18}–$10^{-16}s$.

- the particle energy is distributed evenly or almost evenly to all nucleons of the target so that, at this time, the original particle is undistinguishable from the other nucleons, and the CN has no "memory" of how it was formed. This phenomenon is called the *Bohr independence hypothesis* or the *amnesia assumption*.

Now, if sufficient energy is present, eventually a nucleon or a composite of nucleons will acquire enough energy to overcome nuclear binding forces and escape from the nucleus. This process is called *evaporation*. If residual energy remains

after one nucleon or composite unit has been evaporated, more may be emitted, until there is too little energy left to cause particle emission: the nucleus may then further de-excited via a gamma transition. Finally, the emission of neutrons from compound nuclei is preferred over emission of protons and reactions such as (p, n) and (α, n) are relatively probable if the energy of the incident particle is greater than $1\,MeV$.

1.2.2.2 Direct reactions

Direct reactions do not result in the assimilation of the projectile into the nucleus. Instead, the incoming particle interacts directly with the nucleons at the periphery of the nucleus in a very fast process ($\approx 10^{-22}s$) that involves the prompt emission of a nucleon. Thus, direct reactions happen in only one step, with no time for equilibration between the initial interaction and the resulting nuclear change. Therefore, the nucleus has a sort of "memory" of how it was formed, and the decay modes are related to the means by which the nucleus was originally excited [Ehmann and Vance, 1991].

Two types of direct interactions are distinguished: knock-on reactions and transfer reactions. Knock-on reactions may proceed in various ways: the incident particle may transfer a part of its energy to a nucleon and continue on its way (inelastic scattering). It may induce collective motion of the nucleus (vibration and rotation) or it may be captured by the nucleus and transfer its energy to one or several nucleons that leave the nucleus. The number of nucleon-nucleon collisions increases with the increasing energy of the incident particles. It is important to underline that this type of process is most commonly observed for projectiles with relatively high energy ($50\,MeV$ and above) [Lieser, 2001].

Transfer mechanism can be divided into *stripping* and *pick-up* reactions. In stripping, the target nucleus takes one of the nucleons away from the composite incident particle. In a pick-up reaction, the projectile takes a nucleon away from the target nucleus. In general, transfer reactions are most often observed for particles with energies less than $50\,MeV$.

Chapter 2

Fundamental physical, radiochemical and quantitative informations

In this chapter, the derived physical quantities that will be used in the future calculations are introduced. The quantities I am going to define, in order to fully describe the nuclear reactions I am interested in, are: the cross-section of nuclear reaction, the stopping power, the range, the thin target yield and the thick target yield.
Furthermore, the gamma spectrometry, the analytical technique at the basis of every results, will be shortly discussed.

2.1 Cross-section

In view of the great variety of possible projectiles and targets, a broad definition is desirable. Conventionally, a target has been hit if the interaction of the projectile with the target has had some specific measurable effect. This means that the probability of a given nuclear reaction not only depends on the target, the projectile, and their relative velocity, but also on the physical effect that I have decided to monitor. The probability of a nuclear reaction is usually expressed in terms of the cross-section reaction [Lilley, 2002]. Consequently, it is possible to talk about scattering cross-sections, absorption cross-sections, energy-loss cross-sections, ionization cross-sections, cross-sections for specific nuclear reactions and many others.

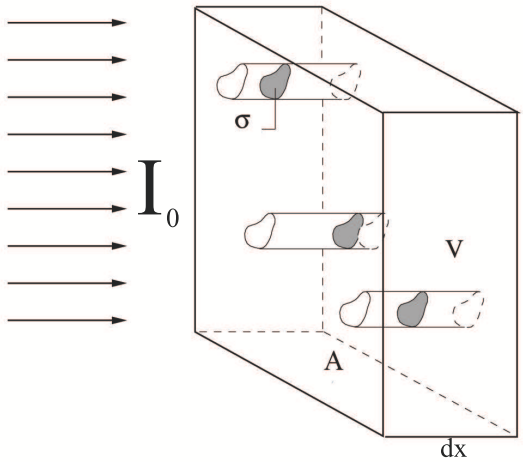

Figure 2.1: Macroscopic target consisting of randomly placed microscopic targets, bombarded by a particle current.

The one I am interested in is the cross-section for a specific nuclear reaction.

For fundamental and practical reasons there is no way of experimentally determining microscopic cross-sections by bombarding one atom with only one projectile. Instead, I utilize the statistical information extracted from a large number of bombardments.

Suppose a macroscopic target is bombarded by a beam of projectiles spread homogeneously over an area S_A (A in Fig. 2.1). If σ is the cross-section (area of one nucleus), then the total area of the nuclei in the target is:

$$S_{nuclei} = \frac{\sigma \cdot \rho \cdot S_A \cdot dx \cdot \mathbf{N}_A}{M} \qquad \left[cm^2\right] \tag{2.1}$$

where $\mathbf{N}_A = 6.0221415(10) \times 10^{23}\ mol^{-1}$ [Mohr et al., 2015] is the Avogadro's constant, ρ is the target density (g/cm^3), M is the atomic weight ($g \cdot mol^{-1}$) of the element and dx is the target thickness. The quantity $\rho \cdot dx$ is known as areal density or massic thickness. The origins of this concept lie in the difficulty in making an accurate estime of the real density ρ of the target. On the other hand, it is possible to determine the mass m of the foil rather easily and then calculate the areal density:

$$dx \cdot \rho = \frac{m}{S_A} \qquad \left[\frac{g}{cm^2}\right]. \tag{2.2}$$

Typical dimensions for material used in this work are of few mg/cm^2.

Furthermore, as just said above, the target area is:

$$S_{target} = S_A \qquad \left[cm^2\right]. \tag{2.3}$$

Thus, the probability P for one projectile to interact with a nucleus is:

$$P(1 \text{ projectile}) = \frac{S_{nuclei}}{S_{target}} = \frac{\sigma \cdot \rho \cdot dx \cdot \mathbf{N}_A}{M}. \tag{2.4}$$

For accelerators, the beam intensity (i.e. particle current = number of particle per unit time) I_0 is expressed by:

$$I_0 = \frac{i}{q} = \frac{i}{z\mathbf{e}} = \frac{Q}{t_{irr} z\mathbf{e}} \qquad \left[s^{-1}\right] \tag{2.5}$$

where i is the beam current (A), q is the projectile charge (C), $\mathbf{e}$ is the electron charge (C), z is the charge in electron units of the particle and Q is the total charge of the beam (C). It should be stressed that the change in current, $dI = I - I_0$, passing through a thin target layer of thickness dx, is infinitesimal (i.e. $I_0 \approx I$) [Ehmann and Vance, 1991].

Now, if N^* is the number of the nuclei which interact with the beam, the number of interactions per unit time is:

$$\frac{dN^*}{dt} = \frac{\sigma \cdot \rho \cdot dx \cdot \mathbf{N}_A}{M} I \equiv k \qquad \left[s^{-1}\right]. \tag{2.6}$$

Equation (2.6) is valid if the following conditions occur:

- the number of nuclear reactions must remain small compared to the total number of target atoms;
- the projectile energy must remain constant so that the cross-section reaction also remains constant;
- the particle current does not decrease in passing through the target.

Frequently, the irradiated target consists of more than one nuclide which can capture bombarding particles to undergo reaction. So, the macroscopic cross-section, which refers to the total decrease in the bombarding particle current, reflects the absorption of particles by the different nuclides, in proportion to their abundance in the target, as well as to their individual cross-section reaction. Assuming that the target as a whole contains N_V atoms m^{-3} with individual abundances w_1, w_2, etc., for nuclides 1, 2, etc., the individual cross sections are σ_1, σ_2, etc. Thus, the macroscopic cross-section Σ is:

$$\Sigma = N_V \sigma^* \equiv N_V \sum_1^n w_j \sigma_j \qquad \left[cm^{-1}\right]. \tag{2.7}$$

where σ^* is called the effective cross-section. For a target that has a geometrical thickness x (m) we obtain:

$$I = I_0 e^{-\Sigma x} \qquad \left[s^{-1}\right]. \tag{2.8}$$

The value Σ^{-1} is the average distance a projectile travels between successive collisions with the target atoms (the mean free path).

2.1.1 Nuclear cross-section and irradiation yield

The production of a radioactive nuclide by irradiation in accelerator can be written as:

$$T + P \overset{k}{\rightarrow} R_1 \overset{\lambda_1}{\rightarrow} R_2. \tag{2.9}$$

I am mainly concerned with the product R_1 (produced at rate k), which is assumed to be radioactive, decaying in a single step or via a chain of decays resulting in a final stable nuclide.

The rate of the net production of the N_1 atoms of the product R_1 is the rate of its production minus the rate of its decay:

$$\frac{dN_1}{dt} = k - \lambda_1 N_1. \tag{2.10}$$

The rate of decay of radioactive nuclides is always proportional to the number of the radionuclides. The proportionality constant is assigned usually by λ and it is called the decay constant. In almost all data tables λ is not given, but rather the half-life $t_{1/2}$ of the radionuclide. The relationship between λ and $t_{1/2}$ is $\lambda \cdot t_{1/2} = \ln 2$.

Integrating equation (2.10) between the limits of $N_1 = 0$ (no radioactive nuclide R_1 exists at the beginning of the irradiation) and N_1 for an irradiation time t_{irr}, we obtain:

$$N_1 = \frac{k}{\lambda_1}\left(1 - e^{-\lambda_1 t_{irr}}\right). \tag{2.11}$$

N_1 increases exponentially with time towards a maximum value (saturation limit), which is reached when $\lambda_1 t_{irr} \gg 1$ (i.e. $t_{irr} \gg t_{1/2}/\ln 2$). In this case it is possible to write:

$$N_{1,max} = \frac{k}{\lambda_1} \tag{2.12}$$

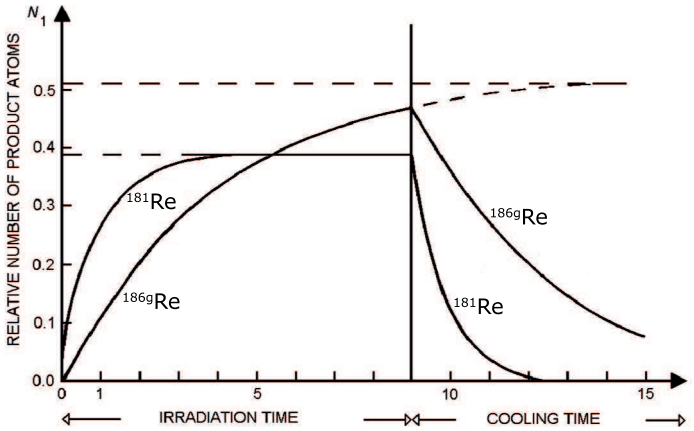

Figure 2.2: Examples of the change in number of ^{181}Re ($t_{1/2}$ = 19.9 h) and ^{186g}Re ($t_{1/2}$ = 90.64 h) atoms during and after irradiation.

However, if $t_{irr} \ll t_{1/2}/\ln 2$ it is possible to ignore the decay of the radionuclide since the rate of its formation is much greater than its decay rate. So, by expanding the exponential into a Maclaurin series, $\exp^{-\lambda_1 t_{irr}} \simeq 1 - \lambda_1 t_{irr}$, the equation (2.11) becomes:

$$N_1 = k t_{irr} \qquad (\text{for } t_{irr} \ll t_{1/2}/\ln 2). \tag{2.13}$$

Furthermore, if we measure the irradiation time in number of half-lifes, $a = t_{irr}/t_{1/2}$, we obtain:

$$N_1 = N_{1,max}\left(1 - 2^{-a}\right), \tag{2.14}$$

that shows that irradiation for one half-life ($a = 1$) produces 50 % of the maximum amount, two half-lives gives 75 % and so on.

After the end of the irradiation time, the radioactive product nuclides continue to decay according to their half-lives. I indicate this decay time after the end of irradiation (termed the cooling time) as t_{cool} . The number of nuclides, which is a function of the irradiation time t_{irr} and cooling time t_{cool}, is now expressed by:

$$N_1 = \frac{k}{\lambda_1}\left(1 - e^{-\lambda_1 \cdot t_{irr}}\right) e^{-\lambda_1 \cdot t_{cool}}. \tag{2.15}$$

The effect of the cooling time is shown in Figure 2.2 for two sample radionuclides.

Furthermore, we have to take into account the decay during the measurement. If at the beginning of the measurement the radioactive nuclides are N_1 (eq. (2.15)), after a counting time t_{count} they are:

$$N_2 = N_1 e^{-\lambda_1 \cdot t_{count}} = \frac{k}{\lambda_1}\left(1 - e^{-\lambda_1 \cdot t_{irr}}\right) e^{-\lambda_1 \cdot t_{cool}} e^{-\lambda_1 \cdot t_{count}}. \qquad (2.16)$$

So, in the elapsed time t_{count}, the number of the decayed radioactive nuclides is:

$$\Delta N = N_1 - N_2 = \frac{k}{\lambda_1}\left(1 - e^{-\lambda_1 \cdot t_{irr}}\right)\left(1 - e^{-\lambda_1 \cdot t_{count}}\right) e^{-\lambda_1 \cdot t_{cool}}. \qquad (2.17)$$

But, usually, the radioactive decay rate A_1, rather than the number of atoms N_1, is measured. Recalling $A \equiv \lambda N = -\Delta N/\Delta t$ (with $\Delta t = t_{count}$), equation (2.17) yields the averaged activity during the measurement (counting):

$$A_1 = \frac{k}{\lambda_1 \cdot t_{count}}\left(1 - e^{-\lambda_1 \cdot t_{irr}}\right)\left(1 - e^{-\lambda_1 \cdot t_{count}}\right) e^{-\lambda_1 \cdot t_{cool}} \qquad [Bq]. \qquad (2.18)$$

This general equation represents the basic relationship for the production of radionuclides and for equations (2.5), (2.6) and (2.18):

$$A = \frac{\sigma \cdot \rho \cdot dx \cdot \mathbf{N}_A \cdot Q \cdot \lambda}{M \cdot z\mathbf{e}}\left(\frac{1 - e^{-\lambda \cdot t_{irr}}}{\lambda \cdot t_{irr}}\right)\left(\frac{1 - e^{-\lambda \cdot t_{count}}}{\lambda \cdot t_{count}}\right) e^{-\lambda \cdot t_{cool}} \qquad [Bq]. \qquad (2.19)$$

In my experimental procedure, however, I am interested in evaluating the cross-section σ. Thus, from equations (2.19) we have:

$$\sigma = \frac{A \cdot M \cdot z\mathbf{e}}{\rho \cdot dx \cdot \mathbf{N}_A \cdot Q \cdot \lambda} \cdot G\left(t_{irr}\right) \cdot D(t_{count}) \cdot e^{+\lambda \cdot t_{cool}} \qquad \left[cm^2\right], \qquad (2.20)$$

with the correction growing factor:

$$G(t_{irr}) \equiv \frac{\lambda \cdot t_{irr}}{1 - e^{-\lambda \cdot t_{irr}}}, \qquad (2.21)$$

and the correction decay factor:

$$D(t_{count}) \equiv \frac{\lambda \cdot t_{count}}{1 - e^{-\lambda \cdot t_{count}}}. \qquad (2.22)$$

The evaluation of the activity A is presented in §§ 2.5 and 2.6.

2.2 Stopping power and range

All of the charged ions that I will consider have positive charges. Energetic charged ions move through material on essentially straight trajectories, giving up or losing

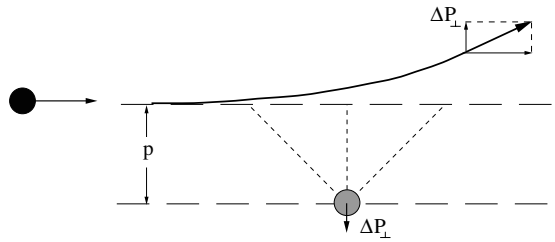

Figure 2.3: A scattering event with momentum transfer $P_\perp$ perpendicular to the beam direction.

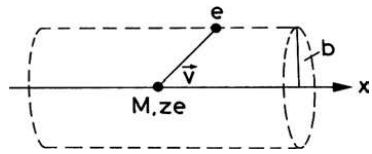

Figure 2.4: Trajectory of a moving ion past an electron.

kinetic energy through collisions with the atomic electrons of the material. In comparison, an ion is rarely scattered by the Coulomb potential of a nucleus, and even more rarely does a nuclear reaction take place. Nuclear reactions are excluded when the initial kinetic energy of the heavily charged particle is lower than the Coulomb barrier and the threshold energy (as summarized in § 1.1.3).

Thus, the ions interact with an extremely large number of electrons and the average behavior of the ions as they pass through matter can be examined. The rate at which charged particles lose energy as they travel through a given material is called the stopping power of that material. The *stopping power* is made up of two parts: the electronic stopping power, due to the interaction with the atomic electrons of the material, and the nuclear stopping power . This equation is expressed by:

$$-\frac{dE}{dx} = S_{electronic} + S_{nuclear} \approx S_{electronic} \qquad \left[\frac{MeV}{cm}\right], \tag{2.23}$$

where the electronic stopping power is always much larger than the nuclear stopping power [Krane, 1988]. The minus sign of the rate indicates that the ions are losing kinetic energy. The nuclear stopping power is not zero, of course, because we know that nuclear reactions take place, even if they are rare. The stopping powers are functions of the mass, the charge, the ion velocity and the atomic number of the target together with its density.

Niels Bohr suggested that the energy loss rate could be simply described as the series of impulses delivered to individual electrons by the ion [Bohr, 1913].

Imagine an ion moving on a straight-line trajectory past an electron (Fig. 2.3): a net impulse to the electron will occur perpendicular to the trajectory of the ion because any impulse, caused by the approaching ion, will be cancelled by that of the receding ion. It can be shown [Loveland et al., 2006] that the energy gained by a single electron (lost by the ion) in one encounter depends on the impact parameter b (Fig. 2.4) as:

$$\Delta E(b) = \frac{2z^2\mathbf{e}^4}{m_e v^2 b^2}, \tag{2.24}$$

where v is the velocity of the ion, and m_e is the mass of the electron. The number of electrons in a cylindrical ring with a radius between b and $b + db$ and thickness dx is $2\pi N_e b db dx$, where N_e is the electron number density. Consequently,

$$-dE(b) = \Delta E(b) N_e 2\pi db dx. \tag{2.25}$$

This expression should not be integrated from $b = 0$ to $b = \infty$ but only from the range b_{min} to b_{max} [Loveland et al., 2006] that corresponds to the initial assumptions regarding the ion and the electron, so that:

$$-\frac{dE}{dx} = \frac{4\pi z^2\mathbf{e}^4}{m_e v^2} N_e \ln\frac{b_{max}}{b_{min}}. \tag{2.26}$$

The minimum impact parameter will correspond to those collisions in which the maximum amount of kinetic energy is transferred to the electron. Due to the conservation of momentum, the maximum energy transferred to an electron is $T_{max} = \frac{1}{2} m_e (2\gamma v)^2$ [Amaldi, 1971] where we have included the relativistic factor γ (i.e. $\gamma = (1 - \beta^2)^{-1/2}$ where $\beta = v/c$) due to the low mass of the electron. Thus, substituting the energy loss at a given impact parameter into the equation (2.24):

$$T_{max} = \Delta E(b_{min}) = \frac{2z^2\mathbf{e}^4}{m_e v^2 b_{min}^2} = 2\gamma^2 m_e v^2 \tag{2.27}$$

we find that:

$$b_{min} = \frac{z\mathbf{e}^2}{\gamma m_e v^2}. \tag{2.28}$$

The maximum impact parameter has to be estimated from different considerations. The basis of this process is that the ion rapidly moves past the electron and delivers a sharp impulse to the electron. The electrons are bound in atoms and, thus, are orbiting with their own characteristic frequencies or time scales. Thus, the time for the ion to cross the atom should be less than the average time for an electron orbit; otherwise, the collision will not be adiabatic or "rapid". The time for

the ion to move past can be estimated as the ratio of the impact parameter to the ion's velocity and the average orbital time for an electron will clearly depend on the chemical element, as there will be an average radius and velocity. These considerations induced Bohr to evaluate the stopping power with a classical formula. Bohr's formula has been superseded by the expression derived by Bethe and Bloch [Bethe, 1932] based on momentum transfer in a quantum mechanically correct formalism. Their expression with the expanded form of the electron number density is:

$$\left(-\frac{dE}{dx}\right)_{\text{Bethe-Bloch}} = 4\pi \mathbf{N}_A r_e^2 m_e c^2 \rho \frac{Z z^2}{\mathbf{A}\beta^2}\left[\ln\left(\frac{T_{max}}{I}\right) - \beta^2\right], \tag{2.29}$$

where $r_e \equiv \mathbf{e}^2/m_e c^2 = 2.8179402894(58) \times 10^{-15} m$ [Mohr et al., 2015] is the classical radius of the electron, ρ is the density of the stopping medium with atomic number, Z, mass number, $\mathbf{A}$, and ionization potential, I. Finally, T_{max} is the maximum energy transfer, encountered above. Various formulas are available to give the average variation of the ionization potential for the chemical elements. For example, in the Thomas-Fermi model, the expression is given by [Amaldi, 1971]:

$$I \cong 10 \cdot Z \qquad [eV]. \tag{2.30}$$

The modern form of the stopping power includes two corrections [Loveland et al., 2006]. The first one is applied at high energies at which the polarization of electrons by the electric field of the moving ion tends to shield distant electrons. This correction depends on the electron density. Furthermore it is a subtractive term and given the symbol δ. The second correction is applied at low energies when the collisions are no longer adiabatic, similar to the limit introduced by Bohr. This correction is termed the shell correction as it depends on the orbital velocities of the electrons. It is also a subtractive term and given the symbol C. If we include all the constants, the modern form becomes:

$$\left(-\frac{dE}{dx}\right)_{\text{Bethe-Bloch}} = 0.3071 \frac{MeV \cdot cm^2}{g} \rho \frac{Z z^2}{\mathbf{A}\beta^2}\left[\ln\left(\frac{T_{max}}{I}\right) - \beta^2 - \frac{\delta}{2} - \frac{C}{Z}\right] \tag{2.31}$$

which has the dimensions of MeV/cm when the usual form of the density in g/cm^3 is used. The actual evaluation of this function is complicated due to the detailed variation of the ionization potential and the two correction terms. In practice, several computer codes and detailed tables of the stopping powers are available.

Sometimes, for example, when combining materials, it is more useful to use the stopping power divided by the density, ρ, and report the mass stopping power as:

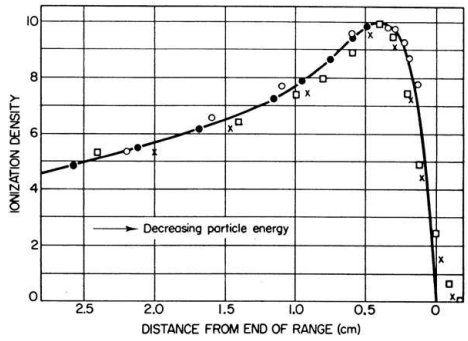

Figure 2.5: Density of ionization along the path of a particle stopping in air. The Bragg peak in the ionization density is evident. [Holloway and Livingston, 1938]

$$-\frac{1}{\rho}\frac{dE}{dx} \qquad \left[\frac{MeV \cdot cm^2}{g}\right]. \tag{2.32}$$

Looking at the these equations for the stopping power, it can be seen that they all have a part that depends on the moving ion and another part that depends on the stopping medium. Concentrating on the part that depends on the ion, it can be written:

$$-\frac{dE}{dx} \propto \frac{z^2}{v^2}\ln(\gamma^2 v^2)g(Z), \tag{2.33}$$

in which we can convert the factors of v^2 into kinetic energy, E, by suitably applying factors of $\frac{1}{2}m_{ion}$. The function $g(Z)$ collects all the variations of the absorbing medium. The revised expression shows that the energy loss rate will be proportional to the mass of the ion:

$$-\frac{dE}{dx} \propto \frac{\mathbf{A}z^2}{2E}\ln\left(\frac{\gamma^2 2E}{\mathbf{A}}\right)g(Z). \tag{2.34}$$

At low ion velocities ($E/\mathbf{A} < 10 \quad MeV/\mathbf{A}$), the $\ln(\gamma^2 2E/\mathbf{A})$ term is approximately constant and then the stopping power is inversely proportional to the kinetic energy:

$$-\frac{dE}{dx} \propto \frac{\mathbf{A}z^2}{E} \tag{2.35}$$

Thus, a more energetic ion will tend to lose energy at a lower rate than a less energetic ion. Note that the relativistic terms, $\gamma^2 = 1/\left(1-\beta^2\right)$ and $\beta^2 = \frac{v^2}{c^2}$, in the parentheses, were ignored. These terms produce a minimum in the complete function near $\beta \sim 0.96$ and a small rise at higher velocities. (Particles with $\beta \sim 0.96$ are called minimum ionizing particles.)

The energy loss rate begins to increase dramatically as $\beta \to 0$, but, more important, the charge state of the ion starts to decrease as the ion captures orbital electrons causing the rate to drop. The ion rapidly loses energy at the end of its range and stops rather suddenly. The energy loss for a particle near the end of its range is shown in Figure 2.5. The resulting peak in the energy loss function, just before the end of the charged particle's range, is called the *Bragg peak*. The fact that charged particles deliver a significant fraction of their kinetic energy at the end of their range makes charged particles useful for radiation therapy. All of these conditions for the stopping power only apply to pure chemical elements. The stopping power of a compound or any complicated mixture will depend on the overall density and the relative numbers of electrons from each chemical element. Recognizing that the ionizing radiation will usually move through macroscopic distances, we can use an averaging procedure called Bragg's rule (eq. (2.36)) [Amaldi, 1971]. The average mass stopping power is:

$$\left(\frac{1}{\rho}\frac{dE}{dX}\right)_{\text{total}} = \sum_j \frac{w_j}{\rho_j}\left(\frac{dE}{dX}\right)_j \tag{2.36}$$

where w_j, ρ_j, and so forth, refer to the fraction by mass of element j-th in the entire mixture and its elemental density. The summation is done for all the elements in the mixture. Thus, if the mixture were a pure compound, then we would combine the numbers of each element in the molecular formula. If the mixture had several components, then we would combine the masses of each element from all the components, and so on, to get an overall mass stopping power.

The range or distance that a heavily charged particle will travel through a material can be obtained by integrating the energy loss rate along the path of the ion. In the approximation that the ion follows a straight-line trajectory, then the range for a given kinetic energy, $R(T)$, would be given by the integral [Sigmund, 2006]:

$$R(T) = \int_0^T -\left(\frac{dE}{dx}\right)^{-1} dE \tag{2.37}$$

where the function dE/dx is the appropriate function for the ion in the material. There are two difficulties in applying this simple integral formula: the ions will suffer a different number of collisions with atomic electrons, and, more importantly, the ions will undergo some scattering from the Coulomb fields of the atomic nuclei. The multiple Coulomb scattering leads to an effect that the ion's trajectory is not straight, but rather, is made up of a series of straight line segments. Thus, the apparent range or the projection of the range onto the initial velocity vector of the ion will not be a single value, but rather, will consist of a statistical distribution of

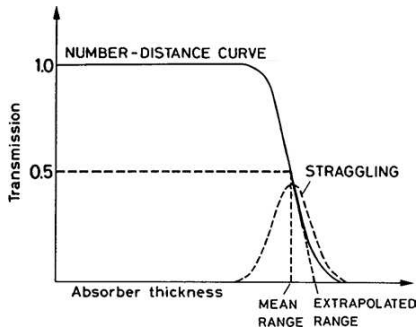

Figure 2.6: Intensity distribution or attenuation curve is shown as a function of absorber thickness for a typical energetic heavy ion penetrating into a metal. The effect of range straggling is indicated by the Gaussian distribution of ranges.

values. Thus, the distribution of ranges is due to range straggling. It is important to note that the size of range straggling will grow as an ion penetrates into the material because it will literally add up. The range of an ion and its fluctuations are integral quantities, whereas the energy loss rate and its fluctuations are differential quantities. It is still true that Coulomb and nuclear scattering are relatively rare, so that the range straggling for typical ion energies in metals is only a small percent of the range. The qualitative features of the range distribution and the attenuation curve for a typical heavily charged particle are shown in Figure 2.6. Heavily charged particles penetrate uniformly into matter with essentially no attenuation in intensity until they are nearly at rest; at this point, the intensity of moving ions rapidly drops to zero.

It can be seen from the integral form of the range as a function of initial kinetic energy, given above, that $R \propto aE^b$ (Fig. 2.7). The exponent should be of order 2 at low energies where the energy loss rate is dominated by the $1/\beta^2$ or $1/E$ term. The range–energy relationships are very useful in determining the kinetic energies of particles by measuring the attenuation curves.

As a final point (more practical) is related to the use of the stopping power and ranges of charged particles, as the best method to calculate the amount of energy deposited in a thin foil. Clearly, the ion will slow down as it passes through the material so that the energy loss rate will change as the particle passes through the foil. Thus, the average energy loss rate should be used. However, since the function is not linear, a technique to determine the average is required. The main interest is for thin foils in which the initial, average, and final energy loss rates are nearly the same. In this case of a thin foil [Loveland et al., 2006], the following expression can be used:

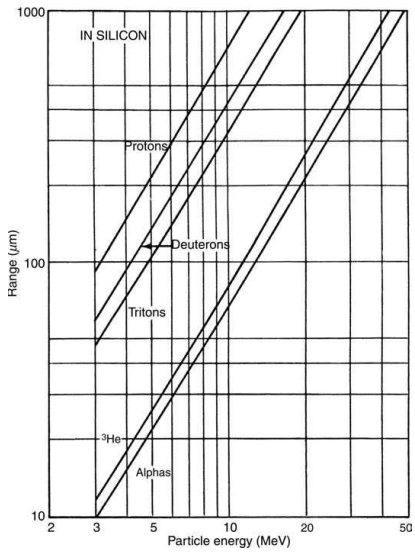

Figure 2.7: Range-energy curves for some charged particles in silicon. Note the data has the form $R \propto aE^b$ with a similar exponent for all ions. [Skyrme, 1967]

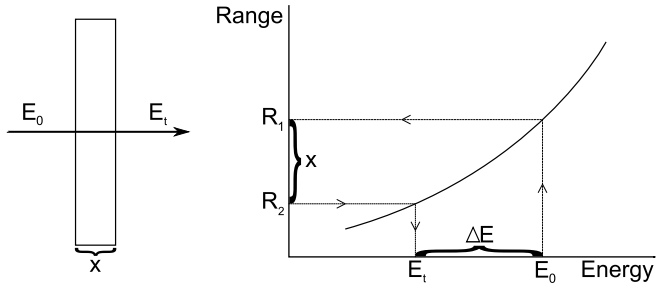

Figure 2.8: Graphical representation of the range-energy evaluation.

$$\Delta E(\Delta x) = \left(\frac{dE}{dx}\right) \Delta x. \tag{2.38}$$

It should be verified that the final rate is approximately equal to the initial rate:

$$\left(\frac{dE}{dx}\right)_{\text{initial}} = \left(\frac{dE}{dx}\right)_{\text{final}}. \tag{2.39}$$

If the energy loss rates are not substantially different, then the average rate can be obtained from the initial rate by the following approximation procedure. The technique relies on determining the ranges of ions in graphs or tables of ranges as follows (Fig. 2.8): imagine that an incident particle with an energy E_0 passes through some material with thickness x. These are the "known quantities". The

particle will emerge from the foil with an energy E_t, which should be determined. The total range, R_1, of the ion in the material can be found from tables. The particles that emerge from the foil will have a residual range equal to $R_1 - x$. The range table or graph can be used to determine E_t that corresponds to the range $R_2 = R_1 - x$. The slowing down and averaging of the energy loss rate will be contained in the range function and do not have to be explicitly evaluated.

For practical purpose, range-energy tables or relationships are among the most commonly used tools. The largest collection of data on stopping powers and ranges of ions in matter is that of Ziegler and Biersack contained in the computer SRIM/TRIM programs [Ziegler et al., 2010].

2.3 Thin target yield

Thin target yield (tty) $y(E)$ is a function of projectile energy. It is defined as the slope at the origin of the growing curve of the activity per current unit (A/i) of a radionuclide versus the irradiation time (t_{irr}) for a target in which the energy loss is insignificant compared to the projectile energy [Bonardi, 1987]. In practice, the tty is defined as the second derivate of A/i respect to the particle energy and the irradiation time, which is calculated when the irradiation t_{irr} tends toward zero (i.e. End Of Instantaneous Bombardment, EOIB):

$$y(E) = y(E)_{EOIB} = y(E,0) = \left[\frac{\partial^2(A/i)}{\partial E \partial t_{irr}}\right]_{t_{irr}\to 0} \qquad \left[\frac{Bq}{C \cdot MeV}\right]. \tag{2.40}$$

Considering equations (2.18) and (2.6) and applying the (2.40) leads to:

$$y(E) = \frac{\sigma^*(E)\mathbf{N}_A\lambda}{Mz\frac{1}{\rho}\frac{dE}{dx}(E)} \tag{2.41}$$

where $E = \langle E \rangle$ is the "average" projectile beam energy (MeV) in the thin target. In such situation, the equation (2.38) is a good approximation. In addition, $\rho dx = \rho\Delta x$ can be measured by using equation (2.2) and ΔE can be easily calculated by the difference of ranges of incoming and outgoing particles in the target using the technique previously shown in Figure 2.8.

2.4 Thick Target Yield

The Thick-Target Yield (TTY) $Y(E, \Delta E)$ is defined as a two parameter function of incident particle energy $E\,(MeV)$ on the target and the energy loss in the target

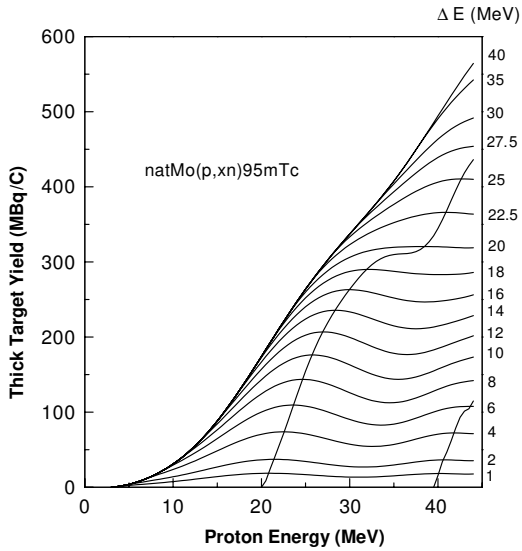

Figure 2.9: Example of calculated thick-target yield as a function of target thickness (in MeV) for ^{95m}Tc production [Bonardi et al., 2002].

itself ΔE (MeV) [Bonardi, 1987], according to the equation (2.42), that holds in the approximation of a monochromatic beam of energy E not affected by either intrinsic energy spread or straggling:

$$Y(E, \Delta E) = \int_{E-\Delta E}^{E} y(x)dx \qquad \left[\frac{Bq}{C}\right]. \tag{2.42}$$

Note that the integrand $y(x)$ represents the tty of equation (2.41). In case of total particle energy absorption in the target (i.e. energy loss $\Delta E = E$), the function $Y(E, \Delta E)$ reaches a value $Y(E, E - E_{th})$, for $\Delta E = E - E_{th}$, that mathematically represents the envelope of the $Y(E, \Delta E)$ family of curves. This envelope is a monotonically increasing curve, never reaching neither a maximum nor a saturation value, even if its slope becomes insignificant for high particle energies and energy losses. Equation (2.42) states, obviously, that the production yield of a thick-target does not increase further if the residual energy in the target is lower than the nuclear reaction energy threshold, E_{th}.

The expressions of thin-target yields $y(E)$ are analytically or numerically integrated at given intervals obtaining the groups of curves reported in Figure 2.9. In the same picture, the first and second calculated loci of the maxima of Thick-Target Yields are represented (the second maximum is present only in some cases). These maxima correspond to couples of optimized values $(E, \Delta E)$, having different values for each different radionuclide.

2.5 γ-spectrometry with HPGe detectors

The evaluation of the samples activity, and of all physical quantities linked to it (cross-sections and target yields), was done by using gamma spectrometry[1]. Thus, it is necessary to describe some important aspects dealt with this technique and, especially, with the detector calibration.

A modern gamma-ray spectrum is, in essence, a list of numbers of pulses measured within small consecutive pulse height ranges. Detector calibration allows the γ-ray spectrum to be interpreted in terms of energy and amount of activity. This is possible thanks to two main tasks: the energy calibration (i.e. the relationship between channels and energy) and the efficiency calibration (i.e. the relationship between number of counts and disintegration rate).

In order to calibrate the detector, in gamma spectrometry, it is extremely important to consider the quality of the nuclear data[2] used in the calibration process. This means that it is necessary to choose a Nuclear Database and then use it for all measurements: both for the detector calibration and for the spectra analysis.

2.5.1 Efficiency calibration

The term "efficiency" is used in many contexts and has many different meanings. In experimental physics, it is generally defined as the ratio between the response of the instrument and the value of the physical quantity that is measured. In gamma spectrometry the intention is to relate the peak area in the spectrum to the amount of radioactivity it represents. For this reason, we need the *absolute full-energy peak efficiency* ε: this relates the peak area to the number of gamma-rays emitted by the source.

The absolute efficiency is generally defined as the ratio of the number of counts detected in a peak to the number emitted by the source:

$$\varepsilon = \frac{\text{events registered}}{\text{events emitted by source}}.$$

This function depends upon the geometrical arrangement of the system source-detector and upon the probability of an interaction in the detector itself. So, the absolute efficiency can be factored into two parts: the intrinsic efficiency ε_{int} and the geometrical efficiency or acceptance ε_{geom}. Thus ε is, then, given by the

[1] For a complete treatment of the topic see Debertin and Helmer 1988, Gilmore 2008, ICRU 1994, Knoll 2000.

[2] The interesting nuclear data useful to the detector calibration are γ-ray energies, their probability of emission and the half-life of the nuclide.

product:

$$\varepsilon = \varepsilon_{int} \cdot \varepsilon_{geom}.$$

The intrinsic efficiency relates the counts in the spectrum to the number of γ-ray incidents on the detector:

$$\varepsilon_{int} = \frac{\text{events registered}}{\text{events hitting the detector}};$$

this probability depends on the cross-section interaction of the incident radiation on the detector medium. The intrinsic efficiency is, thus, a function of the type of radiation, its energy and the detector material.

The geometrical efficiency, instead, is that fraction of the source radiation which is geometricaly intercepted by the detector. This depends entirely on the geometrical configuration of the detector-source system.

Since it is quite impossible to separate the two elements of the absolute efficiency, I have decided to fix the geometry and, thus, evaluate ε.

2.5.1.1 Absolute full-energy peak efficiency

The absolute full-energy peak efficiency is the parameter with the most significance in practical gamma spectrometry. The calculation of ε is straightforward. It is the ratio of the number of counts detected in a peak to the number emitted by the source:

$$\varepsilon = \frac{cps}{A \cdot I_\gamma},$$

where *cps* are the counts per second (i.e. the full-energy peak count rate), A is the source activity (Bq) and I_γ is the probability of emission of the particular gamma-ray being measured (i.e. gamma-ray abundance).

Thus, in order to obtain the efficiency calibration curve, I have used two certified calibration sources: ^{152}Eu and ^{133}Ba.

Each radionuclide's spectrum, collected considering the same geometry and same duration, was analysed. In particular, I computed the absolute efficiency for all the more important gamma emissions. In fact, it is conventional to construct an efficiency curve by measuring many γ-rays and plotting efficiency against energy (Fig. 2.10).

It is evident that the relationship is approximately linear in a bilog scale over much of the commonly used energy range, from 150 to 2000 keV. Below 150 keV, the efficiency falls due to absorption in the detector cap and dead layers. This is the critical part, specifically in corrispondence to the so-called "knee", where the

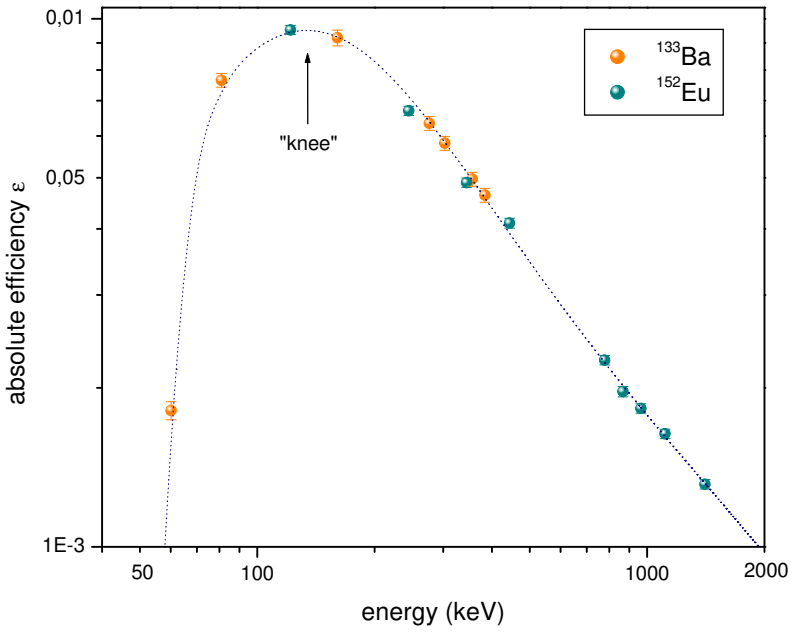

Figure 2.10: Efficiency curve obtained combining the values of two calibration sources such as ^{152}Eu and ^{133}Ba.

accuracy of the efficiency curve must be as high as possible. In fact, in this region, a tiny mistake, both in the choice of the peak area and of the fitting function, may imply significant differences in the final value of the efficiency itself. This means that the mathematical function I use to fit the experimental data also plays an important role in gamma spectrometry. Furthermore, it is important to recognize that none of the possible fitting equations has any theoretical basis. They are all simply empirical relationships which may fit the experimental data to a greater or lesser degree. A higher-order polynomial function will certainly be able to fit all the slight variations in the data better than a lower one and will give a better "goodness-of-fit" factor. This is the reason why I have chosen this type of function for $log(\varepsilon)$ against the peak energy E (in keV):

$$\varepsilon(E) = e^{\sum_{i=1}^{6} a_i E^{2-i}} = e^{a_1 E + a_2 + \frac{a_3}{E} + \frac{a_4}{E^2} + \frac{a_5}{E^3} + \frac{a_6}{E^4}}, \tag{2.43}$$

where a_i are the best fitting coefficients.

One of the advantages of this polynomial expression is that it is usually applied as a single equation covering the whole energy range of interest (i.e. typically up to 2000 keV).

2.6 Experimental activity, cross-section and yield evaluation

After the introduction of the main parameters relating to gamma spectrometry, I am able to evaluate unknown activities of given samples measured using the same geometry of the calibration sources. If C_γ are the counts per second registered by the detector:

$$C_\gamma = \frac{\text{events registered}}{LT} \qquad \left[s^{-1}\right], \tag{2.44}$$

where LT is the live time of the detector, i.e. the time period in which the detector really works ($LT < t_{count}$), defined $\varepsilon(E_\gamma)$ as the total efficiency at energy E_γ and I_γ as the abundance of the gamma-ray, the activity is given by:

$$A = \frac{C_\gamma}{\varepsilon(E_\gamma) \cdot I_\gamma} \qquad [Bq]. \tag{2.45}$$

Since I am interested in the evaluation of the cross-section σ, inserting equation (2.45) in (2.20), I obtain the experimental value:

$$\sigma = \frac{C_\gamma}{\varepsilon(E_\gamma) \cdot I_\gamma} \frac{M\mathbf{e}}{\lambda Q \mathbf{N}_A \rho x} \cdot D(RT) \cdot G(t_{irr}) \cdot e^{\lambda \cdot t_{cool}} \qquad \left[m^2\right]. \tag{2.46}$$

Now, combining this formula with equation (2.41), the experimental thin target yield becomes:

$$y(E) = \frac{C_\gamma}{\varepsilon(E_\gamma) \cdot I_\gamma} \frac{10^{-6}}{Q \Delta E} \cdot D(RT) \cdot G(t_{irr}) \cdot e^{\lambda \cdot t_{cool}} \qquad \left[\frac{Bq}{MeV \cdot C}\right], \tag{2.47}$$

and, for the Thick-Target Yield (eq. (2.42)), it can be concluded that:

$$Y(E) = \frac{C_\gamma}{\varepsilon(E_\gamma) \cdot I_\gamma} \frac{10^{-6}}{Q} \cdot D(RT) \cdot G(t_{irr}) \cdot e^{\lambda \cdot t_{cool}} \qquad \left[\frac{Bq}{C}\right]. \tag{2.48}$$

These formulas are the basis of my experimental evaluations and analysis that will be presented in the next chapters.

2.7 Main radiochemical parameters

In the radiochemical and radiopharmaceutical industry, the concepts, and subsequent specification used for determining the purity of the radiopharmaceutical product, are of concern to both the regulator and the producer.

In this section I present the fundamental quantities involved in the evaluation of pharmaceutical qualities.

2.7.1 A_S, C_A and IDF

In nuclear and radiochemistry the concepts of specific activity, radioactive concentration, isotopic and non-isotopic carrier, carrier-free and no-carrier-added are of paramount relevance. In fact, traces of carrier are easily introduced in the radioactive preparations: they may be present in the target material, in the equipment and chemicals used in target processing, and, finally, they may also be produced by side nuclear reactions induced in the target by nuclear activation, sometimes followed by a decay chain. Moreover radionuclides, particularly short-lived ones, may be present as ultra-traces, as is evident from the basic equation (2.49) relating activity to number of radionuclides. Thus, the radionuclide mass is given by:

$$\text{Amount } (mol) = \frac{\text{activity } (Bq) \cdot t_{1/2}\,(s)}{\ln 2 \cdot \mathbf{N}_A} \tag{2.49}$$

where $\mathbf{N}_A$ is the Avogadro's constant (mol^{-1}).

2.7.1.1 A_S specific activity

In many relevant applications of radionuclides a specific activity (A_S) as high as possible is envisaged [de Goeij and Bonardi, 2005b]. The use of radiotracers with high specific activity plays a fundamental role. In fact for biological studies, it is very important that there is no deviation from the normal physiological state: if, to produce the required tracer activity, the chemical level of the compound given to an organism greatly exceeds the normal physiological or chemical level, the therapeutical effects or diagnosis are open to question. So, the specific activity of the tracer compound must be sufficiently high for the total chemical level to be administered to be within the normal range.

In the last decades many efforts have been made to develop new nuclear production methods without intentional addition of isotopic carrier. The radionuclides obtained in this way are named no-carrier-added (NCA). The isotopic carrier is the total number of atoms (or mass) of the same element (same Z) present in a radioactive preparation. Unfortunately, NCA is a qualitative definition and in most prac-

tical cases the radionuclide concerned is diluted in a mixture of both radioactive and stable atoms of the same element.

We define quantitatively the specific activity of a radionuclide with a 100% radionuclidic purity (see § 2.7.2), under the assumption that a free isotopic exchange is provided in the radioactive preparation and that only stable isotopic carrier is present, as:

$$A_S(t) = \frac{N(t) \cdot \lambda}{m(t)} \qquad [Bq \cdot kg^{-1}] \tag{2.50}$$

where $N(t)$ is the number of atoms of the radionuclide concerned at time t (s), $m(t)$ is the total mass (kg) of all atoms (both stable and radioactive) of same Z present in radioactive preparation at time t and $\lambda \equiv \ln 2/t_{1/2}$ is the decay constant (s^{-1}) of radionuclide with half-life $t_{1/2}$ (s). In the case of accelerator-produced radionuclides, the order of magnitude of A_S (NCA) is very often in the $MBq \cdot \mu g^{-1}$ to $GBq \cdot \mu g^{-1}$ range.

In a few selected cases, a radionuclide can be considered absolutely free of isotopic carrier. In such cases the radionuclide of atomic mass M $(kg \cdot mol^{-1})$ is named carrier-free and its A_S is calculated as:

$$A_S(CF) = \frac{\mathbf{N}_A \cdot \lambda}{M} \qquad [Bq \cdot kg^{-1}]. \tag{2.51}$$

This parameter is a constant for each nuclide and, for example, for ^{103}Pd is $2.76\ GBq \cdot \mu g^{-1}$.

In order to complete the definitions related to $A_S(t)$, it should be realized that in many cases, a suitable amount of isotopic carrier is added intentionally during the radiochemical processing of a radionuclide. The main aim of this procedure is either to increase the radiochemical yield of the separation of a specific radionuclide from a mixture of both stable and radioactive elements or compounds, or the preparation of a labelled chemical species with a concentration representative of investigation carried out. A radionuclide obtained in this way is named carrier added (CA) and its specific activity is defined $A_S(CA)$; the numerical relation between the different types of specific activity is: $A_S(CA) \ll A_S(NCA) \leq A_S(CF)$.

2.7.1.2 C_A activity concentration

Activity concentration $C_A(t)$ of a radionuclide at time t is defined as the ratio between the activity A (Bq) of radionuclide and the mass (kg) or volume (m^3) of substrate or solvent in which the radionuclide is diluted [Bonardi et al., 2004]:

$$C_A(t) = \frac{\text{activity of radionuclide}}{\text{mass or volume of substrate}} \qquad [Bq \cdot kg^{-1}] \text{ or } [Bq \cdot m^{-3}]. \tag{2.52}$$

Sometimes the two quantities $A_S(t)$ and $C_A(t)$ are considered as synonyms and seem interchangeable, even though the definitions of these two quantities are completely different.

2.7.1.3 IDF: isotopic dilution factor

Further on, a relevant dimensionless quantity that can be introduced in order to express quantitatively the degree of isotopic dilution of a radionuclide is the isotopic dilution factor $IDF(t)$ [Bonardi and de Goeij, 2005]. This is the ratio at time t after end of radiochemical processing (EOP), including labelling, if applicable, of a radionuclide, between the number of all atoms (both stable and radioactive) isotopic with radionuclide of interest and the number of atoms of radionuclide itself. The $IDF(t)$ at the EOP is denoted by IDF. It is easy to show that, under the assumption that all isotopes are present in the same chemical form, the $IDF(t)$ is the ratio between $A_S(CF)$ and $A_S(t)$, or:

$$IDF(t) = \frac{\text{number of stable and radioactive nuclides of the same Z}}{\text{divided by the number of atoms of the radionuclide}} = \frac{A_S(CF)}{A_S(t)}.$$

Thus, the $IDF(t)$ is a dimensionless quantity presenting always values not lower than unity, while just in the case of a true CF radionuclide, the $IDF(CF)$ is equal to unity.

2.7.2 Radiopharmaceutical preparation

Production of radiopharmaceutical preparations has to respond to the characteristics presented in the Pharmacopoeia. A relevant parameter presented in the Phamacopoeia is the radionuclidic purity that is defined as the ratio, expressed as a percentage, of the radioactivity of the radionuclide concerned to the total radioactivity of the radiopharmaceutical preparation:

$$RNP_{\%}(t) = \frac{A^*(t)}{\sum_j A_j(t)} \cdot 100 \tag{2.53}$$

where $A^*(t)$ is the activity of the radionuclide of interest and $A_j(t)$ is the activity of the j-th nuclide at a stated time t.

Another important parameter stated in the Pharmacopoeia is the radiochemical purity, defined as the ratio, expressed always as a percentage, of the radioactivity of the radionuclide concerned which is present in the radiopharmaceutical preparation

in the stated chemical form, to the total radioactivity of that radionuclide present in the radiopharmaceutical preparation.

Chapter 3

Irradiation facilities

The irradiations for my work were carried out with the cyclotron (Scanditronix MC40, K = 38) of the JRC-Ispra (section 3.1) and with the cyclotron of the ARRONAX center, Saint-Herblain (FR) (IBA C70, section 3.2): after the closure of the cyclotron of the JRC-Ispra from January 2015, I decided to move to the cyclotron of the ARRONAX center because its beam is similar to the SPES one [Prete et al., 2014] that is being installed in the INFN national laboratory of Legnaro (LNL-INFN).

Even if there were a lot of differences in the irradiation conditions, I will show (Chapter 6) that there is a good overlap between the experimental data obtained from the Ispra and the ARRONAX irradiations.

3.1 Ispra cyclotron

The cyclotron of the Joint Research Centre (JRC) of the European Commission in Ispra (VA, Italy) (Fig. 3.1), created in 1982, is used for materials research and for the production of radionuclides for medical applications (diagnosis and therapy).

The accelerator, an AVF (isochronous) cyclotron, is a Scanditronix MC 40 model (K=38, beam current up to $60\,\mu A$), which is variable energy and accelerates positive ions (protons, deuterons, alphas and $^3He^{2+}$). The relevant characteristics of extracted beams are reported in Table 3.1.

3.1.1 Cyclotron Set-up

The irradiations, carried out with the cyclotron of JRC-Ispra, were at different energies with a typical current of $100\,nA$. This cyclotron (Fig. 3.2) has 7 beam

Figure 3.1: Ispra cyclotron building.

Table 3.1: Characteristics of the JRC Cyclotron extracted beam.

Particle	*Energy (MeV) (min.-max.)*	*Maximum extracted current μA*
p	8–40	60
d	4–20	30
alpha	8–53	30
$^{3}He^{2+}$	4–20	60

lines designed for different purposes. In my experiment, I used the beam line # 1 to study the excitation functions (Fig. 3.3). The beam line leaves the cyclotron and is driven till the irradiation chamber.

The beam passes through a *first collimator* (Fig 3.4 point a, diameter 6 *mm*) which stops the major part of the beam, especially the tails. In fact the beam profile is not a trivial topic (see §3.3) in order to obtain a beam profile in its central part as homogeneous as possible in order to irradiate the target surface with the same intensity. So, this first collimator cuts off the lateral parts of the beam and, thus, reduces its diameter. Since it blocks almost the entire beam, it heats up during the irradiation process. It can be cooled down with water and in this case must be used line # 2 that is suitable constructed. In my case the beam current is low enough to use line # 1 without using of the cooling system. Usually, only one collimator is

(a) Control room. (b) Cyclotron.

Figure 3.2: Ispra (Va) cyclotron.

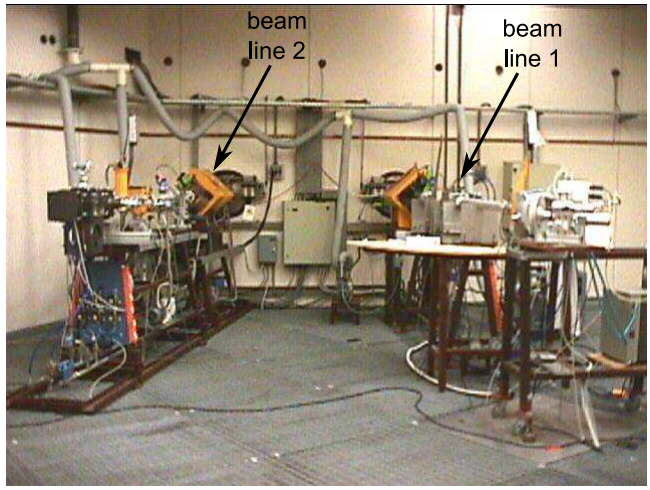

Figure 3.3: Beam lines # 1 e # 2 of the Ispra cyclotron.

not enough to properly modify the beam profile. This is the reason why there is a *second collimator* (Fig. 3.4 point b), with a diameter of 5 mm, with the function to further reduce the beam dimension and definitely cut off any residual tail.

Then, the beam enters in the *Faraday Cup* which collects the whole charge produced inside in order to determine the integrated charge (Fig. 3.4 point c and Fig. 3.5). In these irradiations the Faraday cup consists of a *magnet collimator*, the peculiarity of which is based in the insertion of two little magnets which goal is the deflection of the secondary electrons produced during the collision so that only the whole primary charge can be collected inside the Faraday Cup (Fig. 3.5 point

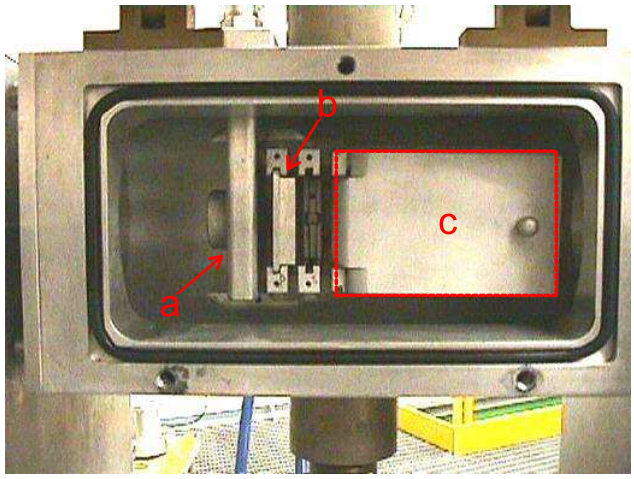

Figure 3.4: Irradiation chamber.

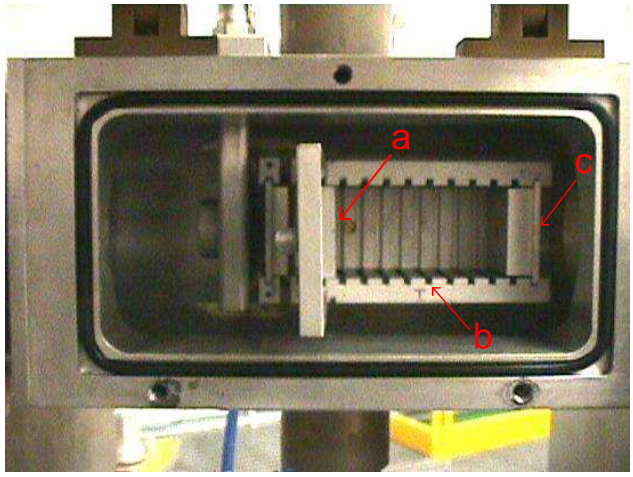

Figure 3.5: Faraday cup.

a). In the middle of the cup, there is enough space where it is possible to introduce various numbers of targets in agreement with the geometrical dimensions of the targets themselves (Fig. 3.5 point b). Finally, if the energy of the beam is so high that the material foil is not able to completely stop the beam, a *beam stopper* is able to stop and collect all the residual charges (Fig. 3.5 point c).

3.2 ARRONAX cyclotron

ARRONAX, an acronym for "Accelerator for Research in Radiochemistry and Oncology at Nantes Atlantique", is a high energy (70 MeV for protons) and high intensity ($2 \times 375\,\mu$A for protons) multi-particle accelerator located in Saint-Herblain (France). It began its hands-on phase in December 2010.

ARRONAX, an AVF cyclotron with 4 high hill sectors, is an IBA model Cyclone 70XP, which is variable energy and accelerates positive ions (protons, deuterons, alphas and H_2^+). The relevant characteristics of extracted beams are reported in Table 3.2.

Table 3.2: Characteristics of the ARRONAX Cyclotron extracted beam.

Particle	*Energy (MeV) (min.-max.)*	*Maximum extracted current μA*
p	35–70	375×2
d	15–35	50
alpha	70	70
H_2^+	35	50

3.2.1 Cyclotron Set-up

The irradiations, carried out with the cyclotron of ARRONAX-Nantes (Fig. 3.6), were at different energies with a typical current of $\sim 150\,nA$. This cyclotron has 8 beam lines designed for different purposes: five vaults, dedicated to average and high current, each house a single end-station and one vault, dedicated to low or very low current, has three (Fig. 3.7).

The beam line is closed using a 75 μm thick kapton foil which makes a barrier between the air in the vault and the vacuum in the line. The stacks were located about 6–8 cm downstream in air (Fig. 3.8). A beam dump was placed after the stack to control the intensity during the irradiation.

3.3 Beam profile

The beam profile is not a trivial issue. Ideally the beam profile must be flat. In my experiments and spatially distributed in a homogenic way in order to activate in an

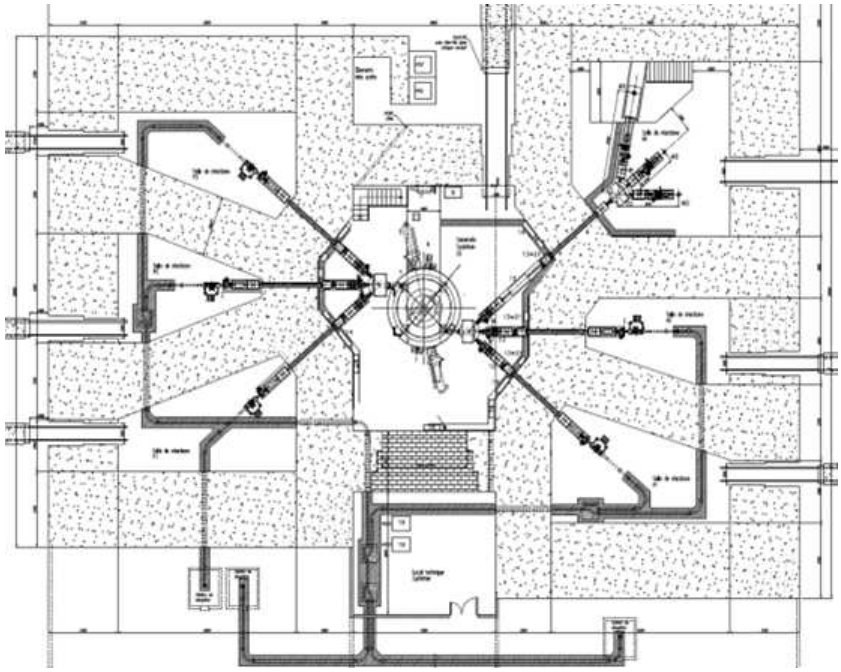

Figure 3.6: ARRONAX cyclotron building.

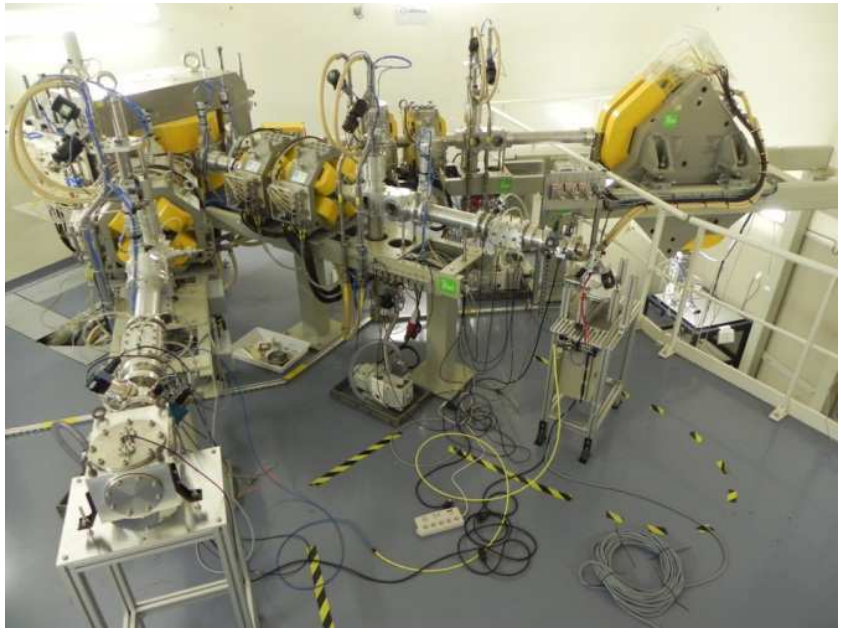

Figure 3.7: ARRONAX experimental vault, at the top right in Fig. 3.6

.

Figure 3.8: ARRONAX experimental irradiation station.

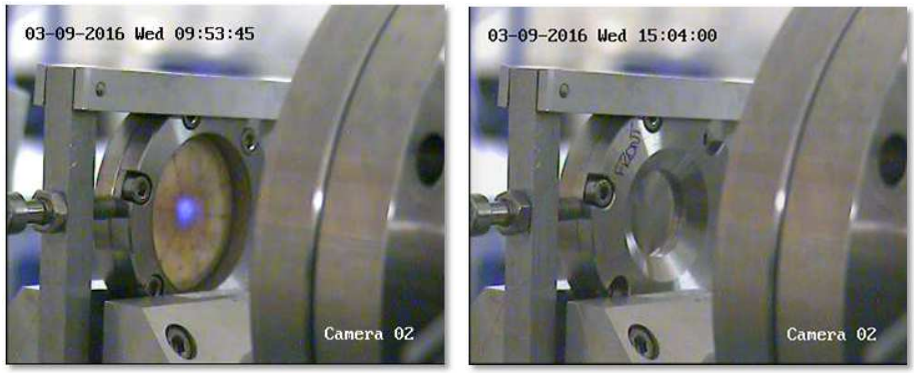

(a) Alumina foil (b) Target

Figure 3.9: ARRONAX experimental irradiation station.

homogenic way the target. Unfortunately, this is very difficult to obtain and, in my irradiations, I tested the distribution of the beam on the targets by the "picture" of the beam done with a suitable instrumentation.

3.3.1 Cyclone

The Perkin Elmer Cyclone storage phosphor system (Fig. 3.10) performs filmless autoradiographies. Reusable storage phosphor screens capture and store the activity of samples which are exposed, as with film, in common film cassettes.

The screens are scanned by a laser focused to less than $50\,\mu m$, and the latent image is detected by unique confocal optics to create a high resolution digitized image with quantitative data in the form of an image file.

Samples are exposed to the phosphor screens, which store energy in the photostimulable plate (PSP, $BaFBr : Eu^{2+}$). The ability of this phosphor to act as an image storage device relies on the presence of the Eu^{2+} dopant, the presence of naturally occurring point defects in the crystal lattice, and a phenomena known as Photostimulable Luminescence (PSL). When X or γ-rays are incident on the phosphor they may further ionize the Eu^{2+} cations to Eu^{3+}. The fast electrons so produced populate the conduction band from where they may either drop back to recombine with Eu^{3+} cations or become trapped in "colour centres".

The colour centres of interest in PSL are known as F-centres and are caused by the absence of halogen anions from their designated position in the $BaFBr$ lattice.

Figure 3.10: Perkin Elmer Cyclone.

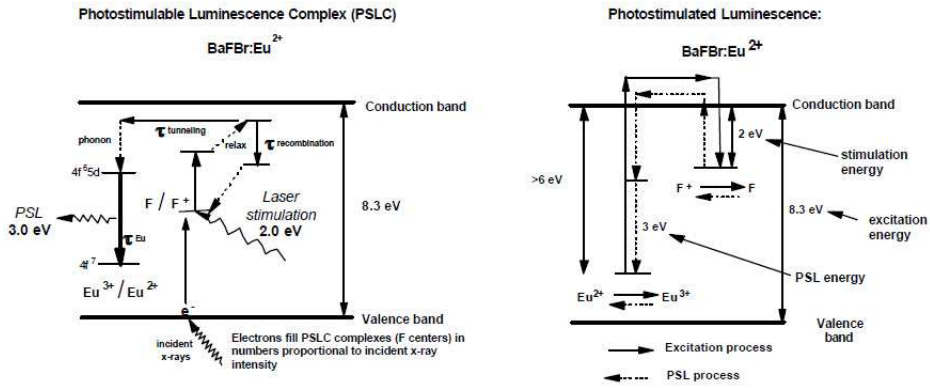

Figure 3.11: An energy diagram of the excitation and photo-stimulated luminescence processes in a $BaFBr : Eu^{2+}$ phosphor. On the left, is the representation of the interactions proposed by von Seggern. On the right, is the energy diagram proposed by Takahashi. Incident X or γ-rays form an "electron" latent image in a meta-stable F-center site that can be processed with a low energy laser beam, producing the desired luminescent signals. τ is the decay constant of the process indicated above.

A F-Center is a type of crystallographic defect in which an anionic vacancy in a crystal is filled by one or more electrons, depending on the charge of the missing ion in the crystal. Electrons in such a vacancy tend to light in the visible spectrum, so that a material that is usually transparent becomes coloured. Thus the origin of the name, F-center, which originates from the German *Farbzentrum*.
The translation of this term also provides the synonym color center, which can also refer to such defects. F-centres are often paramagnetic and can then be studied by electron paramagnetic resonance techniques. The resulting F^+-centres are long lifetime traps into which electrons, having enough energy to enter the conduction band, may fall. Once an electron becomes trapped in a F-center it may stay in that meta-stable state until it is excited again into the conduction band by exposure to laser light at $633\,nm$. From this point it may either fall back into an F-center or recombine with Eu^{3+} cations with the emission of blue light at around $390\,nm$ which is detected by a high quantum efficiency photomultiplier tube (PMT).

The important factors which make this phosphor suitable as an image storage device are:

- the number of F-centres populated by electrons from the excitation process is proportional to the received dose;
- the intensity of the luminescent light under PSL is proportional to the number of F-centres containing trapped electrons;
- the F-centres created by radiation are generally long-lived with a time con-

stant of around a few hours at normal operating temperatures.

There are currently two major theories for the PSP energy absorption process and the subsequent formation of luminescence centres. These include a bimolecular recombination model [Takahashi et al., 1984], and a photostimulated luminescence complex (PSLC) model [Von Seggern et al., 1988] shown in Figure 3.11. Physical processes occurring in $BaFBr : Eu^{2+}$, using the latter model appear to closely approximate the experimental findings. In this model, the PSLC is a metastable complex at a higher energy (F-center) in close proximity to an $Eu^{3+} - Eu^{2+}$ recombination center. X or γ-rays absorbed in the PSP induce the formation of "holes" and "electrons", which activate an "inactive PSLC" by being captured by an F-center, or form an active PSLC by formation and/or recombination of "exitons" explained by F-center physics [Von Seggern et al., 1988]. In either situation, the number of active PSLCs created (number of electrons trapped in the metastable site) are proportional to the X or γ-ray dose to the phosphor.

3.3.2 Beam "picture"

The beam picture was obtained in this way: the irradiated target was placed on the Cyclone plate for some minutes in a completely dark room. Then, after this exposure, the plate was analysed. It is important to stress that the beam shape changes in each irradiation and this is demonstrated by the my beams "picture" that show that the profile is not flat and repeatable.

In Figure 3.12, one of the JRC-Ispra irradiations, the activity distribution is not uniform (the z-axis is the Cyclone unit Digital Light Unit, DLU), but it is quite spread all along the diameter of the collimator even through there is a region with a greater concentration of charge.
Also in Figure 3.13, two of the ARRONAX irradiations, the activity distribution is not uniform. This may be due to the fact that the last collimator is not so close to the target.

In any case, in the activity evaluation I chose to keep the source-detector distance sufficiently high to prevent possible mistakes due to the non-point-like beam shape and, consequently, to the activity distribution.

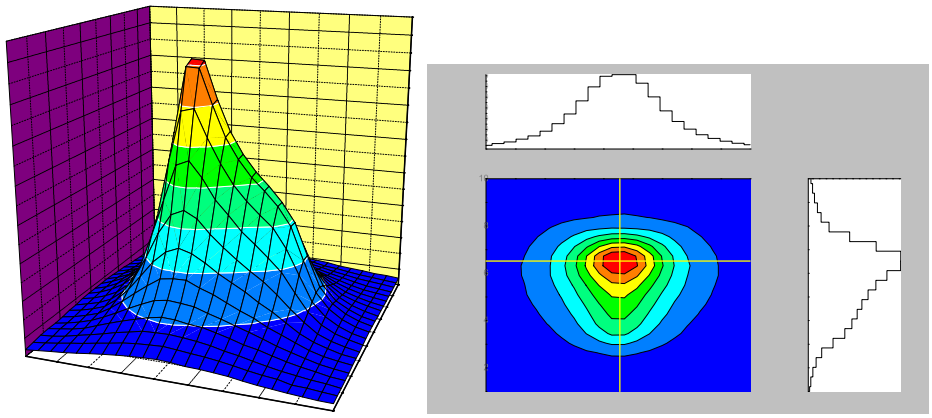

(a) 3D beam profile.

(b) 2D beam profile.

Figure 3.12: Beam "picture" of one of the JRC-Ispra irradiation.

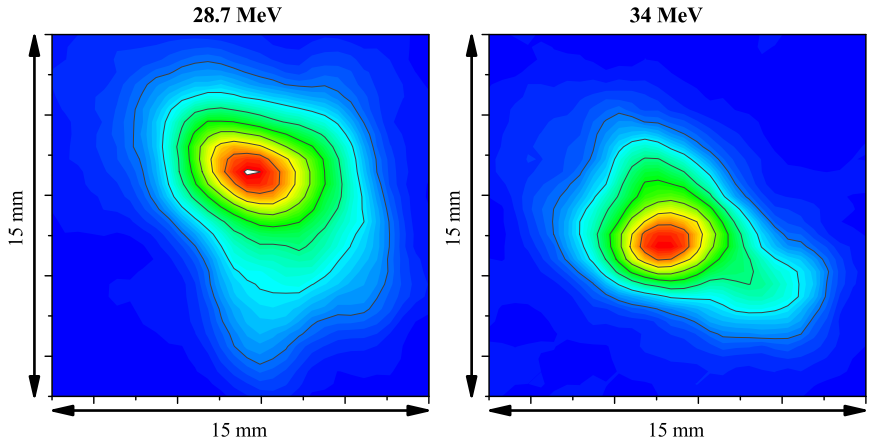

(a) 28.4 MeV irradiation

(b) 34 MeV irradiation

Figure 3.13: Beam "picture" of two of the ARRONAX irradiation.

Chapter 4

The excitation functions of ^{100}Mo(p,x)^{99}Mo and ^{100}Mo(p,2n)^{99m}Tc nuclear reactions[1]

4.1 Introduction

^{99m}Tc is the most used radiotracer in nuclear medicine. This is due to multiple advantages, not only from a physical and chemical point of view but also because it is conveniently available through a ^{99}Mo/^{99m}Tc generator system [Vértes et al., 2011].

In recent years there was a worldwide shortage of ^{99}Mo/^{99m}Tc, which is produced in highly enriched uranium targets via fission of ^{235}U in nuclear reactors [Council of the European Union, 2010]. This shortage boosted the interest in verifying alternative routes [Nuclear Energy Agency, 2010, Wolterbeek et al., 2014]. One method is the cyclotron production of ^{99m}Tc via the ^{100}Mo(p,2n)^{99m}Tc nuclear reaction.

As reported recently [Qaim et al., 2014] there are large discrepancies in published data concerning the reaction cross section for the reaction ^{100}Mo(p,2n)^{99m}Tc [Alharbi et al., 2011, Challan et al., 2007, Gagnon et al., 2011, Khandaker et al., 2007, Lagunas-Solar, 1999, Lagunas-Solar et al., 1991, Lebeda and Pruszyński,

[1] A large part of this chapter was published in Manenti et al. [2014]

2010, Levkovski, 1991, Scholten et al., 1999, Takács et al., 2003, Tárkányi et al., 2012, Wenrong et al., 1998].

Thus, the main goal of this work is to elucidate the discrepancies in literature by a careful determination of the excitation functions of the nuclear reactions ^{100}Mo(p,2n)^{99m}Tc and ^{100}Mo(p,x)^{99}Mo.

A particular emphasis is layed on an analysis of all the aspects involved in the determination of the ^{100}Mo(p,2n)^{99m}Tc cross-section in order to try to find an explanation for the scatter of previously published data.

4.2 Experimental

I determined the excitation functions using the stacked-foil technique covering the proton energy range from 8 MeV to 21 MeV. Stacks of thin foils consist of alternating high purity aluminium (as energy degrader foils inserted between Mo targets), highly enriched molybdenum ^{100}Mo and one titanium foil. In particular each stack was composed of the same number of Mo and Al foils, i.e. four or five depending on the irradiation energy, and by a Ti foil, inserted as final monitor foil in the stack. ^{100}Mo targets (0.08 % ^{92}Mo, 0.05 % ^{94}Mo, 0.1 % ^{95}Mo, 0.11 % ^{96}Mo, 0.07 % ^{97}Mo, 0.54 % ^{98}Mo, 99.05 % ^{100}Mo; Isoflex Isotopes, San Francisco, CA, USA) were prepared with a nominal thickness of 20–25 μm ($\sim$0.020–0.025 g·cm^{-2} and a general relative uncertainty of $\pm$2 %) in the nuclear target laboratory of the Legnaro National Laboratory of National Institute of Nuclear Physics, Italy (LNL-INFN), from ^{100}Mo purchased as metallic powder. The powder was pressed to get small pellets. The pellets were molten under vacuum by an electron beam and cooled slowly in a nitrogen atmosphere. Due to the high surface tension of the molten Mo, the initially flat pellet got a spherical shape during electron beam melting. Then, the spherical pellets were laminated using the pack-rolling technique into the required foil thickness. The true value of target thickness was measured accurately by weighing.

All irradiations were carried out with the cyclotron (Scanditronix MC40, K = 38, beam current up to 60 μA) of the JRC-Ispra at different incident energies with a constant current of about 100 nA for a duration of 1 hour. The excitation functions were obtained from seven foil stacks irradiated in seven different irradiation experiments.

Each irradiation took place in an insulated target holder under vacuum, which was designed as an elongated Faraday cup to determine the integrated charge of the proton beam. In the Faraday cup a strong magnet was installed to avoid escaping of scattered or backscattered electrons as the loss of such electrons could lead to a

virtually larger proton dose on the foil stacks. Two coaxial Al collimators (5 mm in diameter) were placed in front of the Faraday cup. Based on the distance between the collimators and from the last couple of quadrupoles a maximum broadening the beam of a few μm was calculated. The charge was integrated by a current integrator (BIC Brookhaven Instruments Corporation, Austin, TX, USA; model 1000C), calibrated within 2 % uncertainty by an authorized calibration service (Nemko S.p.A., Biassono, MB, Italy): in my experiment I use the experimentally measured charge.

The reliability of the integrated current has been validated by the values of the cross sections measured for ^{nat}Ti targets used as monitor foils, compared with the IAEA tabulated monitor reaction ^{nat}Ti(p,x)^{48}V [Tárkányi et al., 2001]. The extracted beam energy, calibrated by a cross-over technique, has an uncertainty of 0.2 MeV [Birattari et al., 1992]. Mean proton beam energy and energy degradation in each foil were computed by the Monte Carlo based computer code SRIM 2013 [Ziegler et al., 2010]. The uncertainty of the mean energy in each foil (± 0.25–0.44 MeV) includes the energy uncertainty of the extracted proton beam energy, the uncertainties in the mean mass thicknesses and the beam-energy straggling through the target foils (± 0.1–0.3 MeV). The activity was measured, without any chemical processing, by calibrated high purity germanium (HPGe) detectors (EG&G Ortec, 15 % relative efficiency, FWHM = 2.2 keV at 1.33 MeV). The first measurements of the samples were generally started within a few hours after end of bombardment (EOB) and measurements continued periodically for about one month to follow the decay of molybdenum-99: in general the counts in the peak in the region of interest exceed 10 000.

The overall uncertainty of the determined cross-sections is caused by several error sources in the measurement and evaluation process. Regarding the measurement process, a typical component is related to the statistical error in the peak counts: particular attention is given to reduce this value below 1 %. All foils were measured in the same geometrical position as that used for the calibrated sources in the energy and efficiency calibration of the detectors in order to avoid corrections for different geometries. The distance from the detector cap was sufficiently high to reduce dead time and pile up errors to negligible values (< 0.1 %). Other significant error sources were: the target thickness and uniformity (< 2 %), the integrated charge (< 2 %), the calibration sources uncertainty (1.5 % and 2.0 %) and the fitting of the detector efficiency curves (< 1 %), with a typical overall relative error of 4.5 %.

The published data about the abundance of the gamma emissions and the half-lives were considered as being exact. Decay characteristics for the radionuclides investigated, as summarized in Table 4.1, were taken from Browne and Tuli [2011],

Table 4.1: Decay data [Browne and Tuli, 2011] of ^{99m}Tc and ^{99}Mo radionuclides and contributing reactions. Branching ratio (BR) is reported from ICRP [2008]. Energy threshold (E_{th}) evaluation is based on Wang et al. [2012]

Nuclide	$t_{1/2}$ (h)	Contributing reactions	E_{th} (MeV)	E_γ (keV)	I_γ (%)
^{99}Mo	65.949	^{100}Mo(p,x)^{99}Mo	6.13	140.511	5.1 *
		^{99}Nb$\rightarrow^{99}$Mo †		181.1	6.142
^{99m}Tc‡	6.0067	^{100}Mo(p,2n)^{99m}Tc	7.79	140.511	89
		^{99}Mo$\xrightarrow{BR=87.73\,\%}{}^{99m}$Tc		142.684	0.02225

*see section 4.3.2
†^{100}Mo(p,2p)$^{99(m,g)}$Nb, E_{th}=11.26 MeV
‡It is impossible to distinguish the 140.511 keV peak from the 142.63 keV one. We use the cumulative intensities: 89.022 %.

ICRP [2008] and Wang et al. [2012].

4.3 Results and Discussion

The foils of the stacked foil targets were measured, positioning them on the detector with the beam-on side showing towards the detector cup. The experimental cross-sections σ(E) [cm^2 ≡ 10^{27} mb] for each target were calculated from the thin-target yield by the relationship [Bonardi, 1987]:

$$\sigma(E) = y_{\mathrm{EOIB}}(E) \cdot \frac{M \cdot Z \cdot e \cdot \Delta E}{\lambda \cdot N_{\mathrm{A}} \cdot \rho \Delta x} \tag{4.1}$$

where $y_{\mathrm{EOIB}}(E)$ is the thin-target yield [Bq·(C·Mev)$^{-1}$] at the End Of Instantaneous Bombardment, M denotes the atomic mass [g·mol^{-1}], $E = \langle E \rangle$ is the "average" proton beam energy in the "thin" target [MeV], e the electron charge [C], Z the atomic number of the projectile, ΔE the beam energy loss in the target [MeV], λ the decay constant [s^{-1}] of the investigated nuclide, N_{A} Avogadro's constant [mol^{-1}] and $\rho\Delta x$ the mass thickness [g·cm^{-2}].
$y_{\mathrm{EOIB}}(E)$ was calculated by the equation:

$$y_{\mathrm{EOIB}}(E) = \frac{COUNTS_\gamma}{\varepsilon_\gamma \cdot I_\gamma \cdot LT} \cdot \frac{1}{Q \cdot \Delta E} \cdot D(RT) \cdot G(t_{\mathrm{irr}}) \cdot e^{\lambda \cdot \Delta t} \tag{4.2}$$

where Q is the integrated proton charge [C] (obtained from Faraday cup read-out and confirmed by beam monitor reactions), $COUNTS_\gamma$ denotes the net photo-peak counts at energy E_γ above the continuum background, I_γ the γ-emission absolute abundance, ε_γ the experimental efficiency of the HPGe detector at the γ-energy

Table 4.2: Experimental cross-sections (1SD) of the ^{100}Mo(p,2n)^{99m}Tc and ^{100}Mo(p,x)^{99}Mo reactions

Energy (MeV)	^{99}Mo (mb)	^{99m}Tc (mb)
8.12 ± 0.34		0.27 ± 0.01
9.40 ± 0.29		84.20 ± 3.90
10.58 ± 0.25	0.38 ± 0.02	187.56 ± 8.68
11.07 ± 0.37	0.77 ± 0.04	230.44 ± 10.55
12.12 ± 0.33	4.89 ± 0.20	297.30 ± 13.61
12.69 ± 0.34	8.40 ± 0.42	306.29 ± 14.02
13.12 ± 0.30	12.40 ± 0.50	303.84 ± 13.91
13.65 ± 0.20	17.17 ± 0.94	322.90 ± 14.78
14.03 ± 0.38	21.41 ± 1.01	311.09 ± 14.28
14.60 ± 0.36	29.83 ± 1.40	307.79 ± 14.09
15.12 ± 0.43	38.59 ± 1.80	315.15 ± 14.43
15.16 ± 0.41	42.42 ± 1.96	320.87 ± 14.69
15.65 ± 0.41	45.95 ± 2.13	291.34 ± 13.34
16.18 ± 0.38	55.28 ± 2.55	292.15 ± 13.38
16.70 ± 0.36	66.25 ± 3.06	298.35 ± 13.66
16.84 ± 0.44	66.53 ± 3.05	306.98 ± 14.05
17.59 ± 0.41	79.41 ± 3.64	296.30 ± 13.57
17.76 ± 0.44	90.17 ± 4.15	294.03 ± 13.46
18.05 ± 0.39	94.55 ± 4.33	302.88 ± 13.87
18.77 ± 0.42	104.17 ± 4.78	269.70 ± 12.35
19.74 ± 0.40	119.46 ± 5.49	240.59 ± 11.02
20.85 ± 0.43	153.07 ± 7.02	195.14 ± 8.94

considered, LT the Live counting Time [s], RT the Real counting Time =LT + DT [s] (where DT is the Dead counting Time), Δt the waiting time from the EOB [s], t_{irr} the Irradiation Time [s]. The non-dimensional quantities $D(RT)$ (the decay factor to correct decay during counting time) and $G(\tau)$ (the growing factor to correct decay during irradiation) are defined as:

$$D(RT) = \frac{\lambda \cdot RT}{1 - e^{-\lambda \cdot RT}} \tag{4.3}$$

and

$$G(t_{\mathrm{irr}}) = \frac{\lambda \cdot t_{\mathrm{irr}}}{1 - e^{-\lambda \cdot t_{\mathrm{irr}}}}. \tag{4.4}$$

I give the experimentally determined cross sections of the ^{100}Mo(p,2n)^{99m}Tc and ^{100}Mo(p,x)^{99}Mo nuclear reactions in Table 4.2.

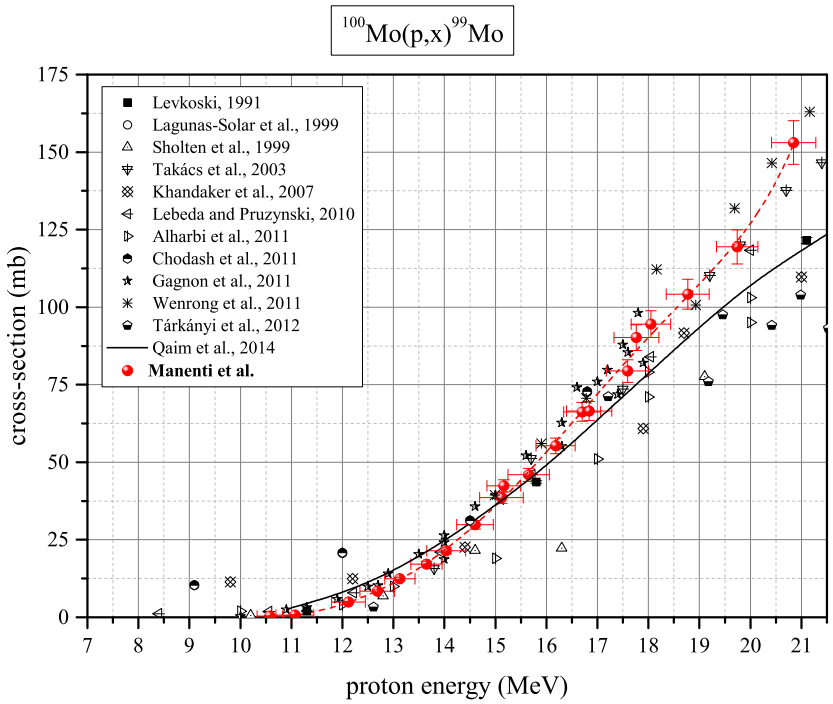

Figure 4.1: Excitation functions for $^{100}Mo(p,x)^{99}Mo$ nuclear reactions. For clarity, literature data are presented without error bars. Only my presented data have been fitted with a polinomial curve (- - -).

The measured excitation functions are shown in Figures 4.1 and 4.3.

4.3.1 ^{99}Mo

In addition to the direct formation of ^{99}Mo, the ^{99}Mo cross-section contains also the contributions of $^{100}Mo(p,2p)^{99(m,g)}Nb$ (respectively $t_{1/2}$ = 2.6 m and $t_{1/2}$ = 15 s) after the total decay of the $^{99(m,g)}Nb$. The cross-section values presented here are normalized to targets consisting of 100 % enriched ^{100}Mo.

General agreement is noted when comparing my data with Takács et al. [2003], Gagnon et al. [2011] and Lebeda and Pruszyński [2010]. Some disagreement at higher energies may be justified if the contribution of the $^{100}Mo(p,2p)^{99(m,g)}Nb$ (E_{th}=11.26 MeV) nuclear reaction has not been taken into account. This contribution depends on the irradiation time and on the enrichment in ^{100}Mo of the target. In my case, due to the $^{99(m,g)}Nb$ very short half-life, the evaluation of $^{100}Mo(p,2p)^{99(m,g)}Nb$ cross section was not possible.

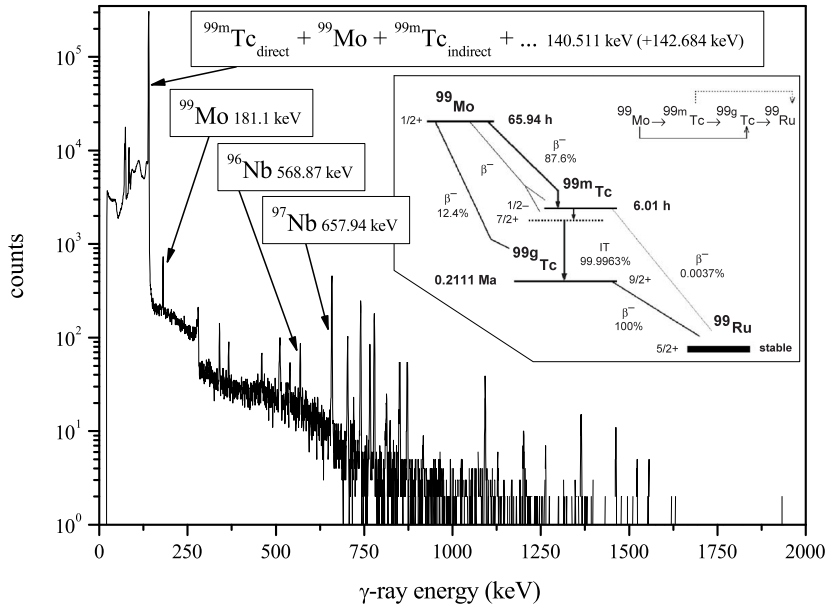

Figure 4.2: Example of a γ-ray spectrum. The picture reports the emissions used to determine the activity. The other emissions belong to: ^{96}Nb/^{96}Tc, ^{95}Nb/^{95}Tc, ^{94}Nb/^{94}Tc, ^{93g}Tc produced by the isotopes of molybdenum contained in the target in a non-natural abundance and ^{99}Rh and ^{100}Rh produced by the impurities contained in the target.

4.3.2 Determination of the absolute intensity 140.511 keV γ-ray emission of ^{99}Mo

The decay chain of ^{99}Mo and ^{99m}Tc creates a problem in the determination of the intensities of γ-rays: in this case the parent nuclide decays to the ground state of the daughter through the isomer and at the same time bypassing it (Fig. 4.2). In the previous papers, not all the author took in consideration this aspect and the value of the absolute intensity of the 140.511 keV γ-ray of ^{99}Mo was very scattered ranging from an unknown value to 89.43 % (Table 4.3). On the other hand, this value is important for the considerations presented in section 4.3.3. So I evaluated this decay characteristic of ^{99}Mo when it is in equilibrium with ^{99m}Tc and I took the 181.1 keV γ-ray of ^{99}Mo as internal reference to calculate this relevant 140.511 keV line intensity.

The absolute intensity of the 140.511 keV γ-ray of ^{99}Mo ($I^{Mo}_{140.5}$) is given by

$$I^{Mo}_{140.5} = \frac{COUNTS^{tot}_{140}}{COUNTS^{Mo}_{181}} \cdot \frac{\varepsilon_{181}}{\varepsilon_{140.5}} \cdot I^{Mo}_{181} - \frac{t^{Mo}_{1/2}}{t^{Mo}_{1/2} - t^{Tc}_{1/2}} \cdot BR \cdot I^{Tc}_{140.5} \qquad (4.5)$$

where ε is the HPGe efficiency at the indicated energy, I^{Mo}_{181} is the absolute intensity

of the 181 keV γ-ray of ^{99}Mo, BR is the branching ratio for the ^{99}Mo decay to the ground state of the daughter through the isomer ^{99m}Tc (BR = 87.73 %, Table 4.1) and Mo and Tc are used as abbreviations for ^{99}Mo and ^{99m}Tc.

In this manner, I experimentally obtained the value of 5.1 ± 0.2 % that is equal to the one measured by Chen et al. [1985]: 5.10 ± 0.16 %.

4.3.3 ^{99m}Tc

The determination of the ^{100}Mo(p,2n)^{99m}Tc cross-section is not a trivial topic. In fact, ^{99m}Tc emits only 140.511 keV and 142.63 keV photons and, as seen in section 4.3.2, there is the contribution of the same gamma emission due to the decay of ^{99}Mo.

Furthermore there is a contribution for the indirect production of ^{99m}Tc as a result of ^{99}Mo decay, both during and post irradiation and a possible contribution for the production of ^{90}Nb.

^{90}Nb has main γ-emissions of 141.2 keV (69.0 %) and 1129.1 keV (92.0 %) and can be produced via the nuclear reactions ^{92}Mo(p,dp+2pn)^{90}Nb (E_{th}=17.47 MeV), ^{94}Mo(p,αn)^{90}Nb (E_{th}= 9.05 MeV) and ^{95}Mo(p,α2n)^{90}Nb (E_{th}= 16.50 MeV).

In my experiment, I didn't found evidence of the presence of the 1129.1 keV γ-emission and, for the $E_{p,max}$=21 MeV, ^{90}Nb has an activity limit [Gilmore, 2008, section 5.6] at the EOB equal to 150 Bq, i.e. less than 0.007 % of the ^{99m}Tc activity: this may be due to the small amount of contributing molybdenum isotopes.

So for the evaluation of the ^{100}Mo(p,2n)^{99m}Tc cross-section, $COUNTS_\gamma$ in equation 4.2 is given by:

$$COUNTS^{Tc,dir} = COUNTS - (CF_1 + CF_2) \tag{4.6}$$

where CF_1 is the correction factor for the interference of the 140.511 keV peak arising directly from decay of ^{99}Mo and CF_2 is the correction factor for indirect production of ^{99m}Tc as a result of ^{99}Mo decay, both during and post irradiation. These correction factors can be calculated as

$$CF_1 = \frac{A^{Mo}_{EOIB} \cdot \varepsilon_{140.5} \cdot I^{Mo}_{140.5} \cdot LT}{D^{Mo}(RT) \cdot G^{Mo}(t_{irr})} \cdot e^{-\lambda^{Mo} \cdot \Delta t} \tag{4.7}$$

$$CF_2 = \frac{A^{Tc,ind}_{EOB} \cdot \varepsilon_{140.5} \cdot I^{Tc}_{140.5} \cdot LT}{D^{Tc}(RT) \cdot G^{Mo}(t_{irr})} \cdot e^{-\lambda^{Tc} \cdot \Delta t} \tag{4.8}$$

with

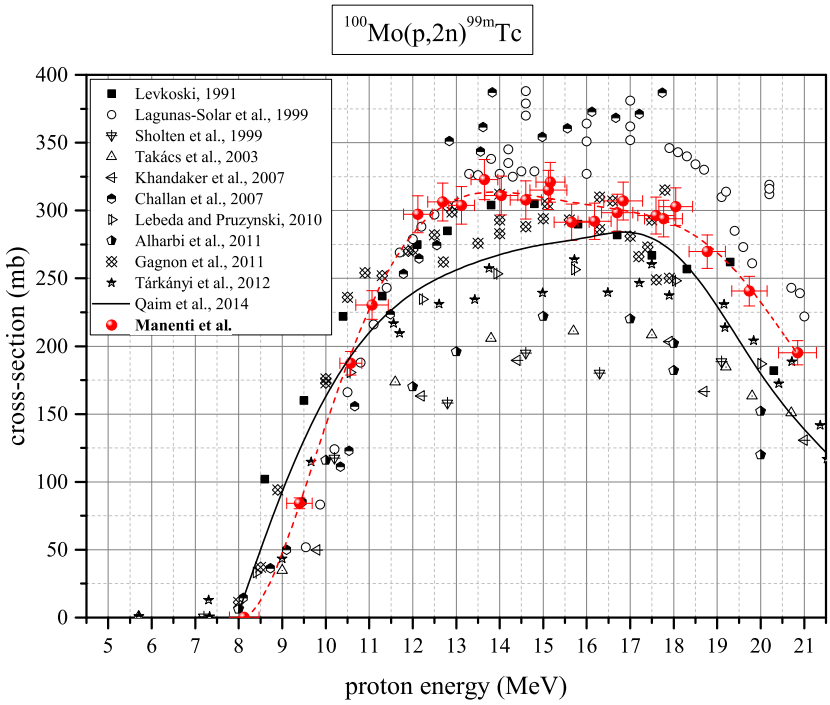

Figure 4.3: Excitation functions for ^{100}Mo(p,n)^{99m}Tc nuclear reactions. For clarity, literature data are presented without error bars. Only my presented data have been fitted with a polynomial curve (---).

$$A_{\mathrm{EOB}}^{Tc,ind} = BR \cdot A_{\mathrm{EOIB}}^{Mo}\left[\frac{\lambda^{Tc}}{\lambda^{Tc}-\lambda^{Mo}}\cdot\left(e^{-\lambda^{Mo}\cdot\Delta t}-e^{-\lambda^{Tc}\cdot\Delta t}\right)+\right.$$
$$+\frac{1}{1-e^{-\lambda^{Mo}\cdot t_{\mathrm{irr}}}}\left(1-\frac{\lambda^{Tc}}{\lambda^{Tc}-\lambda^{Mo}}\cdot e^{-\lambda^{Mo}\cdot t_{\mathrm{irr}}}+\right. \tag{4.9}$$
$$\left.\left.+\frac{\lambda^{Mo}}{\lambda^{Tc}-\lambda^{Mo}}\cdot e^{-\lambda^{Tc}\cdot t_{\mathrm{irr}}}\right)\right].$$

These equations differ from the expression published in Lebeda and Pruszyński [2010] and used in [Gagnon et al., 2011]: this is because I solve the exact differential equation starting from the EOIB and not from the EOB. I think that, in the experimental measurement of the cross section, the EOIB approach is the correct one, but, for short irradiations ($t_{\mathrm{irr}} \ll 1/\lambda^{Mo}$) the differences are negligible.

The numerical data of the cross-section are given in Table 4.2 and the measured excitation functions are shown in Figure 4.3.

A large disagreement is noted when comparing the present data with previously

Table 4.3: Relevant data: "–" is for an information not explicitly reported in the previous paper, "NA" is for the information not available, CF1 is the correction factor for the interference of the 140.511 keV peak (✓) and CF2 is the correction factor for indirect production of ^{99m}Tc as a result of ^{99}Mo decay, post irradiation (✓) or both during and post irradiation (✓✓). In the last two columns the are the energy and the maximum cross section.

	^{99m}Tc	^{99}Mo			corrections		maximum	
	$I^{Tc}_{140.5}$ (%)	$I^{Mo}_{140.5}$ (%)	I^{Mo}_{181} (%)	BR (%)	CF1	CF2	$E_p(\sigma_{max})$ (MeV)	σ_{max} (mb)
Lagunas-Solar et al. [1991]*	89.0†	88.7	6.3	87	–	–	∽17	∽290
Levkovski [1991]	–	–	–	–	–	–	∽15	∽305
Lagunas-Solar [1999]	89.0	88.7	6.3	87	✓	–	∽16.5	∽365
Scholten et al. [1999]	89.06	–	6.07	–	–	✓	∽17	∽200
Takács et al. [2003]	89	89.43	5.99	–	–	✓	∽16	∽210
Khandaker et al. [2007]	89.06	4.52	6.07	–	✓	✓	∽18	∽200
Challan et al. [2007]	89.06	–	–	–	–	–	13 – 18	350 – 380
Lebeda and Pruszyński [2010]	88.05	4.72	6.01	87.6	✓	✓✓	∽16	∽260
Alharbi et al. [2011]	89.06	89.43	5.99	–	✓	✓	∽15	∽220
Gagnon et al. [2011]	89.08	4.52	5.99	87.6	✓	✓✓	∽16	∽310
Tárkányi et al. [2012]	87.2	–	5.99	–	–	✓	∽16	∽260
Qaim et al. [2014]							16–17	∽280
this work	89.002	5.1	6.142	87.73	✓	✓✓	∽13.5 12–18	∽325 285–325

*this set is not reported in Figure 4.3

†in this paper is reported also a 143 keV γ-line with a I_γ=6.4 %

reported data. This may be due to (i) a inaccurate determination of the calibration curve (Ge detectors present maximum efficiency in the 140 keV region: this means that it is necessary to be sure of the values obtained from the fitting function, because it is not trivial to interpolate the data in this energy region), to (ii) the use of different nuclear data or to (iii) not taking into account the correction for the determination of the direct ^{99m}Tc production. In Table 4.3 I report the (i) and (ii) relevant data, if they are provided by papers author. In particular, a less poor agreement is noted when comparing only with Gagnon et al. [2011] and Levkovski [1991]. This is somewhat strange because Levkovski paper is one of the older and it is without details but, mainly to its minimality, it is not possible to say that he didn't apply corrections.
Moreover, the maxima of my experimental cross section are at lower energies than the evaluated curve in Qaim et al. [2014].

4.3.4 Thin and Thick Target Yield

In order to make some more quantitative considerations for the production of ^{99m}Tc and ^{99}Mo, it is useful to calculate the Thick-Target Yield $Y(E, \Delta E)$) that is defined as a two parameter function of incident particle energy E (MeV) on the target and energy loss in the target itself ΔE (MeV) [Bonardi et al., 2002] and holds in the approximation of a monochromatic beam of energy E not affected by either intrinsic energy spread or straggling.

I calculated the Thick-Target Yield for ^{99m}Tc and ^{99}Mo: the experimental thin-target yields of these radionuclides (Figg. 4.4 and 4.5) were fitted by the software TableCurve 2D for Windows (Systat Software Inc). These mathematical functions were integrated by MathCAD (PTC, USA) to bear the Thick-Target Yields in Figures 4.6 and 4.7.

In Figure 4.6 the calculated locus of maxima of Thick-Target Yield that corresponds to couples of optimised values $(E, \Delta E)$ is reported: this set of Thick-Target Yields allows to calculate the optimum irradiation conditions in order to have radiotracers with radionuclidic purity as high as possible.

Using Figures 4.6 and 4.7, it is possible to calculate the expected activity as function of t_{cool} and t_{irr} (e.g. Table 4.4).

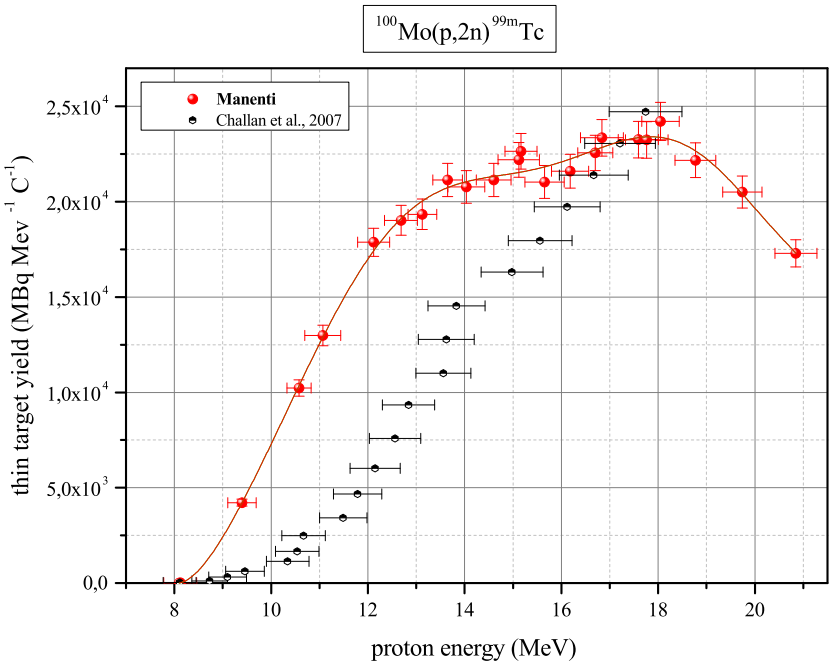

Figure 4.4: ^{99m}Tc experimental and fitted thin-target yield.

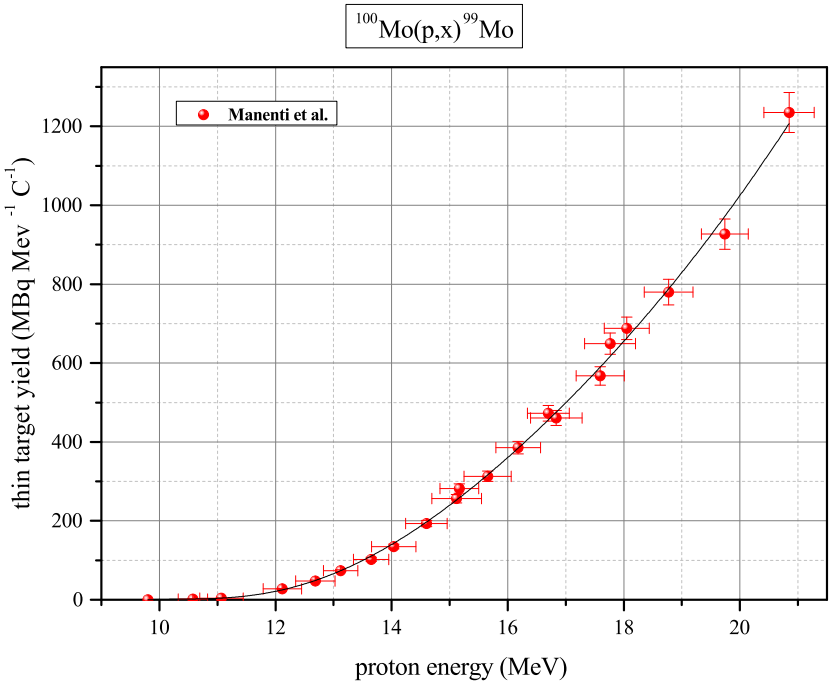

Figure 4.5: ^{99}Mo experimental and fitted thin-target yield.

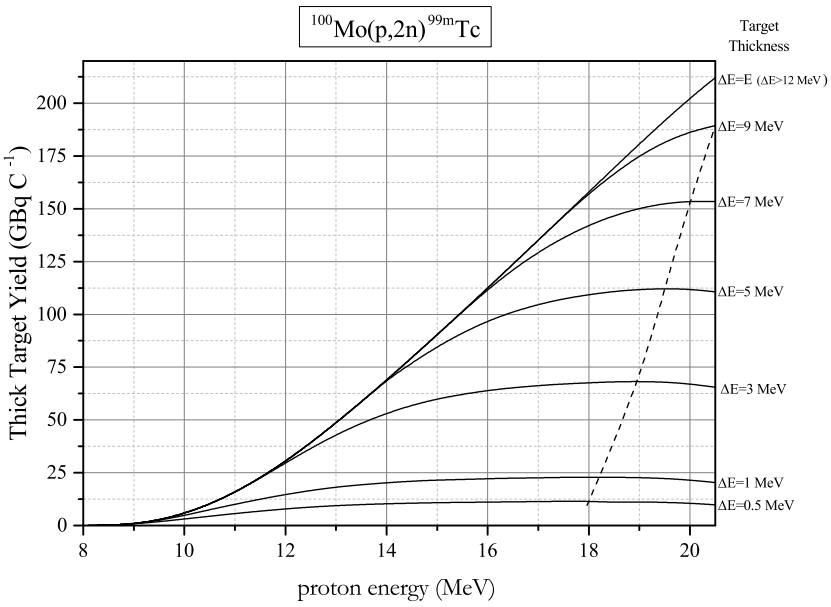

Figure 4.6: Calculated Thick-Target Yields for the production of ^{99m}Tc as a function of deuteron irradiation energy and different energy loss in the target (that corresponds to different target thickness).

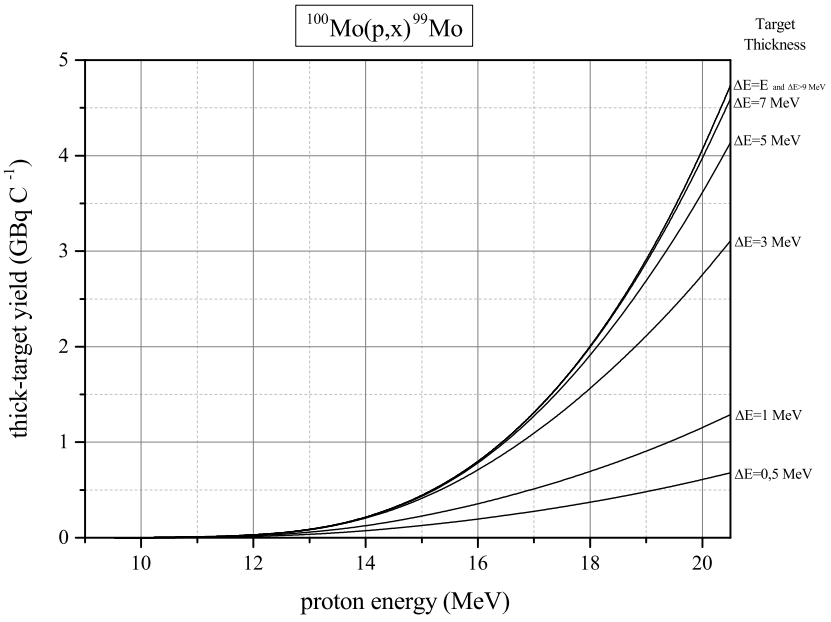

Figure 4.7: Calculated Thick-Target Yields for the production of ^{99}Mo as a function of deuteron irradiation energy and different energy loss in the target (that corresponds to different target thickness).

Table 4.4: ^{99m}Tc activity [GBq/100μA] for E = 14 MeV and ΔE = 5 MeV

		t_{cool} (h)				
		0 (EOB)	**1**	**2**	**4**	**8**
t_{irr} (h)	**1**	23.6	21.1	18.8	14.9	9.4
	2	44.7	39.8	35.5	28.2	17.8
	4	80.2	71.5	63.7	50.6	31.9
	8	130.8	116.5	103.8	82.5	52.0

Table 4.5: Decay data [Browne and Tuli, 2011, NNDC, 2016] of ^{99g}Tc, ^{96}Nb and ^{97g}Nb radionuclides and contributing reactions. Branching ratio (BR) is reported from ICRP [2008]. Energy threshold (E_{th}) evaluation is based on Wang et al. [2012]

Nuclide	$t_{1/2}$	Contributing reactions	E_{th} (MeV)	E_γ (keV)	I_γ (%)
^{96}Nb	23.35 h	^{100}Mo(p,αn)^{96}Nb	3.83	568.87	58.00
^{97}Nb	72.1 m	^{100}Mo(p,α)^{97g}Nb	0	657.94	98.23
		^{97m}Nb$\rightarrow$^{97g}Nb *			
^{99g}Tc	2.11×10^5 y	^{100}Mo(p,2n)^{99m}Tc	7.79	89.5	6.5×10^{-4}
		$^{99}\text{Mo} \xrightarrow{BR=12.27\%} {}^{99g}\text{Tc}$			
		^{99m}Tc$\rightarrow$^{99g}Tc			

*$t_{1/2}(^{97m}\text{Nb})$=58.7 s

4.3.5 Radionuclidic impurities: ^{96}Nb, ^{97g,cum}Nb and ^{99g}Tc

My main motivation for this earlier work was to assess the level of the co-produced ^{99g}Tc contaminant and compare the technetium specific activity of the cyclotron route to that which can be achieved with the current generator standard. Simultaneous to these initial irradiations to assess ^{99m}Tc and ^{99}Mo production following proton irradiation of enriched ^{100}Mo, I also evaluated the ^{100}Mo(p,2n)^{99g}Tc, ^{100}Mo(p,αn)^{96}Nb, and ^{100}Mo(p,α)^{97}Nb reaction cross sections. With the discussions relating to the quality of cyclotron-produced ^{99m}Tc, these side reactions are of great interest.

Decay characteristics for these radionuclides are summarized in Table 4.5.

Table 4.6: Experimental cross-sections (1SD) of the ^{100}Mo(p,αn)^{96}Nb, ^{100}Mo(p,α)^{97g,cum}Nb and ^{100}Mo(p,2n)^{99g}Tc

Energy (MeV)	^{96}Nb (mb)	^{97g}Nb (mb)	^{99g}Tc (mb)
8.12 ± 0.34		0,14 ± 0.01	
9.40 ± 0.29		0.68 ± 0.04	
10.58 ± 0.25		1.52 ± 0.08	
11.07 ± 0.37		1.95 ± 0.09	
12.12 ± 0.33		3.35 ± 0.16	
12.69 ± 0.34		3.86 ± 0.19	
13.12 ± 0.30		4.17 ± 0.20	
13.65 ± 0.20		5.08 ± 0.25	
14.03 ± 0.38	0.15 ± 0.02	5.11 ± 0.24	
14.60 ± 0.36	0.28 ± 0.02	5.50 ± 0.26	
15.12 ± 0.43	0.55 ± 0.03	6.11 ± 0.30	
15.16 ± 0.41	0.62 ± 0.04	6.08 ± 0.29	
15.65 ± 0.41	0.83 ± 0.04	5.37 ± 0.26	
16.18 ± 0.38	1.33 ± 0.07	5.75 ± 0.28	
16.70 ± 0.36	2.00 ± 0.10	5.95 ± 0.28	
16.84 ± 0.44	2.12 ± 0.10	6.14 ± 0.29	
17.59 ± 0.41	3.30 ± 0.16	5.83 ± 0.27	
17.76 ± 0.44			867.1 ± 57.6
18.05 ± 0.39	4.43 ± 0.21	6.15 ± 0.28	
19.74 ± 0.40			929.7 ± 61.1
20.85 ± 0.43			570.6 ± 44.2

In Table 4.6 there is the cross sections of the ^{100}Mo(p,2n)^{99g}Tc, ^{100}Mo(p,αn)^{96}Nb and ^{100}Mo(p,α)^{97g,cum}Nb nuclear reactions.

General agreement is noted (Figures 4.8 and 4.9) for both ^{96}Nb and ^{97g,cum}Nb when comparing my data with Levkovski [1991], Lebeda and Pruszyński [2010] and Gagnon et al. [2012].

4.3.5.1 ^{99g}Tc

While the production of ^{99m}Tc and ^{99}Mo may be quantified via γ-ray spectrometry using an HPGe detector, ^{99g}Tc does not emit any suitable γ-ray for analysis with this method. This mandated an alternative strategy for evaluating the ^{99g}Tc content and, ultimately, the excitation function. I utilized ICP-MS [Becker, 2003] for this study. The direct ^{99g}Tc excitation function was thus determined using ICP-MS in combination with γ-ray spectrometry to correct for the indirect ^{99g}Tc contribu-

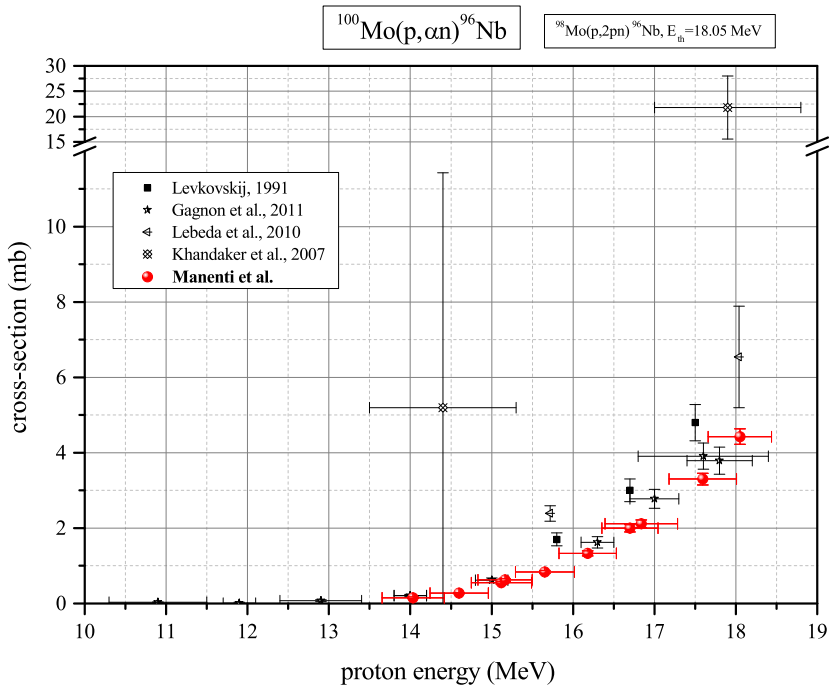

Figure 4.8: Excitation functions for ^{100}Mo(p,αn)^{96}Nb nuclear reactions.

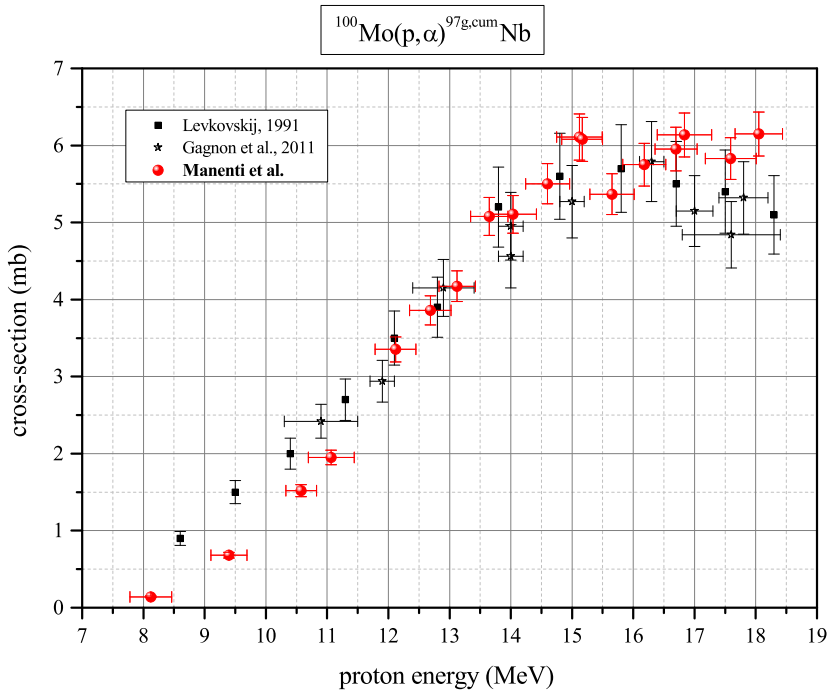

Figure 4.9: Excitation functions for ^{100}Mo(p,α)^{97g,cum}Nb nuclear reactions.

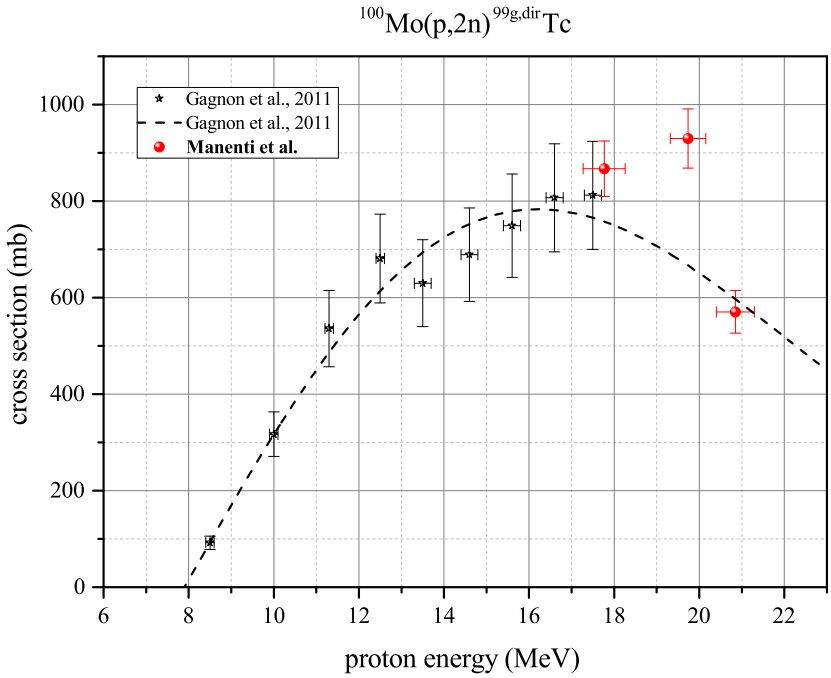

Figure 4.10: Excitation functions for ^{100}Mo(p,n)^{99g}Tc nuclear reactions.

tions following decay of ^{99m}Tc and ^{99}Mo: the samples were left to decay for more than one year to allow for complete decay of the ^{99m}Tc and ^{99}Mo reaction products.

To measure ^{99g}Tc, chemical separation of the technetium from the bulk of the ^{100}Mo was necessary.
Technetium was extracted from the bulk molybdenum of the irradiated foils by dissolution using 1 ml 30 % H_2O_2 and 3 ml 8N HNO_3 at 70 °C. Solutions were then basified by the addition of 6N NaOH. Liquid-liquid extraction was carried out by addition of 6 ml methyl ethyl ketone (MEK), an immiscible organic solvent, shaking of the solution and subsequent removal of the top 3 ml of the organic layer. Technetium oxide is soluble in MEK but not molybdenum oxide. After agitation, the MEK will float to the surface of the aqueous solution and can be removed, carrying with it the ^{99m}Tc. This process was repeated three times. Eventually, the MEK is evaporated leaving behind the technetium oxide.
These samples were measured by HR-ICP-MS at the Physics Department of the University of Milano Bicocca.

The experimentally measured ^{100}Mo(p,2n)^{99g,dir}Tc cross-section is summarized

in Figure 4.10. Due to technical problem, we were able to measure only three samples and only one is energetically close to the data in previous literature: it is in good agreement with that. Unlike the extrapolation of Gagnon et al. [2011], the cross-section seems to increase and then decrease rapidly at the energy of 19–20 MeV.

4.4 Conclusions

With this study, I presented an experimental verification of the reaction cross sections of the nuclear reactions ^{100}Mo(p,x)^{99}Mo and ^{100}Mo(p,2n)^{99m}Tc and I gave the solution of the exact differential equation starting from the EOIB.
It is my opinion that the best energy range range for the production of ^{99m}Tc via cyclotron route is 12–17 MeV. In fact, the cross section reaches its maximum value in this energy range. Furthermore, for energies higher than about 17 MeV there is a sharp increase of the side production of the long-lived radioisotopic impurities due to the production of ^{98}Tc (^{100}Mo(p,3n)^{98}Tc, E_{th}=16.85 MeV).

Chapter 5

The excitation functions of the ^{89}Y(d,2n)^{89}Zr nuclear reaction

5.1 Introduction

Zirconium-89 is one of the most promising radionuclides for labelling monoclonal antibodies, bio-distribution studies, and immuno-PET (positron emission tomography) imaging [Bansal et al., 2015, Brasse and Nonat, 2015, Deri et al., 2013, Knowles and Wu, 2012, Tolmachev and Stone-Elander, 2010].
Furthermore, a method to prepare simultaneously paramagnetic and pharmaceutical probes of ^{89}Zr-labelled octreotide liposomes for simultaneous PET and magnetic resonance tumour imaging capabilities has been reported [Abou et al., 2013].
^{89}Zr ($t_{1/2}$=78.41 h, Tab. 5.1) decays by positron emission (22.3 %) and electron capture (76.6 %) to the stable isotope ^{89}Y [Mustafa et al., 1988]. β^+ particle emission has a maximum decay energy of 900 keV.

The longer-lived isotope Zirconium-88, with a reasonably long half-life ($t_{1/2}$= 83.4 d) and single gamma-ray emission (392.87 keV), is the only radioisotopic impurity in ^{89}Zr produced by deuterons on ^{89}Y. It is used in extended experiments such as animal bio-distribution studies and pharmacokinetic behaviour of labelled antibodies [Meijs et al., 1997].
^{88}Zr also provides the opportunity to produce significant amounts of monoisotopic carrier free ^{88}Y from a ^{88}Zr/^{88}Y generator [Meijs et al., 1996].

Yttrium-88 ($t_{1/2}$=106.65 d) is produced in large scale for investigation of the

bio-distribution of ^{90}Y ($t_{1/2}$=64.1 h) labelled therapeutic compounds [Kobayashi et al., 1999], for gamma-ray detector calibration source and for dose determination in accelerator technology.

My work presents and discusses the experimental results with reference to the cross-sections of the $^{89}Y(d,2n)^{89}Zr$ reaction in the 6–18 MeV energy range. The earlier results for deuteron induced nuclear reactions on Y target were published by Baron and Cohen 1963, La Gamma and Nassiff 1973, Bissem et al. 1980, Degering et al. 1988, West et al. 1993, Uddin et al. 2007, Tárkányi et al. 2005 and Lebeda et al. 2015 and were rather scattered. Their data are compared with mine.

5.2 Experimental

I determined the excitation functions using the stacked-foil technique. Stacks of thin foils consist of alternating high purity aluminium (as energy degrader and monitor foils inserted between the Y and the Ti targets), yttrium and titanium foil. In particular each stack was composed of the same number of Y and Al foils, i.e. four or five depending on the irradiation energy, and by one Ti foils after each Y/Al foils in the stack.

^{89}Y targets (Goodfellow Cambridge Ltd., Ermine Business Park, Huntingdon PE29 6WR, UK) had a nominal thickness of 25 μm. The true value of target thickness was measured accurately by weighing: $\sim$12.37 mg·cm^{-2} and a relative uncertainty of $\pm$2 %.

The irradiations were carried out with the cyclotron of the ARRONAX center, Saint-Herblain (FR) (IBA C70). The ARRONAX cyclotron delivers a deuteron beam with an energy within $\pm$0.25 MeV [Haddad et al., 2008]. The stacks were irradiated with an external deuteron beam, delivered by the ARRONAX cyclotron. A 75 μm thick kapton foil closes the line and makes a barrier between the air in the vault and the vacuum in the beam line. The stacks were located 82 mm downstream in air.

Two stacks were irradiated with a different incident energy in order to minimize this energy dispersion and cover the energy range from 18 MeV down to 6 MeV. Irradiations were carried out with a mean beam intensity of about 180 nA for 1 h.

During irradiation, an instrumented beam stop was used to control the beam

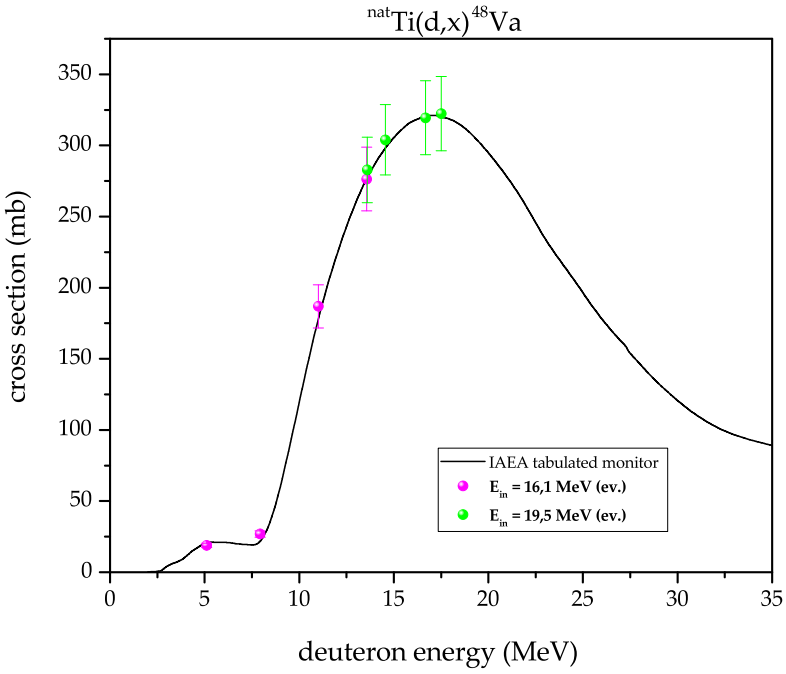

Figure 5.1: Excitation functions for ^{nat}Ti(p,x)^{48}V nuclear reactions.

current stability. However, it was not used as a Faraday cup with precise intensity measurements, since it is not under vacuum and is is not equipped with a device to avoid escaping of scattered or backscattered electrons.

In this case, the titanium and the aluminium foils were used also as monitors - ^{nat}Ti(p,x)^{48}V and ^{27}Al(d,x)^{24}Na reactions, IAEA tabulated monitor reactions [Tárkányi et al., 2001] - for the exact determination of beam intensity and energy (Figures 5.1 and 5.2).

Mean deuteron beam energy and energy degradation in each foil were computed by the Monte Carlo based computer code SRIM 2013 [Ziegler et al., 2010]. The uncertainty of the mean energy in each foil (± 0.2–0.4 MeV) includes the energy uncertainty of the extracted deuteron beam energy, the uncertainties in the mean mass thicknesses and the beam-energy straggling through the target foils (± 0.1–0.3 MeV).

The activity was measured at the LASA laboratory (INFN and Physics Dept. of University of Milan, Segrate MI), without any chemical processing, by calibrated high purity germanium (HPGe) detectors (EG&G Ortec, 15 % relative efficiency,

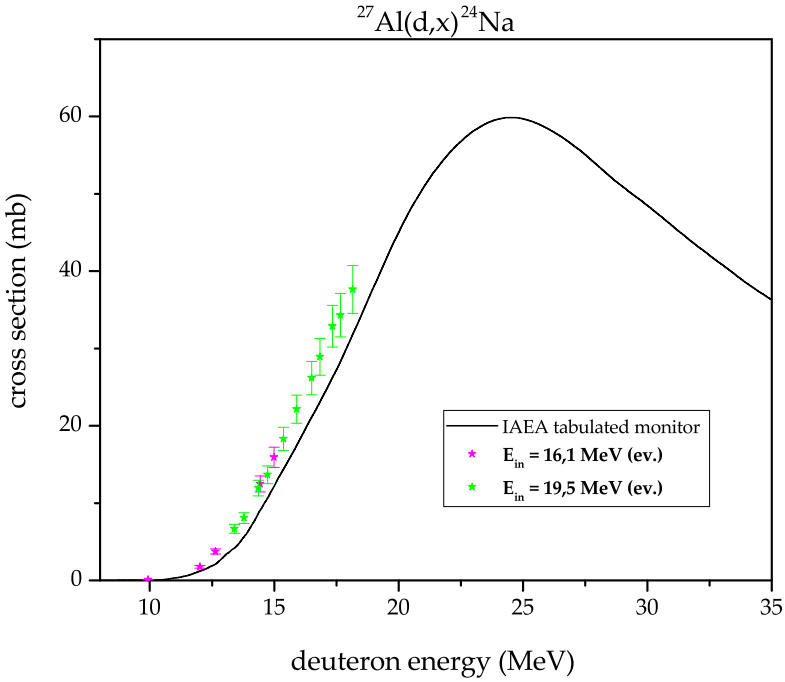

Figure 5.2: Excitation functions for ^{27}Al(d,x)^{24}Na nuclear reactions.

FWHM = 2.2 keV at 1.33 MeV). The first measurements of the samples were generally started within within 48 hours after end of bombardment (EOB) and measurements continued periodically for about six months (e.g. Fig. 5.3).

The overall uncertainty of the determined cross-sections is caused by several error sources in the measurement and evaluation process. All foils were measured in the same geometrical position as that used for the calibrated sources in the energy and efficiency calibration of the detectors in order to avoid corrections for different geometries. The distance from the detector cap was sufficiently high to reduce dead time and pile up errors to negligible values (< 0.1 %). Other significant error sources were: the target thickness and uniformity (< 2 %), the integrated charge (< 2 %), the calibration sources uncertainty (1.5 % and 2.0 %) and the fitting of the detector efficiency curves (< 1 %), with a overall relative error of 4–20 %.

The published data about the abundance of the gamma emissions and the half-lives were considered as being exact. Decay characteristics for the radionuclides investigated, as summarized in Table 5.1, were taken from Firestone et al. [1999] and Wang et al. [2012].

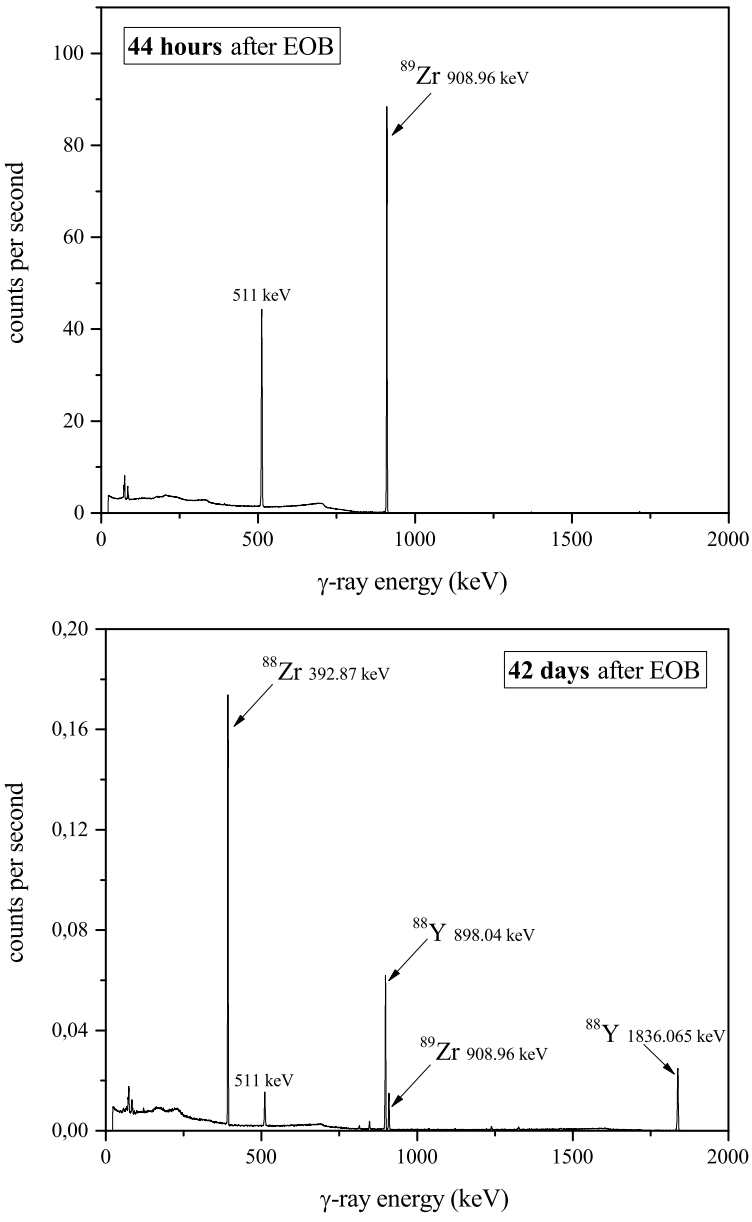

Figure 5.3: Examples of γ-ray spectra, E = 17.9 MeV.

5.3 Results

I show the measured excitation functions in Figures 5.4–5.6 in comparison with the literature data.The numerical data are collected in Table 5.2.

Table 5.1: Decay data [Firestone et al., 1999] of Zr and Y radionuclides and contributing reactions. The E_{th} evaluation is based on the mass defects of Wang et al. [2012].

Nuclide	$t_{1/2}$	Contributing reactions	E_{th} (MeV)	E_γ (keV)	I_γ (%)
^{90}Zr	stable	^{89}Y(d,n)^{90}Zr	0		
^{89}Zr	78.41 h	^{89}Y(d,2n)^{89}Zr	7.4	908.96	99.87
^{88}Zr	83.4 d	^{89}Y(d,3n)^{88}Zr	15.50	392.87	97.31
^{88}Y	106.65 d	^{89}Y(d,x)^{88}Y	5.34	898.04	93.7

Table 5.2: Experimental cross-sections (1SD) of the ^{89}Y(d,xn)^{89,88}Zr and ^{89}Y(d,x)^{88}Y reactions

Energy (MeV)	^{89}Zr (mb)	^{88}Zr (mb)	^{88}Y (mb)
6.03 ± 0.33	8.6 ± 0.7		
9.56 ± 0.23	445.7 ± 36.2		0.25 ± 0.02
12.33 ± 0.20	728.5 ± 59.2		3.8 ± 0.2
14.08 ± 0.25	857.1 ± 69.6		7.6 ± 0.4
14.71 ± 0.17	851.1 ± 69.1		8.6 ± 0.5
15.64 ± 0.23	865.6 ± 70.3	0.11 ± 0.02	9.9 ± 0.6
17.09 ± 0.22	895.3 ± 72.7	6.5 ± 0.5	14.8 ± 0.9
17.91 ± 0.21	901.2 ± 73.2	20.8 ± 1.7	21.5 ± 1.2

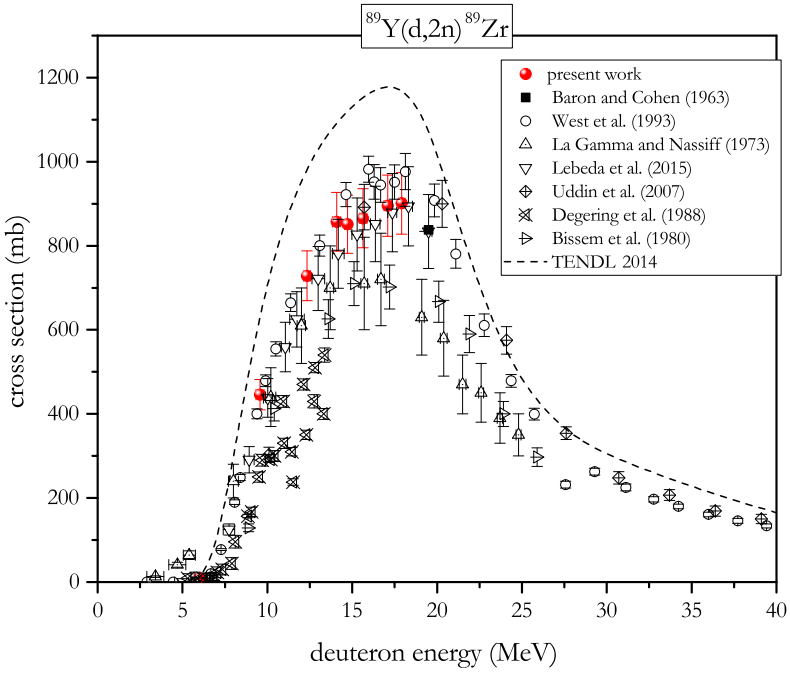

Figure 5.4: Excitation functions for ^{89}Y(d,2n)^{89}Zr nuclear reactions.

5.3.1 ^{89}Y(d,2n)^{89}Zr

^{89}Zr has a half-life of $t_{1/2}$ = 78.41 h and can be produced through the (d,2n) reaction. I assessed the activity through the 908.96 keV gamma line (I_γ = 99.87 %). ^{89}Zr has a short-lived isomer ^{89m}Zr ($t_{1/2}$ = 4.18 m, isomeric transition probability equal to 93.77 %) that was not measured: I measured a cumulative production of $^{89,m+g}$Zr.

The measured experimental cross-sections are shown in Figure 5.4 together with the data of the earlier study and curves of theoretical calculations with TALYS codes (TENDL-2014). My cross-sections are in good agreement with the results of Lebeda et al. 2015 and West et al. 1993. The prediction of TENDL-2014 is higher than all the experimental data.

5.3.2 ^{89}Y(d,3n)^{88}Zr

^{88}Zr has a half-life of $t_{1/2}$ = 83.4 d and can be produced through the (d,3n) reaction. The activity was assessed through the 392.87 keV gamma line (I_γ = 97.31 %).
My cross-sections (Fig. 5.5) are in good agreement with the two previous results in the same energy range [Lebeda et al., 2015, West et al., 1993]. The experimental

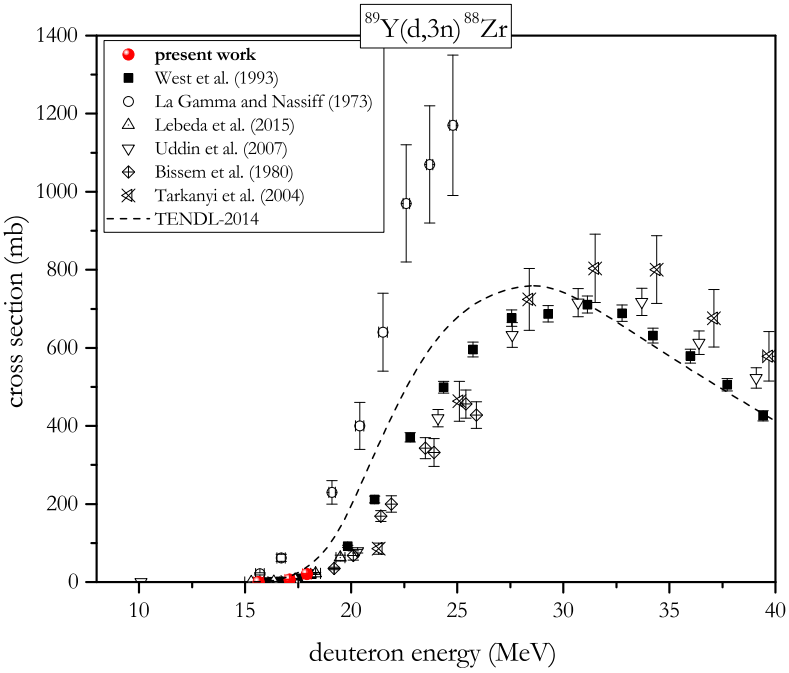

Figure 5.5: Excitation functions for $^{89}Y(d,3n)^{88}Zr$ nuclear reactions.

data in the studied energy range from the work of La Gamma and Nassiff [1973] are higher than mine, while data from Tárkányi et al. [2005] are lower.

5.3.3 $^{89}Y(d,x)^{88}Y$

^{88}Y can be produced through the (d,x) reactions.
^{88}Y has a half-life of $t_{1/2}$ = 106.65 d and the activity was assessed through the 898.04 keV gamma line (I_γ = 93.7 %).
My cross-sections are, in general, in good agreement with the results of Lebeda et al. 2015 and West et al. 1993 (Fig. 5.6). The experimental data in the studied energy range from the work of La Gamma and Nassiff [1973] and Uddin et al. [2007] are lower than mine, while data from Tárkányi et al. [2005] are higher. Also TENDL-2014 is lower than my experimental points.

5.4 Conclusions

^{89}Zr has a practical importance as it is widely used in the research of new radiotherapeutics. The present excitation curve allows for calculating and optimizing

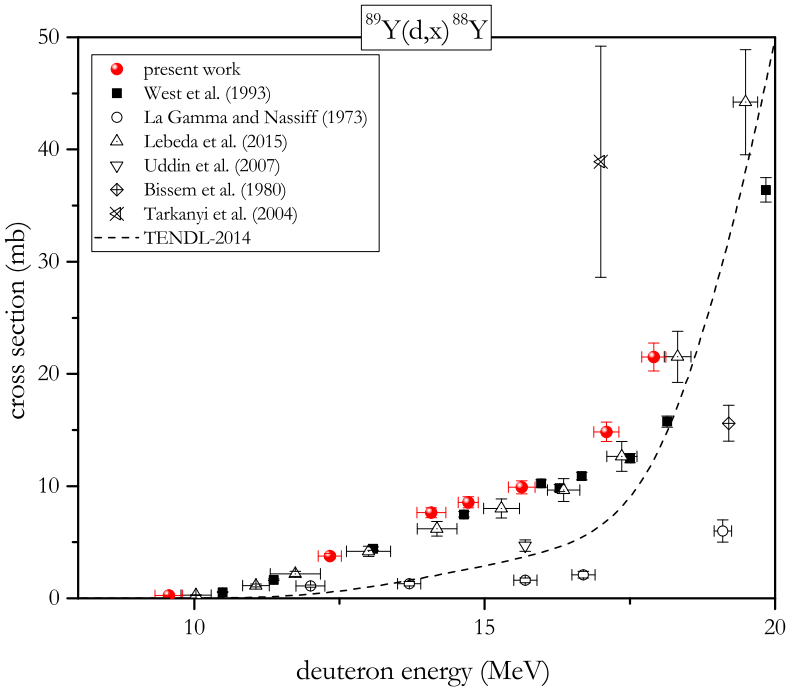

Figure 5.6: Excitation functions for ^{89}Y(d,x)^{88}Y nuclear reactions.

batch yields of this radionuclide.

I presented measurement of the excitation functions of the deuteron-induced reactions on ^{89}Y up to 18 MeV. Significant amounts of ^{89}Zr can be produced at low energy accelerators using yttrium as target and the possibility to involve radionuclidic impurities is very low in the energy range considered in this study.

Chapter 6

The excitation function and yield for the ^{103}Rh(d,2n)^{103}Pd nuclear reaction

6.1 Introduction

^{103}Pd ($t_{1/2}$=16.991 d [Firestone et al., 1999]) decays almost exclusively (99.90 %), by electron capture (EC) to ^{103m}Rh ($t_{1/2}$=56.12 min), which de-excites through internal transition (IT). As a result of these processes (EC and IT) Auger-electrons and X-rays are emitted which are ideally suited for therapy. Taking into account also the de-excitation of the "daughter" nuclide ^{103m}Rh, every 100 decays of ^{103}Pd are accompanied by the emission of about 263 Auger electrons, 188 low-energy conversion electrons and 97 X-rays National Nuclear Data Center [2016]. These decay features and the practical absence of high-energy γ-rays make ^{103}Pd particulary suitable for interstitial brachytherapy: encapsulated in millimetre-size seed implants it is used in prostate Yoshioka [2009], breast Pignol et al. [2006] or choroidal melanomas Semenova and Finger [2013] cancer brachytherapy.
It has been shown that gold nanoparticles (Au NPs) distributed in the vicinity of ^{103}Pd radioactive implants can act as radiosensitivers that strongly enhance the therapeutic dose of radioactive implants [Jones et al., 2010, Lechtman et al., 2011]. A new strategy under development to replace millimetre-size seeds [Moeendarbari et al., 2016], consist in injecting radioactive nanoparticles in the affected tissues. The development of ^{103}Pd@Au NPs distributed in the diseased tissue, could in-

crease the uniformity of the treatment compared to larger seeds, while enhancing the radiotherapeutic dose to the cancer cells through Au-mediated radiosensitisation effect.

The possibility to use this radionuclide for therapeutic purpose is strictly linked to the feasibility of increasing the Specific Activity (A_S, the ratio between the radioactivity and the mass of the sum of all radioactive and stable isotopes of the nuclide of interest de Goeij and Bonardi [2005a]), approaching the theoretical carrier free value of A_S(CF)=2.76 GBq·μg^{-1}.

Nowadays, ^{103}Pd can be produced in reactors via the ^{102}Pd(n,γ) reaction with a very low A_S or in no-carrier-added form with accelerators using proton induced reactions [INTERNATIONAL ATOMIC ENERGY AGENCY, 2006].

Irradiation of 100 % enriched palladium in palladium-102 (3.2 % natural abundance) to saturation ($t_{irr} \simeq 85$ d) in a nuclear reactor with a flux of $10^{15} \cdot n\, s^{-1} \cdot cm^{-2}$ will lead to about 6.8 % of ^{103}Pd.

The most widely used accelerator production method based on high-flux 18 MeV proton irradiation of a ^{103}Rh target in cyclotrons [INTERNATIONAL ATOMIC ENERGY AGENCY, 2009, 2012] allows to reach a yield [Otuka and Takács, 2015] equal to 2.40 GBq·C^{-1} (the yield for an energy irradiation of 50 MeV is 3.25 GBq·C^{-1}).

The use of a deuteron beam appears to be attractive for the production of a few radionuclides since the (d,2n) reaction cross-section in the medium to high mass region is generally higher than that of (p,n) reactions [Qaim, 2016]. However, studies on this alternative production methods using deuterons were scarce, and only two studies were reported beginning of this research work [Ditrói et al., 2011, Hermanne et al., 2002].

My work presents and discusses the experimental results with reference to the cross-sections of the ^{103}Rh(d,2n)^{103}Pd reaction and of the co-produced radionuclides in the 5–33 MeV energy range.

6.2 Experimental

The excitation functions were determined using the stacked-foil technique. Stacks of thin foils consisted of alternating high purity aluminium (as energy degrader and monitor foils inserted between the Rh and the Ti targets), rhodium and titanium foils. In particular each stack was composed of the same number of Rh and Al foils, i.e. four or five, depending on the irradiation energy, and (i) by a Ti foil, inserted

as final monitor foil in the stack for the JRC-Ispra irradiations or (ii) one Ti foil after each of the Rh/Al foils in the stack for the GIP-ARRONAX irradiations.

^{103}Rh targets (Goodfellow Cambridge Ltd., Ermine Business Park, Huntingdon PE29 6WR, UK) had a nominal thickness of 12.5 or 25 μm (~15.1–31.7 mg·cm^{-2} with a general relative uncertainty of ± 2 %: these values of target thickness used in the calculation were measured accurately by weighing).

Low-energy irradiations were carried out on five stacks with the cyclotron (Scanditronix MC40, K = 38) of the JRC-Ispra at different incident energies covering the energy range from 16.6 MeV down to 5.2 MeV with a constant current of about 100 nA for a duration of 1 hour.
Each irradiation was carried out in an insulated target holder under vacuum, which was designed as an elongated Faraday cup to determine the integrated charge of the deuteron beam. Inside the Faraday cup a strong magnet was installed to avoid escaping of scattered or backscattered electrons as the loss of such electrons could lead to a virtually larger deuteron charge on the foil stacks. Two coaxial Al collimators (5 mm in diameter) were placed in front of the Faraday cup. Based on the distance between the collimators and the last couple of quadrupoles, a maximum broadening of the beam of a few μm was calculated. The charge was integrated by a current integrator (BIC Brookhaven Instruments Corporation, Austin, TX, USA; model 1000C), calibrated within 2 % of uncertainty by an authorized calibration service (Nemko S.p.A., Biassono, MB, Italy). The incident energy has an uncertainty of ± 0.20 MeV [Birattari et al., 1992].
The reliability of the integrated current has been validated by the values of the cross-sections measured for ^{nat}Ti targets used as monitor foils, compared with the IAEA tabulated monitor reaction ^{nat}Ti(p,x)^{48}V [Tárkányi et al., 2001].

Medium and high-energy irradiations were carried out with an IBA C70 cyclotron of the ARRONAX center, Saint-Herblain (FR). The ARRONAX cyclotron delivers deuteron beam at variable energies with an energy uncertainty of ± 0.25 MeV [Haddad et al., 2008]. The stacks were irradiated with an external deuteron beam. A 75 μm thick kapton foil is used as beam exit windows, separating the beam line vacuum from atmospheric pressure in the vault. The stacks were located 68 mm downstream in air.
During the irradiation, an instrumented beam stop was used to control the beam current stability. However, it was not used as a Faraday cup with precise intensity measurements, since it is not under vacuum and is not equipped with a magnet to

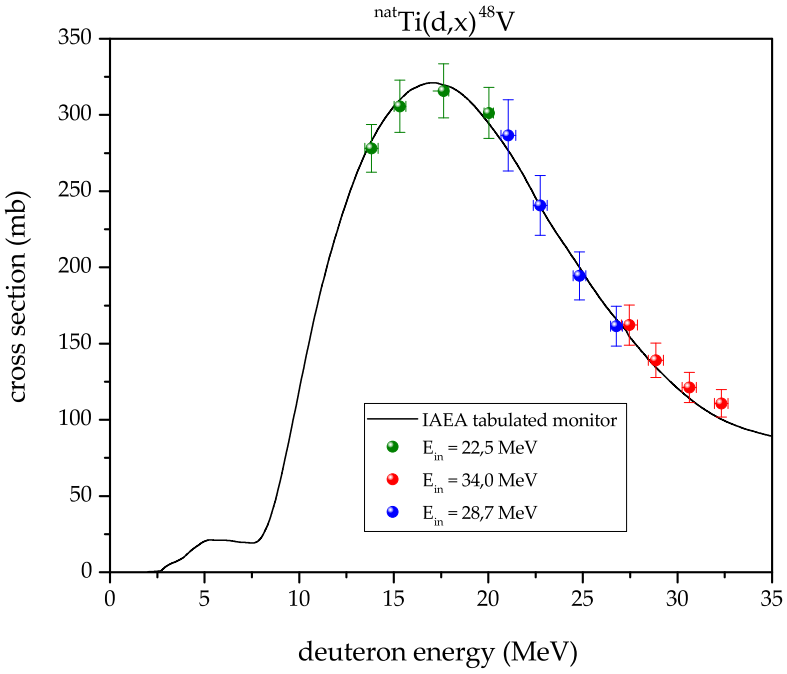

Figure 6.1: Excitation functions for $^{nat}Ti(p,x)^{48}V$ nuclear reactions.

avoid escaping of scattered or backscattered electrons.
In this case, it was mandatory to use titanium and aluminium foils also as monitors to determine the experimental beam intensity value and energy from the $^{nat}Ti(d,x)^{48}V$ and $^{27}Al(d,x)^{24}Na$ IAEA tabulated monitor reactions [Tárkányi et al., 2001] (Figures 6.1 and 6.2).
Four stacks were irradiated with a different incident energy in order to minimize energy straggling and to cover the energy range from 34 MeV down to 14 MeV, with an overlap of more than 2 MeV with the JRC-Ispra irradiations. Irradiations were carried out with a mean beam intensity of about 170 nA for 1 h.

Mean deuteron beam energy and energy degradation in each foil were computed by the Monte Carlo based computer code SRIM 2013 [Ziegler et al., 2010]. The uncertainty of the mean energy in each foil (± 0.2–0.4 MeV) includes the energy uncertainty of the extracted deuteron beam, as well as the uncertainties in the mean mass thicknesses and the beam-energy straggling through the target foils (± 0.1–0.3 MeV).

The activity of each radionuclides detected in each foil was measured at the

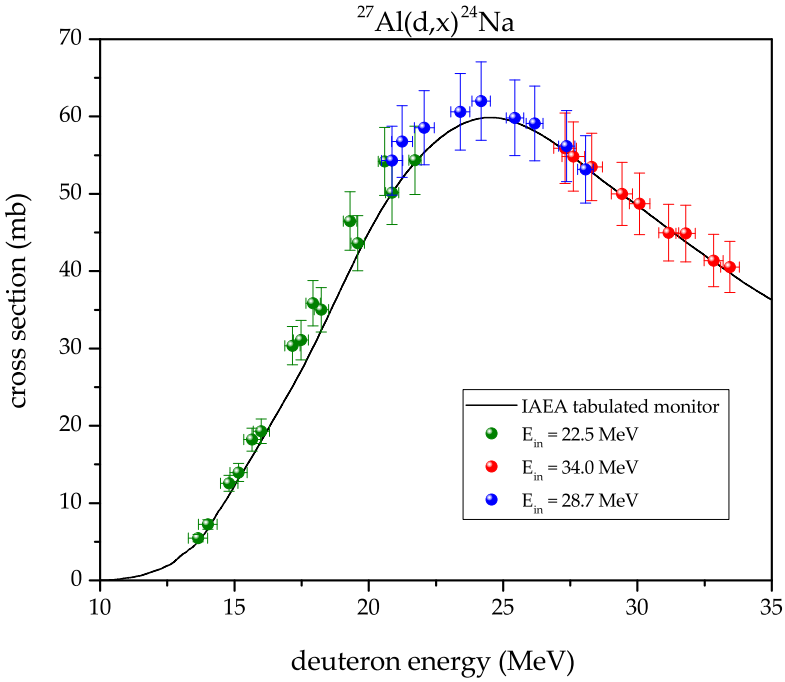

Figure 6.2: Excitation functions for ^{27}Al(d,x)^{24}Na nuclear reactions.

LASA laboratory (INFN and Physics Dept. of University of Milan, Segrate MI), without any chemical processing, by calibrated high purity germanium (HPGe) detectors (EG&G Ortec, 15 % relative efficiency, FWHM = 2.2 keV at 1.33 MeV). The detectors were calibrated with certified ^{152}Eu and ^{133}Ba sources (CercaLEA, France and Amersham, UK). All foils were measured in the same geometrical position as that used for the calibrated sources in the energy and efficiency calibration of the detectors in order to avoid corrections for different geometries. The distance from the detector cap was sufficiently high to reduce dead time and pile up errors to negligible values (< 0.1 %). The first measurements of the samples were generally started within a few hours (for the Ispra irradiations) or within 48 hours (for ARRONAX irradiations) after the end of bombardment (EOB). The measurements continued for about six months in order to follow the decay of the main radionuclides and to let completely decay eventual "parent" radionuclides. (e.g. Figure 6.3).

The overall uncertainty of the determined cross-sections is caused by several error sources in the measurement and evaluation process. Regarding the measurement process, a typical component is related to the statistical error in the peak counts: particular attention is given to reduce this value as low as possible (< 1 %–

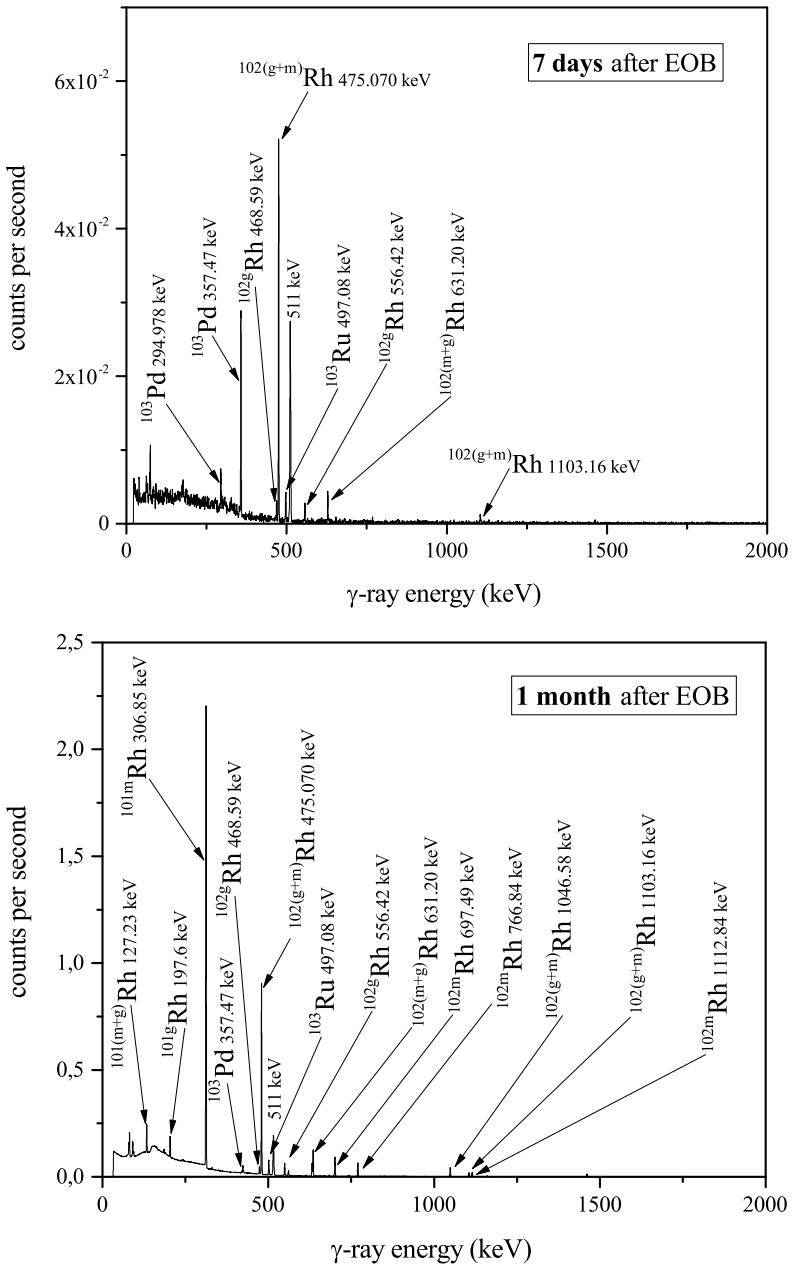

Figure 6.3: Examples of γ-ray spectra for different targets and time.

18 %, depending on the radionuclides and on the energies). Other significant error sources were: the target thickness and uniformity (< 2 %), the integrated charge ($\leq$ 2 %), the calibration sources uncertainty (1.5 % and 2.0 %) and the fitting of the

detector efficiency curves (< 1 %), with an overall relative error of 4–20 %.

The published data about the abundance of the gamma emissions and the half-lives were considered as being exact. Decay characteristics for the radionuclides investigated, as summarized in Table 6.1, were taken from Firestone et al. [1999] and Wang et al. [2012].

6.3 Results

The measured excitation functions are compared in Figures 6.4–6.13 with the literature data. The numerical data are collected in Table 6.2 and Table 6.3.
The cross-sections for Pd isotopes were also theoretically calculated with EMPIRE-3.2.2 [Herman et al., 2007] in order to evaluate the best energy of irradiation to obtain ^{103}Pd with the highest A_S (Section 6.3.7).
In spite of the differences in the irradiation conditions (see Section 6.2) there is a very good overlap between the experimental data obtained from the JRC-Ispra and the ARRONAX facilities.

6.3.1 ^{103}Rh(d,2n)^{103}Pd

^{103}Pd has a half-life of $t_{1/2}$ = 16.991 d and can be produced through the (d,2n) reaction. The activity was determined from the 357.47 keV emission (I_γ = 0.0221 %). The measured experimental cross-sections are shown in Figure 6.4 together with the data of the earlier studies and curves of theoretical calculations with EMPIRE-II Menapace et al. [2008], EMPIRE-3.2.2 and TENDL-2015 [Koning and Rochman, 2012] codes. My cross-sections are in good agreement with the results of Hermanne et al. [2002] (γ data), while they are in the maximum about 15 % higher than those of Ditrói et al. [2011]. The prediction of EMPIRE-3.2.2 and EMPIRE-II are close to the experimental data, while TENDL-2015 underestimates the reaction cross-sections at energies above 10 MeV.

In order to enable quantitative considerations for the production of ^{103}Pd, it is useful to calculate the Thick-Target Yield (TTY); this was done using the polynomial fit result of the experimental thin-target yields presented in Figure 6.5 and integrating it up to a given deuteron energy. Figure 6.6 shows the resulting Thick-Target Yield and, also, experimental Thick-Target Yields presented in literature (Dmitriev et al. [1983, 1982] and Mukhammedov et al. [1984]) and the IAEA recommended one [INTERNATIONAL ATOMIC ENERGY AGENCY, 2012].

It is possible to see that there is a very good agreement between the experimental data sets and the curve related to the present work, while there are discrepancies

Table 6.1: Decay data [Firestone et al., 1999] of Pd, Rh and Ru radionuclides and contributing reactions. The E_{th} evaluation is based on the mass defects of Wang et al. [2012].

Nuclide	$t_{1/2}$	Contributing reactions	E_{th} (MeV)	E_γ (keV)	I_γ (%)
^{104}Pd	stable	^{103}Rh(d,n)^{104}Pd	0		
^{103}Pd	16.991 d	^{103}Rh(d,2n)^{103}Pd	3.62	357.47	0.0221
^{102}Pd	stable	^{103}Rh(d,3n)^{102}Pd	11.39		
^{101}Pd	8.47 h	^{103}Rh(d,4n)^{101}Pd	22.17	296.29	19.2
^{102m}Rh	3.742 a Tuli [2011]*	^{103}Rh(d,p2n)^{102m}Rh	11.91	697.49	43.9
		^{103}Rh(d,dn)^{102m}Rh	7.91		
		^{103}Rh(d,t)^{102m}Rh	1.53		
^{102g}Rh	207 d	^{103}Rh(d,p2n)^{102g}Rh	11.77	468.59	2.813
		^{103}Rh(d,dn)^{102g}Rh	7.77		
		^{103}Rh(d,t)^{102g}Rh	1.39		
^{101m}Rh	4.34 d	^{103}Rh(d,p3n)^{101m}Rh	19.52	306.85	87
		^{103}Rh(d,d2n)^{101m}Rh	17.25		
		^{103}Rh(d,tn)^{101m}Rh	10.87		
^{101g}Rh	3.3 a	^{103}Rh(d,p3n)^{101g}Rh	19.36	197.6	70.88
		^{103}Rh(d,d2n)^{101g}Rh	17.09		
		^{103}Rh(d,tn)^{101g}Rh	10.71		
^{100g}Rh	20.8 h	^{103}Rh(d,p4n)^{100g}Rh	29.44	539.51	80.6
		^{103}Rh(d,d3n)^{100g}Rh	27.18		
		^{103}Rh(d,t2n)^{100g}Rh	20.80		
^{103}Ru	39.26 d	^{103}Rh(d,2p)^{103}Ru	2.25	497.08	90.9

*The value reported in Firestone et al. [1999] is ~2.9 a: in this case we prefer to use a more precise value from another database

Table 6.2: Experimental cross-sections (1SD) of the ^{103}Rh(d,xn)^{103,101}Pd, ^{103}Rh(d,2p)^{103}Ru and ^{103}Rh(d,p5n)^{100g}Rh reactions

Energy (MeV)	^{101}Pd (mb)	^{103}Pd (mb)	^{103}Ru (mb)	^{100g}Rh (mb)
5.23 ± 0.25		22.5 ± 2.8		
6.53 ± 0.26		131.2 ± 6.5	0.011 ± 0.002	
7.37 ± 0.19		324.6 ± 15.2	0.020 ± 0.001	
7.75 ± 0.27		316.6 ± 18.4	0.027 ± 0.004	
8.41 ± 0.21		516.2 ± 24.8	0.037 ± 0.003	
8.93 ± 0.28		604.2 ± 29.1	0.051 ± 0.005	
9.46 ± 0.23		681.0 ± 34.2	0.057 ± 0.005	
10.00 ± 0.30		800.0 ± 37.3	0.064 ± 0.005	
10.50 ± 0.24		845.2 ± 40.8	0.078 ± 0.006	
11.13 ± 0.33			0.087 ± 0.005	
11.51 ± 0.26			0.090 ± 0.011	
12.23 ± 0.34			0.102 ± 0.006	
12.53 ± 0.28		1166.9 ± 53.8	0.106 ± 0.006	
13.22 ± 0.36		1127.5 ± 52.4	0.108 ± 0.006	
13.56 ± 0.30		1141.4 ± 52.8	0.109 ± 0.007	
13.91 ± 0.34		1253.4 ± 60.1	0.120 ± 0.006	
14.32 ± 0.34		1142.7 ± 103.5	0.125 ± 0.014	
14.53 ± 0.30		1207.2 ± 98.4	0.146 ± 0.012	
14.95 ± 0.38		1261.1 ± 58.3	0.149 ± 0.008	
15.53 ± 0.38		1107.8 ± 51.4	0.140 ± 0.007	
15.65 ± 0.28		1090.3 ± 88.9	0.157 ± 0.013	
16.10 ± 0.35		1127.1 ± 52.8	0.196 ± 0.010	
16.50 ± 0.29		1043.7 ± 103.5	0.180 ± 0.015	
16.63 ± 0.36		1040.3 ± 49.3	0.175 ± 0.009	
18.70 ± 0.26		743.4 ± 62.6	0.326 ± 0.028	
21.29 ± 0.25		392.8 ± 64.9	0.628 ± 0.052	
21.65 ± 0.39		374.4 ± 34.9	0.625 ± 0.052	
23.79 ± 0.35		239.9 ± 27.5	1.00 ± 0.08	
25.81 ± 0.32	12.31 ± 1.12	208.0 ± 24.5	1.37 ± 0.11	
27.71 ± 0.29	56.58 ± 4.71	188.8 ± 23.4	1.68 ± 0.14	
27.95 ± 0.41	46.92 ± 3.93	168.9 ± 23.3	1.59 ± 0.13	
29.75 ± 0.39	121.6 ± 10.01	142.98 ± 23.8	1.92 ± 0.16	0.23 ± 0.03
31.48 ± 0.37	194.85 ± 15.96	140.5 ± 30.9	2.17 ± 0.18	0.68 ± 0.07
33.14 ± 0.35	266.15 ± 21.73	96.3 ± 20.0	2.39 ± 0.19	1.36 ± 0.12

Table 6.3: Experimental cross-sections (1SD) of the ^{103}Rh(d,pxn)$^{\bullet}$Rh

Energy (MeV)	^{102m}Rh (mb)	^{102g}Rh (mb)	^{101m}Rh (mb)	^{101g}Rh (mb)
7.37 ± 0.19		1.40 ± 0.32		
8.93 ± 0.28		1.91 ± 0.18		
9.46 ± 0.23		2.04 ± 0.18		
10.00 ± 0.30	0.23 ± 0.08	3.35 ± 0.55		
10.50 ± 0.24	0.16 ± 0.06	3.77 ± 0.22		
11.13 ± 0.33	0.66 ± 0.08	7.83 ± 0.47		
12.23 ± 0.34	0.81 ± 0.20	9.69 ± 0.60		
12.53 ± 0.28	0.41 ± 0.06	10.37 ± 0.72		
13.22 ± 0.36	0.51 ± 0.06	11.09 ± 0.53		
13.56 ± 0.30	0.74 ± 0.18	11.01 ± 1.18		
13.91 ± 0.34	0.67 ± 0.08	13.51 ± 0.69		
14.32 ± 0.34	1.56 ± 0.27	14.12 ± 1.39		
14.95 ± 0.38	1.46 ± 0.20	15.40 ± 0.88		
15.53 ± 0.38	1.39 ± 0.11	15.21 ± 0.74		
16.10 ± 0.35	2.35 ± 0.29	16.82 ± 1.02		
16.50 ± 0.29	2.21 ± 0.26	17.61 ± 1.53		
16.63 ± 0.36	2.19 ± 0.16	16.89 ± 0.88		
18.70 ± 0.26	8.22 ± 0.83	23.65 ± 2.08		
21.29 ± 0.25	33.56 ± 2.75	32.69 ± 4.78		
21.65 ± 0.39	35.74 ± 2.96	39.06 ± 3.33	1.07 ± 0.09	0.50 ± 0.13
23.79 ± 0.35	72.97 ± 5.96	63.44 ± 5.34	0.95 ± 0.08	1.08 ± 0.23
25.81 ± 0.32	113.35 ± 9.21	85.14 ± 7.11	17.72 ± 1.59	1.58 ± 0.16
27.71 ± 0.29	147.77 ± 12.02	104.99 ± 8.61	76.90 ± 6.63	1.86 ± 0.17
27.95 ± 0.41	138.43 ± 11.25	97.40 ± 7.97	64.68 ± 5.59	1.97 ± 0.18
29.75 ± 0.39	167.15 ± 13.58	112.82 ± 9.22	114.10 ± 10.10	3.85 ± 0.34
31.48 ± 0.37	185.60 ± 15.10	119.84 ± 9.83	267.63 ± 23.06	7.35 ± 0.66
33.14 ± 0.35	190.89 ± 15.51	121.76 ± 9.93	371.41 ± 31.97	14.30 ± 1.27

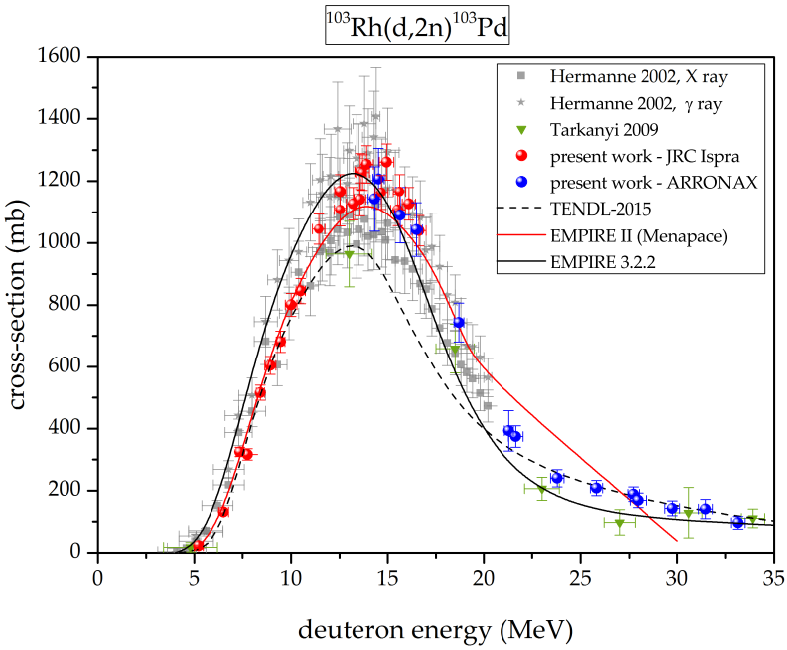

Figure 6.4: Excitation functions for ^{103}Rh(d,2n)^{103}Pd nuclear reactions.

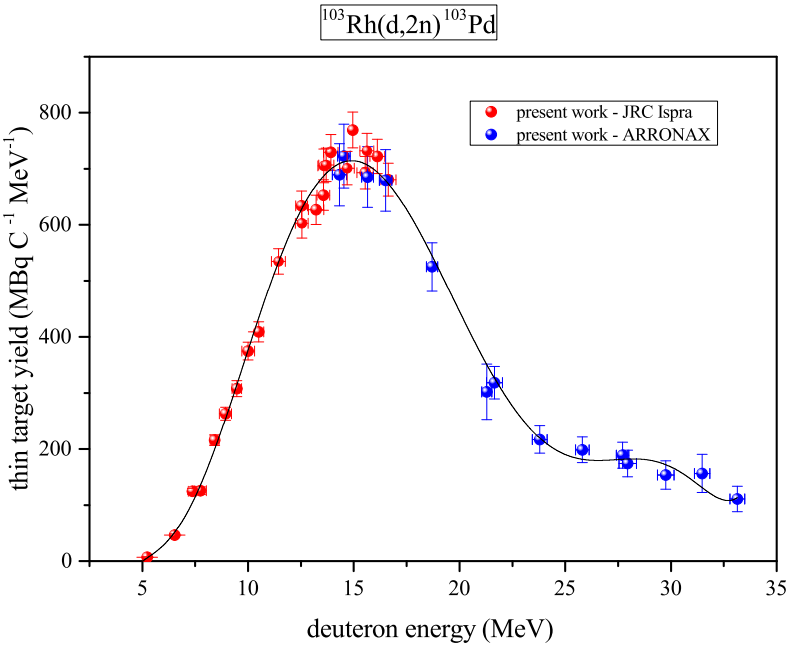

Figure 6.5: ^{103}Rh(d,2n)^{103}Pd experimental and fitted thin-target yield.

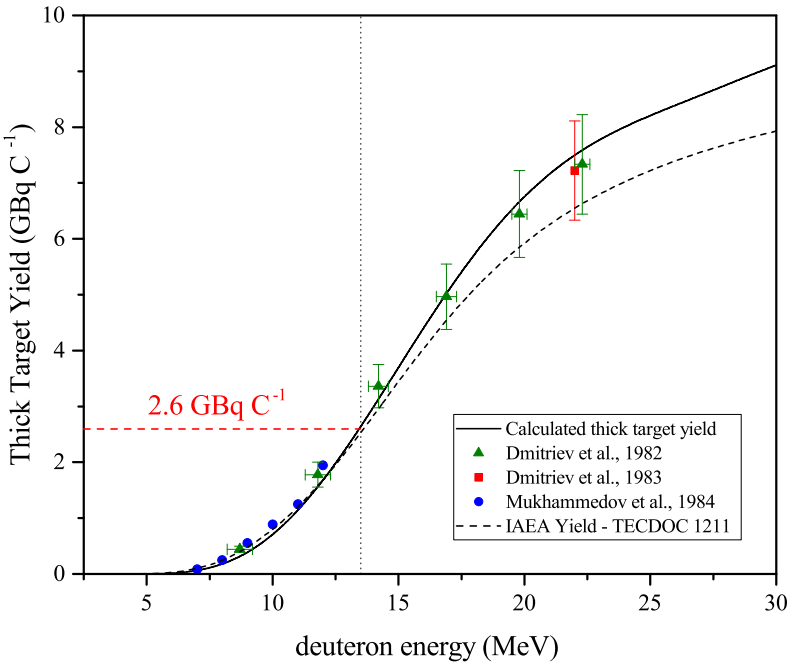

Figure 6.6: Calculated Thick-Target Yields for the production of ^{103}Pd as a function of deuteron irradiation energy.

with the IAEA curve.

6.3.2 ^{103}Rh(d,4n)^{101}Pd

^{101}Pd has a half-life of $t_{1/2}$ = 8.47 h and can be produced through the (d,4n) reaction. The activity was assessed through the 296.29 keV gamma line (I_γ = 19.2 %).

My cross-sections are in good agreement with the results of Ditrói et al. [2011] (Figure 6.7). The prediction of EMPIRE-3.2.2 is in quite good agreement with the experimental data.

6.3.3 ^{103}Rh(d,x)^{102m,g}Rh

^{102}Rh can be produced through the (d,p2n), (d,dn) and (d,t) reactions.

^{102m}Rh has a half-life of $t_{1/2}$ = 3.742 a and the activity was assessed through the 697.49 keV gamma line (I_γ = 43.90 %).

My cross-sections are, in general, in good agreement with the results of Ditrói et al. [2011] and Hermanne et al. [2002] (Figure 6.8).

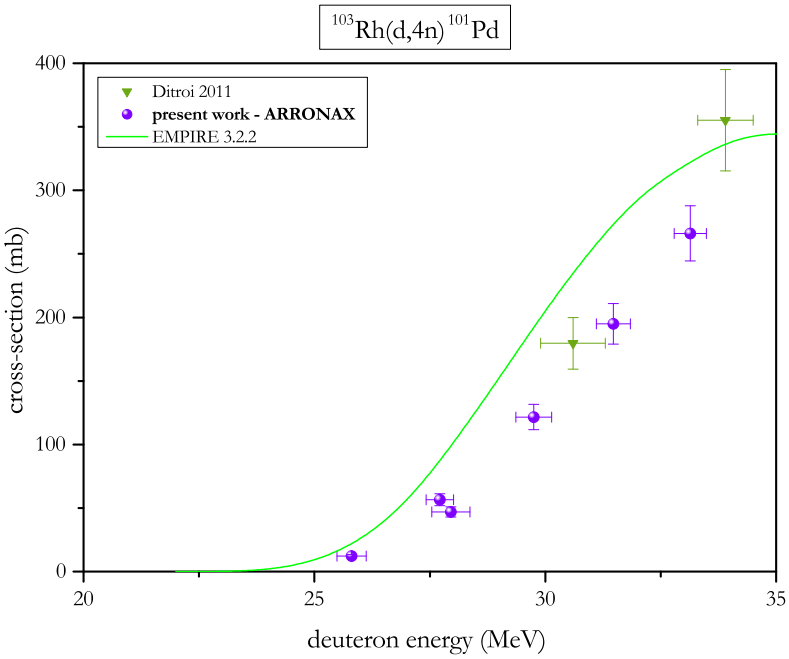

Figure 6.7: Excitation functions for ^{103}Rh(d,4n)^{101}Pd nuclear reaction.

^{102g}Rh has a half-life of $t_{1/2}$ = 207 d and its activity was determined from the 468.59 keV gamma line (I_γ = 2.813 %). Under my experimental conditions ^{102g}Rh is mainly formed directly because the contribution of the decay of the metastable level is negligible (only 0.233 % IT and low ratio between the half-lives).
My cross-sections are in good agreement with the results of Hermanne et al. [2002] (Figure 6.9). The discrepancy with Ditrói et al. [2011] can be explained taking into account that Ditroi et al. used the 628.05 keV gamma line to determine the activity but also ^{102m}Rh contributes to this emission (I_γ = 8.5 %) which may result in an overestimation of the ^{102g}Rh activity. It is possible to appreciate this contribution at energies greater than 18 MeV: it is shown in Figure 6.8 that the ^{103}Rh(d,x)^{102m}Rh cross-section starts to increase rapidly from this energy value.

6.3.4 ^{103}Rh(d,x)^{101m,g}Rh

^{101}Rh can be produced through the (d,p3n), (d,d2n) and (d,tn) reactions.

^{101m}Rh has a half-life of $t_{1/2}$ = 4.34 d and the activity was determined from the 306.85 keV emission (I_γ = 87 %); ^{101m}Rh is also formed by the decay of the much

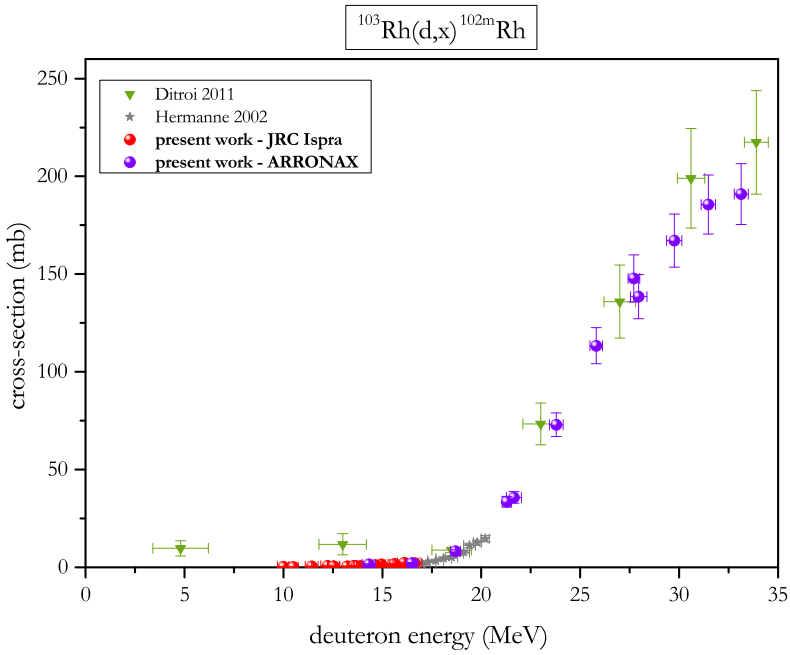

Figure 6.8: Excitation functions for ^{103}Rh(d,x)^{102m}Rh nuclear reactions.

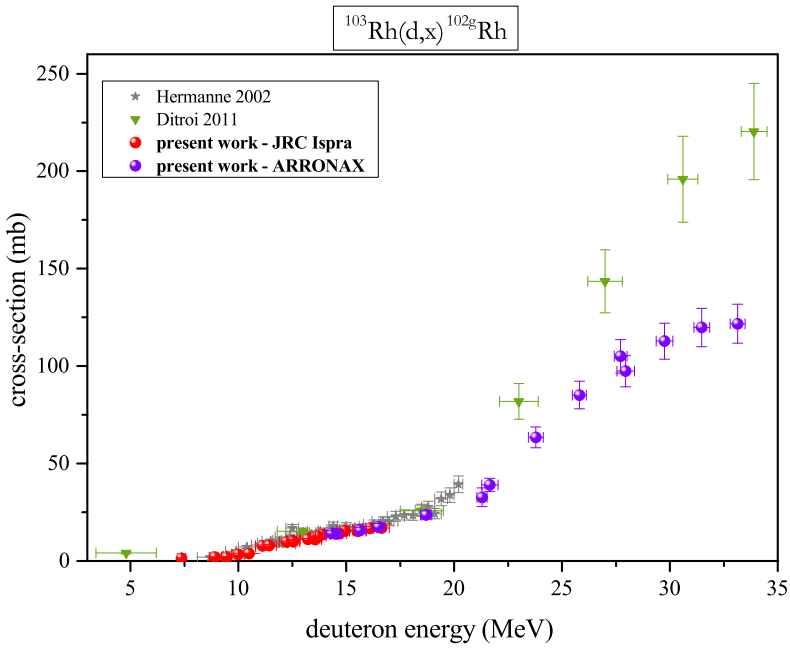

Figure 6.9: Excitation functions for ^{103}Rh(d,x)^{102g}Rh nuclear reactions.

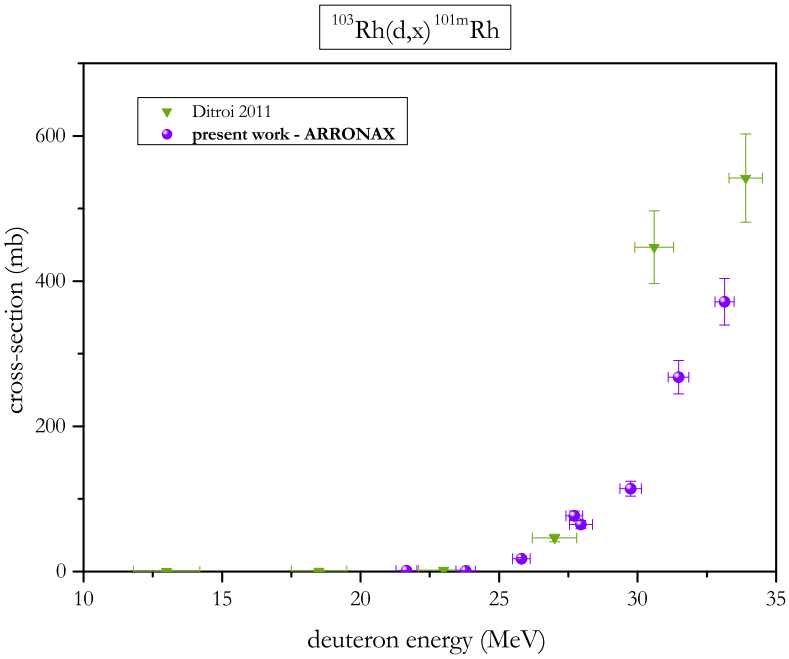

Figure 6.10: Excitation functions for ^{103}Rh(d,x)^{101m,cum}Rh nuclear reactions.

shorter lived ^{101}Pd (8.47 h, 99.731 %). Therefore, the measurements for this radionuclide were done once that ^{101}Pd was completely decayed in order to subtract this contribution. My cross-sections are quite smaller than the results of Ditrói et al. [2011] (Figure 6.10): this is because Ditroi et al. measured the cumulative production of ^{101m}Rh.

^{101g}Rh has a half-life of $t_{1/2} = 3.3$ a and the activity was determined quantifying the 197.6 keV emission ($I_\gamma = 70.88\,\%$). ^{101g}Rh is also formed by the de-excitation of the shorter lived metastable level ^{101m}Rh and, also in this case, the measurements for this radionuclide were done once that its metastable level was completely de-excited. My cross-sections are in quite good agreement with the few data points of Ditrói et al. [2011] (Figure 6.11).

6.3.5 ^{103}Rh(d,x)^{100g,cum}Rh

^{100}Rh can be produced through the (d,p4n), (d,d3n) and (d,t2n) reactions.

^{100g}Rh has a half-life of $t_{1/2} = 20.8$ h and the activity was determined analysing the 539.51 keV gamma emission ($I_\gamma = 80.6\,\%$)

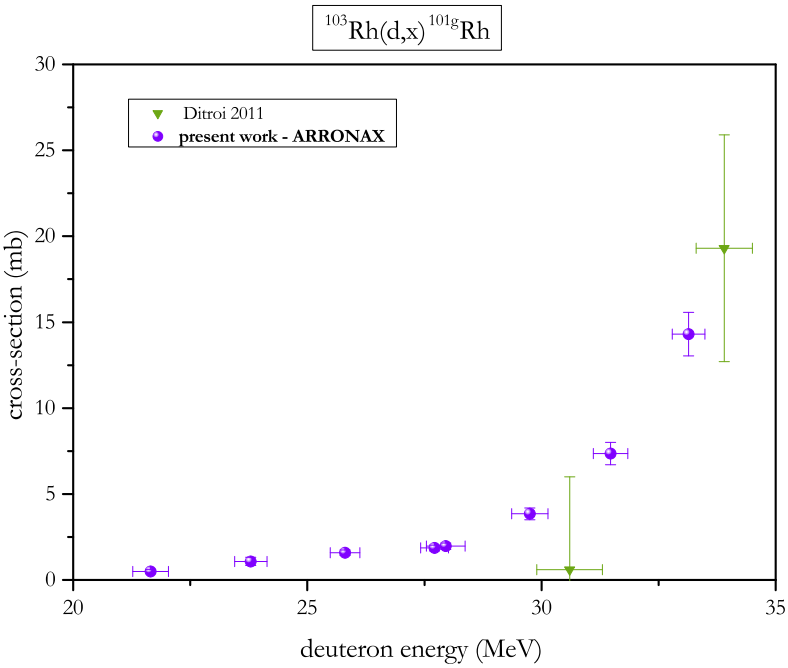

Figure 6.11: Excitation functions for ^{103}Rh(d,x)^{101g}Rh nuclear reactions.

The determined cross-section includes a contribution from the not measured short lived and totally decayed ^{100m}Rh isomer ($t_{1/2}$ = 4.7 m).
The derived cross-section data are in good agreement with the results of Ditrói et al. [2011] (Figure 6.12).

6.3.6 ^{103}Rh(d,2p)^{103}Ru

^{103}Ru has a half-life of $t_{1/2}$ = 39.26 d and can be produced through the (d,2p) reaction. The activity was determined from the 497.08 keV gamma emission (I_γ = 90.9 %).
My cross-sections are in good agreement with the results of Ditrói et al. [2011] (Figure 6.13).

6.3.7 Specific Activity for ^{103}Pd production

The good agreement between the experimental data of the produced Pd radioisotopes and the EMPIRE-3.2.2 calculations was shown in Figures 6.4 and 6.7.

Using EMPIRE-3.2.2, it is possible to calculate also the cross-sections for the

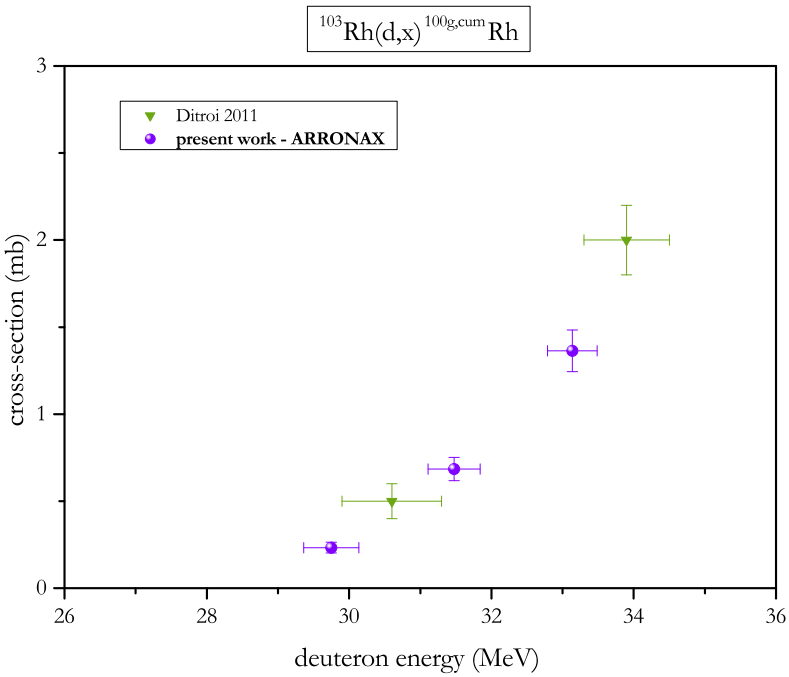

Figure 6.12: Excitation functions for ^{103}Rh(d,x)^{100g,cum}Rh nuclear reactions.

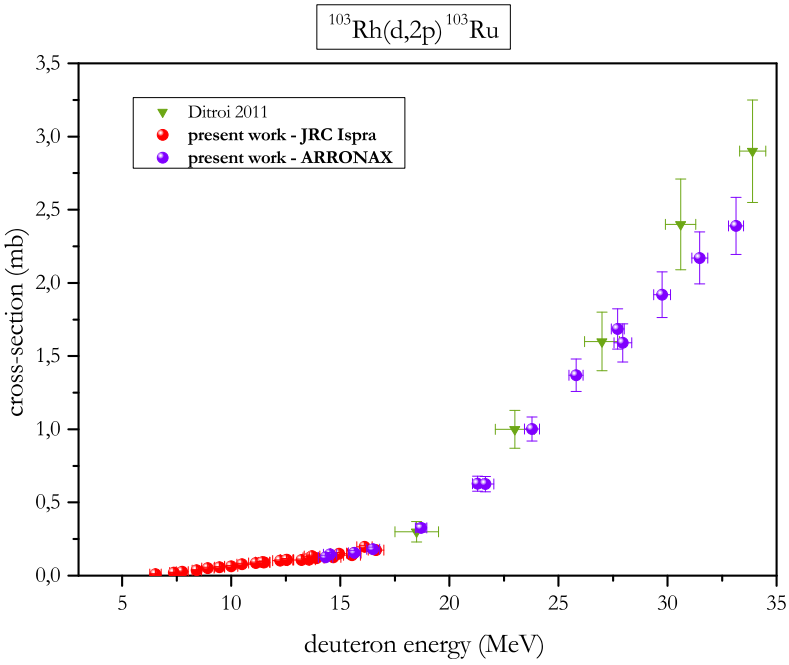

Figure 6.13: Excitation functions for ^{103}Rh(d,2p)^{103}Ru nuclear reactions.

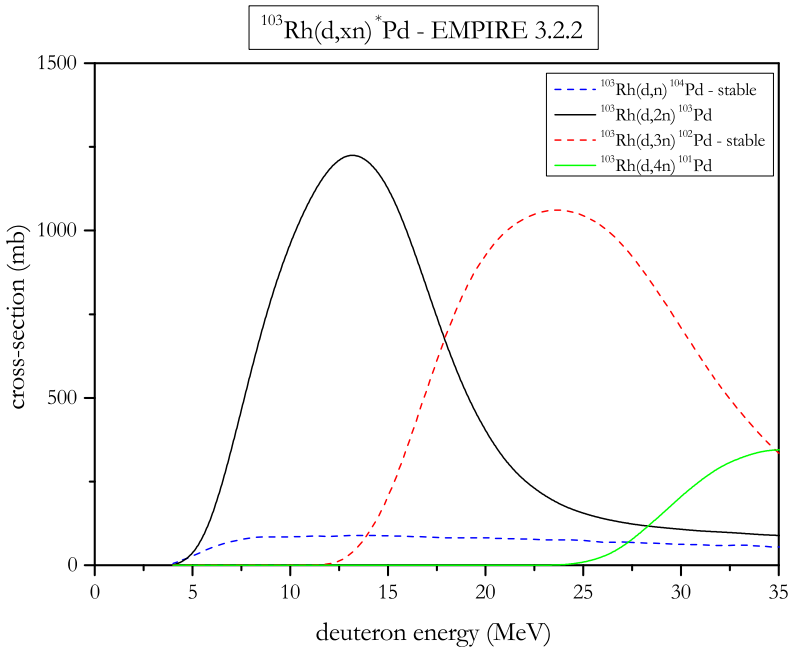

Figure 6.14: Excitation functions for $^{103}Rh(d,x)^{\bullet}Pd$ nuclear reactions calculated with the model EMPIRE-3.2.2

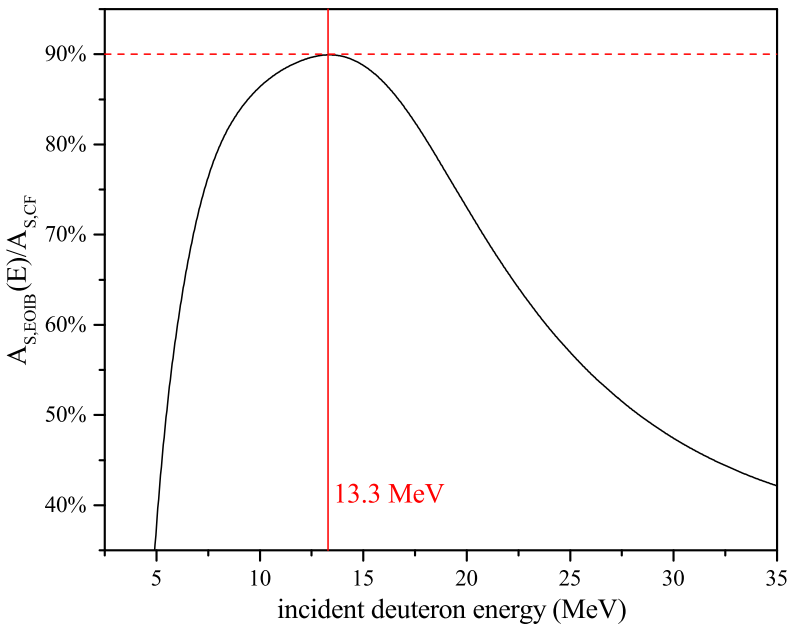

Figure 6.15: Ratio between the A_S at the End Of an Instantaneous Bombardment and the A_S(CF) calculated from the results presented in Figure 6.14

formation of the stable isotopes of palladium (Figure 6.14).

Based on the EMPIRE simulation and in case of a target at total energy absorption, in order to obtain the highest A_S of ^{103}Pd (90 %), the best incident energy is 13.3 MeV (Figure 6.15). The curve presented in Figure 6.15 is exact for an Instantaneous Bombardment but, for an incident deuteron energy smaller than 22 MeV (the energy threshold for the production of ^{101}Pd), it is a very good description at the End of Bombardment for $t_{irr} \ll (\lambda_{^{103}Pd})^{-1}$ (i.e. $t_{irr} \ll 588\,h$).

6.4 Conclusions

In the present study I experimentally determined the excitation functions for the radionuclides produced by cyclotron irradiation of Rh targets with deuteron beams in the energy range from 5 to 33 MeV. In particular, I have measured the cross-section for ^{103}Pd production by ^{103}Rh(d,2n)^{103}Pd nuclear reactions.

In the energy range presented here, the only radio-isotopic impurities is the ^{101}Pd radionuclide that has an energy threshold of 22 MeV and an half-life of 8.47 h.

In order to have high A_S, it is mandatory to take into account also the production of the stable isotopes of palladium (Figure 6.15); the presented excitation curves allow the calculation and the optimization of the ^{103}Pd batch yields: the best incident energy for the production is 13.3 MeV and it is possible to produce 2.6 GBq C^{-1} of ^{103}Pd at the EOIB (Figure 6.6).

So, the use of deuteron as particle beam leads to high TTYs, high radionuclidic purity, high specific activity and at the same time requires a less amount of rhodium to be involved in the radiochemical separation: more ^{103}Pd is formed and less ^{103}Rh is needed for the target, due to larger $-dE/dx$ in the case of deuteron over proton.

The criticality of this system is tied to the practical availability of accelerators with deuteron beams with possibly high energy and a reasonable intensity. But due to the half-life of ^{103}Pd radionuclide, nothing prevents to produce it in Centres with cyclotrons with deuteron beam and energies depending on the advisable A_S and on the eligible ^{103}Pd activity.

Summary of the conclusions

The activities described in this work concern the study of accelerator-based routes aimed to the production of nuclides relevant to nuclear medicine as ^{99m}Tc, its precursor ^{99}Mo, ^{103}Pd and ^{89}Zr.
These radionuclides applied at different radiopharmaceuticals are or can be used as imaging and therapeutic agents in nuclear medicine and in the relatively new branch called nano-medicine.
In fact, the interest in radiolabelled nanoparticles is increasing:compared to conventional contrast agents, nanoparticles promise to improve in vivo detection and enable more efficient targeting due to increased circulation times, evasion of clearance pathways, and multimeric binding capacity.

My work was finalized to the optimization of the production of the aforementioned radionuclides. In particular:

- ^{99m}Tc (Chapter 4), that is the most used radiotracer in nuclear medicine. An experimental verification of the reaction cross sections of the nuclear reactions ^{100}Mo(p,x)^{99}Mo and ^{100}Mo(p,2n)^{99m}Tc is presented and the solution of the exact differential equation starting from the EOIB is given.
  It is my opinion that the best energy range range for the direct production of ^{99m}Tc via cyclotron route is 12–17 MeV. In fact, the cross section reaches its maximum value in this energy range. Furthermore, for energies higher than about 17 MeV there is a sharp increase of the side production of the long-lived radioisotopic impurities due to the production of ^{98}Tc (^{100}Mo(p,3n)^{98}Tc, E_{th}=16.85 MeV);

- ^{89}Zr (Chapter 5) is one of the most promising radionuclides for labelling

monoclonal antibodies, bio-distribution studies and immuno-positron emission tomography (PET) imaging. I presented measurement of the excitation functions of the deuteron-induced reactions on ^{89}Y up to 18 MeV. So, significant amounts of ^{89}Zr can be produced at low energy accelerators using yttrium as target and the possibility to involve radionuclidic impurities is very low in the energy range considered in this study;

- ^{103}Pd (Chapter 6), because of its suitable half life and decay characteristics, has been of great interest in permanent brachytherapy. With the rapid development of nanoscience and nanotechnology, it becomes appealing to make injectable nano-scale brachytherapy seeds: a new strategy under development to replace millimetre-size implants, consist in injecting radioactive NPs in the affected tissues. In order to have high A_S, it is mandatory to take into account also the production of the stable isotopes of palladium; the presented excitation curves allow the calculation and the optimization of the ^{103}Pd batch yields: the best incident energy for the production is 13.3 MeV and it is possible to produce 2.6 GBq C^{-1} of ^{103}Pd at the EOIB.

References

Abou, D., Thorek, D., Ramos, N., Pinkse, M., Wolterbeek, H., Carlin, S., Beattie, B., and Lewis, J. (2013). ^{89}Zr-labeled paramagnetic octreotide-liposomes for PET-MR imaging of cancer. *Pharmaceutical Research*, 30(3):878–888.

Alharbi, A. A., Azzam, A., McCleskey, M., Roeder, B., Spiridon, A.and Simmons, E., Goldberg, V., Banu, A., Trache, L., and Tribble, R. E. (2011). Medical radioisotopes production: A comprehensive cross-section study for the production of Mo and Tc radioisotopes via proton induced nuclear reactions on ^{nat}Mo. In Singh, N., editor, *Radioisotopes - Applications in Bio-Medical Science*, pages 3–26. InTech. ISBN: 978-953-307-748-2.

Amaldi, U. (1971). *Fisica delle Radiazioni*, chapter 8, pages 315–425. Boringhieri.

Bansal, A., Pandey, M., Demirhan, Y., Nesbitt, J., Crespo-Diaz, R., Terzic, A., Behfar, A., and DeGrado, T. (2015). Novel ^{89}Zr cell labeling approach for PET-based cell trafficking studies. *EJNMMI Research*, 5(1).

Baron, N. and Cohen, B. L. (1963). Activation cross-section survey of deuteron-induced reactions. *Physical Review*, 129:2636–2642.

Becker, J. S. (2003). Mass spectrometry of long-lived radionuclides. *Spectrochimica Acta Part B: Atomic Spectroscopy*, 58(10):1757–1784.

Bethe, H. (1932). Bremsformel für elektronen relativistischer geschwindigkeit. *Zeitschrift für Physik*, 76:293–299.

Birattari, C., Castiglioni, M., and Silari, M. (1992). Absolute calibration of accelerator beam energies by the crossover technique. *Nuclear Instruments and Methods in Physics Research Section A: Accelerators, Spectrometers, Detectors and Associated Equipment*, 320(3):413–431.

Bissem, H. H., Georgi, R., Scobel, W., Ernst, J., Kaba, M., Rao, J. R., and Strohe, H. (1980). Entrance and exit channel phenomena in *d*- and ^{3}He-induced preequilibrium decay. *Phys. Rev. C*, 22:1468–1484.

Bohr, N. (1913). On the theory of the decrease of velocity of moving electrified particles on passing through matter. *Philosophical Magazine Series 6*, 25(145):10–31.

Bohr, N. (1936). Neutron capture and nuclear constitution. *Nature*, (137):344–348.

Bonardi, L. M. and de Goeij, M. J. J. (2005). How do we ascertain specific activities in no-carrier-added radionuclide preparations? *Journal of Radioanalytical and Nuclear Chemistry*, 263(1):87–92.

Bonardi, M. (1987). *Proceedings of the IAEA Consultants' Meeting on Data Requirements for Medical Radioisotope Production, Tokyo, Japan, 20-24 April 1987*, volume INDC(NDS)-195/GZ, chapter The contribution to nuclear data for biomedical radioisotope production from the Milan Cyclotron Laboratory, pages 98–112. IAEA.

Bonardi, M., Birattari, C., Groppi, F., and Sabbioni, E. (2002). Thin-target excitation functions, cross-sections and optimised thick-target yields for $^{\mathrm{nat}}$Mo(p,xn)$^{94g,95m,95g,96(m+g)}$Tc nuclear reactions induced by protons from threshold up to 44 MeV. No Carrier Added radiochemical separation and quality control. *Applied Radiation and Isotopes*, 57(5):617–635. A Special Issue dedicated to the memory of Richard M. Lambrecht 1 943 - 2001.

Bonardi, M. L., Birattari, C., Groppi, F., Gini, L., and Mainardi, H. S. C. (2004). Cyclotron production and quality control of "high specific activity' radionuclides in "no-carrier-added" form for radioanalytical applications in the life sciences. *Journal of Radioanalytical and Nuclear Chemistry*, 259(3):415–419.

Brasse, D. and Nonat, A. (2015). Radiometals: Towards a new success story in nuclear imaging? *Dalton Transactions*, 44(11):4845–4858.

Browne, E. and Tuli, J. (2011). Nuclear Data Sheets for A = 99. *Nuclear Data Sheets*, 112(2):275–446.

Challan, M. B., Comsan, M. N. H., and Abou-Zeid, M. A. (2007). Thin target yields and EMPIRE-II predictions on the accelerator production of technetium-99m. *J. Nucl. Radiat. Phys.*, 2(1):1–12.

Chen, D., Zhang, Q., and Chang, Y. (1985). Absolute Intensity Determination of the 140.5 keV gamma ray of ^{99}Mo, ^{99m}Tc. *Nuclear Science, IEEE Transactions on*, 32(1):71–73.

Choppin, G., Liljenzin, J., and Rydberg, J. (2002). *Radiochemistry and Nuclear Chemistry*, chapter 12, 14 and 15. Butterworth-Heinemann.

Council of the European Union (2010). 13399/1/10 REV 1, Draft Council Conclusions "Towards the Secure Supply of Radioisotopes for Medical Use in the European Union".

de Goeij, J. J. M. and Bonardi, M. L. (2005a). How do we define the concepts specific activity, radioactive concentration, carrier, carrier-free and no-carrier-added? *Journal of Radioanalytical and Nuclear Chemistry*, 263(1):13–18.

de Goeij, M. J. J. and Bonardi, L. M. (2005b). How do we define the concepts specific activity, radioactive concentration, carrier, carrier-free and no-carrier-added? *Journal of Radioanalytical and Nuclear Chemistry*, 263(1):13–18.

Dearling, J. and Pedley, R. (2007). Technological advances in radioimmunotherapy. *Clinical Oncology*, 19(6):457–469. Importance of Radiobiology to Cancer Therapy: Current Practice and Future PerspectivesRadiobiology & Cancer Therapy.

Debertin, K. and Helmer, R. (1988). *Gamma- and X-Ray Spectrometry with Semiconductor Detectors*. North-Holland.

Degering, D., Unterricker, S., and Stolz, W. (1988). Excitation function of the ^{89}Y(d,2n)^{89}Zr reaction. *Journal of Radioanalytical and Nuclear Chemistry*, 127(1):7–11.

Deri, M., Zeglis, B., Francesconi, L., and Lewis, J. (2013). PET imaging with ^{89}Zr: From radiochemistry to the clinic. *Nuclear Medicine and Biology*, 40(1):3–14.

Ditrói, F., Tárkányi, F., Takács, S., A., H., H., Y., M., B., A., M., and A.V., I. (2011). Study of activation cross-sections of deuteron induced reactions on rhodium up to 40 MeV. *Nuclear Instruments and Methods in Physics Research Section B: Beam Interactions with Materials and Atoms*, 269(18):1963–1972.

Dmitriev, P. P., Krasnov, N. N., and Molin, G. A. (1983). Yields of radioactive nuclides formed by bombardment of a thick target with 22-MeV deuterons. Technical Report INDC(CCP)-210/L.

Dmitriev, P. P., Panarin, M. V., and Molin, G. A. (1982). Production of ^{103}Pd by the ^{103}Rh(p, n) and ^{103}Rh(d, 2n) reactions. *At.Energ.*, 53:198.

Ehmann, W. and Vance, D. (1991). *Radiochemistry and Nuclear Methods of Analysis*, chapter 6, pages 85–103. John Wiley & Sons.

Firestone, R. B., Baglin, C. M., and Chu, S. Y. F. (1999). *Table of Isotopes: 1999 Update with CD-ROM, 1999 Update, 8th Edition.* Wiley-Interscience.

Friedlander, G., Kennedy, J., Macias, E., and Miller, J. (1981). *Nuclear and Radiochemistry*, chapter 4, pages 110–122. John Wiley & Sons.

Gagnon, K., Bénard, F., Kovacs, M., Ruth, T. J., Schaffer, P., Wilson, J. S., and McQuarrie, S. A. (2011). Cyclotron production of ^{99m}Tc: Experimental measurement of the ^{100}Mo(p,x) ^{99}Mo, ^{99m}Tc and ^{99g}Tc excitation functions from 8 to 180 Mev. *Nuclear Medicine and Biology*, 38(6):907–916.

Gagnon, K., Wilson, J. S., and McQuarrie, S. A. (2012). Experimental cross section measurements for the ^{100}Mo(p,x)^{101}Tc, ^{96}Nb, ^{97}Nb reactions in the energy range of 10 to 18 Mev. *Nuclear Medicine and Biology*, 39(7):923–925.

Gilmore, G. (2008). *Practical Gamma-ray Spectroscopy; 2nd ed.* Wiley, Chichester.

Haddad, F., Ferrer, L., Guertin, A., Carlier, T., Michel, N., Barbet, J., and Chatal, J.-F. (2008). ARRONAX, a high-energy and high-intensity cyclotron for nuclear medicine. *European Journal of Nuclear Medicine and Molecular Imaging*, 35(7):1377–1387.

Herman, M., Capote, R., Carlson, B., Obložinský, P., Sin, M., Trkov, A., Wienke, H., and Zerkin, V. (2007). EMPIRE: Nuclear reaction model code system for data evaluation. *Nucl. Data Sheets*, 108:2655.

Hermanne, A., Sonck, M., Takács, S., Tárkányi, F., and Shubin, Y. (2002). Study on alternative production of ^{103}Pd and characterisation of contaminants in the deuteron irradiation of ^{103}Rh up to 21 MeV. *Nuclear Instruments and Methods in Physics Research Section B: Beam Interactions with Materials and Atoms*, 187(1):3–14.

Holloway, M. and Livingston, M. S. (1938). Range and specific ionization of alpha-particles. *Physical Review*, 54:18–37.

ICRP (2008). Annex A. radionuclides of the ICRP-07 collection. *Annals of the ICRP*, 38(3):35–96.

ICRU (1994). *Particle Counting in Radioactivity Measurements (Report 52).*

INTERNATIONAL ATOMIC ENERGY AGENCY (2006). *Production Techniques and Quality Control of Sealed Radioactive Sources of Palladium-103, Iodine-125, Iridium-192 and Ytterbium-169.* INTERNATIONAL ATOMIC ENERGY AGENCY, Vienna. IAEA-TECDOC-1512.

INTERNATIONAL ATOMIC ENERGY AGENCY (2009). *Cyclotron Produced Radionuclides: Physical Characteristics and Production Methods.* Number 468 in Technical Reports Series. INTERNATIONAL ATOMIC ENERGY AGENCY, Vienna.

INTERNATIONAL ATOMIC ENERGY AGENCY (2012). *Nuclear Data for the Production of Therapeutic Radionuclides.* Number 473 in Technical Reports Series. INTERNATIONAL ATOMIC ENERGY AGENCY, Vienna.

Jones, B. L., Krishnan, S., and Cho, S. H. (2010). Estimation of microscopic dose enhancement factor around gold nanoparticles by Monte Carlo calculations. *Medical Physics*, 37(7):3809–3816.

Khandaker, M., Uddin, M., Kim, K., Lee, Y., and Kim, G. (2007). Measurement of cross-sections for the (p,xn) reactions in natural molybdenum. *Nuclear Instruments and Methods in Physics Research Section B: Beam Interactions with Materials and Atoms*, 262(2):171–181.

Knoll, G. (2000). *Radiation Detection and Measurement.* John Wiley & Sons.

Knowles, S. and Wu, A. (2012). Advances in immuno-positron emission tomography: Antibodies for molecular imaging in oncology. *Journal of Clinical Oncology*, 30(31):3884–3892.

Kobayashi, H., Wu, C., Kim, M.-K., Paik, C. H., Carrasquillo, J. A., and Brechbiel, M. W. (1999). Evaluation of the in vivo biodistribution of indium-111 and yttrium-88 labeled Dendrimer-1B4M-DTPA and its conjugation with anti-tac monoclonal antibody. *Bioconjugate Chemistry*, 10(1):103–111.

Koning, A. and Rochman, D. (2012). Modern nuclear data evaluation with the TALYS code system. *Nuclear Data Sheets*, 113(12):2841–2934.

Koppe, M. J., Bleichrodt, R. P., Soede, A. C., Verhofstad, A. A., Goldenberg, D. M., Oyen, W. J., and Boerman, O. C. (2004). Biodistribution and therapeutic efficacy of $^{125/131}I^{-}$, ^{186}Re-, $^{88/90}$Y-, or ^{177}Lu-labeled monoclonal antibody MN-14 to carcinoembryonic antigen in mice with small peritoneal metastases of colorectal origin. *Journal of Nuclear Medicine*, 45(7):1224–1232.

Krane, K. (1988). *Introductory Nuclear Physics*, chapter 11 and 15, pages 378–431 and 559–598. John Wiley & Sons.

La Gamma, A. and Nassiff, S. (1973). Excitation functions for deuteron-lnduced reactions on ^{89}Y. *Radiochimica Acta*, 19(4):161–162.

Lagunas-Solar, M. (1999). Accelerator production of ^{99m}Tc with proton beams and enriched ^{100}M targets. *IAEA-TECDOC-1065*, pages 87–112.

Lagunas-Solar, M. C., Kiefer, P. M., Carvacho, O. F., Lagunas, C. A., and Cha, Y. P. (1991). Cyclotron production of NCA ^{99m}Tc and ^{99}Mo. an alternative non-reactor supply source of instant ^{99m}Tc and ^{99}Mo/^{99m}Tc generators. *International Journal of Radiation Applications and Instrumentation. Part A. Applied Radiation and Isotopes*, 42(7):643–657.

Lebeda, O. and Pruszyński, M. (2010). New measurement of excitation functions for (p,x) reactions on ^{nat}mo with special regard to the formation of ^{95m}Tc, $^{96m+g}$Tc, ^{99m}Tc and ^{99}Mo. *Applied Radiation and Isotopes*, 68(12):2355–2365.

Lebeda, O., Štursa, J., and Ráliš, J. (2015). Experimental cross-sections of deuteron-induced reaction on ^{89}Y up to 20 MeV; comparison of ^{nat}Ti(d,x)^{48}V and ^{27}Al(d,x)^{24}Na monitor reactions. *Nuclear Instruments and Methods in Physics Research Section B: Beam Interactions with Materials and Atoms*, 360:118–128.

Lechtman, E., Chattopadhyay, N., Cai, Z., Mashouf, S., Reilly, R., and Pignol, J. (2011). Implications on clinical scenario of gold nanoparticle radiosensitization in regards to photon energy, nanoparticle size, concentration and location. *Physics in Medicine and Biology*, 56(15):4631–4647. cited By 75.

Levkovski, V. N. (1991). *Cross sections of medium mass nuclide activation (A=40–100) by medium energy protons and α-particles (E=10–50 MeV) (Experiment and Systematics)*. Inter-Vesti, Moscow.

Lieser, K. (2001). *Nuclear and Radiochemistry -Fundamentals and Applications-*, chapter 8, pages 126–146. Wiley-VCH.

Lilley, J. (2002). *Nuclear Physics -Principles and Applications-*, chapter 5, pages 129–150. John Wiley & Sons.

Loveland, W., Morrissey, D., and Seaborg, G. (2006). *Modern Nuclear Chemistry*, chapter 10 and 17. John Wiley & Sons.

Manenti, S., Holzwarth, U., Loriggiola, M., Gini, L., Esposito, J., Groppi, F., and Simonelli, F. (2014). The excitation functions of ^{100}Mo(p,x)^{99}Mo and ^{100}Mo(p,2n)^{99m}Tc. *Applied Radiation and Isotopes*, 94:344–348.

Meijs, W. E., Haisma, H. J., Klok, R. P., Van Gog, F. B., et al. (1997). Zirconium-labeled monoclonal antibodies and their distribution in tumor-bearing nude mice. *The Journal of Nuclear Medicine*, 38(1):112.

Meijs, W. E., Haisma, H. J., Schors, R. V. D., Wijbrandts, R., Oever, K. V. D., Klok, R. P., Pinedo, H. M., and Herscheid, J. D. (1996). A facile method for the labeling of proteins with zirconium isotopes. *Nuclear Medicine and Biology*, 23(4):439–448.

Menapace, E., Bonardi, M. L., Groppi, F., Persico, E., and Alfassi, Z. B. (2008). Experimental and calculated nuclear reaction data relevant to innovative production of medical radioisotopes. In *Proc. Intern. Conf. Nuclear Data for Science and Technology*, volume 2, page 1403.

Moeendarbari, S., Tekade, R., Mulgaonkar, A., Christensen, P., Ramezani, S., Hassan, G., Jiang, R., Öz, O. K., Hao, Y., and Sun, X. (2016). Theranostic nanoseeds for efficacious internal radiation therapy of unresectable solid tumors. *Scientific Reports*, 6:20614.

Mohr, P. J., Newell, D. B., and Taylor, B. N. (2015). CODATA Recommended Values of the Fundamental Physical Constants: 2014. *ArXiv e-prints*.

Mukhammedov, S., Vasidov, A., and Pardaev, E. (1984). Use of proton and deuteron activation methods of analysis in the determination of elements with Z > 42. *At.Energ.*, 56:50.

Mustafa, M. G., West, H. I., O'Brien, H., Lanier, R. G., Benhamou, M., and Tamura, T. (1988). Measurements and a direct-reaction – plus – Hauser-Feshbach analysis of ^{89}Y(p , n)^{89}Zr, ^{89}Y(p ,2 n)^{88}, and ^{89}Y(p , pn)^{88}Y reactions up to 40 mev. *Phys. Rev. C*, 38:1624–1637.

National Nuclear Data Center (2016). National Nuclear Data Center, information extracted from the NuDat 2 database. http://www.nndc.bnl.gov/nudat2/. Accessed: 2016-11-21.

Ngoune, R., Peters, A., von Elverfeldt, D., Winkler, K., and Pütz, G. (2016). Accumulating nanoparticles by EPR: A route of no return. *Journal of Controlled Release*, 238:58 – 70.

NNDC (2016). National nuclear data center, information extracted from the nudat 2 database, http://www.nndc.bnl.gov/nudat2/.

Nuclear Energy Agency (2010). The Supply of Medical Radioisotopes: Review of Potential Molybdenum-99/Technetium-99m Production Technologies.

Otuka, N. and Takács, S. (2015). Definitions of radioisotope thick target yields. *Radiochimica Acta*, 103(1):1–6.

Pignol, J. P., Keller, B., Rakovitch, E., Sankreacha, R., Easton, H., and Que, W. (2006). First report of a permanent breast ^{103}Pd seed implant as adjuvant radiation treatment for early–stage breast cancer. *International Journal of Radiation Oncology*Biology*Physics*, 64(1):176 –181.

Prete, G., Andrighetto, A., Manzolaro, M., Corradetti, S., Scarpa, D., Rossignoli, M., Monetti, A., Lollo, M., Calderolla, M., Vasquez, J., Zafiropoulos, D., Sarchiapone, L., Benini, D., Favaron, P., Rigato, M., Pegoraro, R., Maniero, D., Calabretta, L., Comunian, M., Maggiore, M., Lombardi, A., Piazza, L., Porcellato, A., Roncolato, C., Bisoffi, G., Pisent, A., Galatá , A., Giacchini, M., Bassato, G., Canella, S., Gramegna, F., Valiente, J., Bermudez, J., Mastinu, P., Esposito, J., Wyss, J., and Zanella, S. (2014). The SPES project at the INFN-Laboratori Nazionali di Legnaro. *EPJ Web of Conferences*, 66:11030.

Prokop, A. and Davidson, J. M. (2008). Nanovehicular intracellular delivery systems. *Journal of Pharmaceutical Sciences*, 97(9):3518 – 3590.

Qaim, S., Sudàr, S., Scholten, B., Koning, A., and Coenen, H. (2014). Evaluation of excitation functions of ^{100}Mo(p,d+pn)^{99}Mo and ^{100}Mo(p,2n)^{99m}Tc reactions: Estimation of long-lived Tc-impurity and its implication on the specific activity of cyclotron-produced ^{99m}Tc. *Applied Radiation and Isotopes*, 85(0):101–113.

Qaim, S. M. (2016). Nuclear data for production and medical application of radionuclides: Present status and future needs. *Nuclear Medicine and Biology*, pages –.

Rutherford, E. (1919). Collision of α particles with light atoms; 4, an anomalous effect in nitrogen. *Philosophical Magazine*, 37:581.

Scholten, B., Lambrecht, R. M., Cogneau, M., Ruiz, H. V., and Qaim, S. M. (1999). Excitation functions for the cyclotron production of ^{99m}Tc and ^{99}Mo. *Applied Radiation and Isotopes*, 51(1):69–80.

Semenova, E. and Finger, P. T. (2013). Palladium-103 radiation therapy for small choroidal melanoma. *Ophthalmology*, 120(11):2353–2357.

Sigmund, P. (2006). *Particle Penetration and Radiation Effects: General Aspects and Stopping of Swift Point Charges*, chapter 2 and 9. Springer.

Skyrme, D. (1967). The passage of charged particles through silicon. *Nuclear Instruments and Methods*, 57:61–73.

Stöcklin, G., Qaim, S., and Rösch, F. (1995). The impact of radioactivity on medicine metallic. *Radiochimica Acta*, 70(s1):249–272.

Takács, S., Szücs, Z., Tárkányi, F., Hermanne, A., and Sonckz, M. (2003). Evaluation of proton induced reactions on ^{100}Mo: New cross sections for production of ^{99m}Tc and ^{99}Mo. *Journal of Radioanalytical and Nuclear Chemistry*, 257(1):195–201.

Takahashi, K., Kohda, K., Miyahara, J., Kanemitsu, Y., Amitani, K., and Shionoya, S. (1984). Mechanism of photostimulated luminescence in BaFX: Eu 2+(X= Cl, Br) phosphors. *Journal of Luminescence*, 31:266–268.

Tárkányi, F., Ditrói, F., Hermanne, A., Takács, S., and Ignatyuk, A. (2012). Investigation of activation cross-sections of proton induced nuclear reactions on ^{nat}Mo up to 40 Mev: New data and evaluation. *Nuclear Instruments and Methods in Physics Research Section B: Beam Interactions with Materials and Atoms*, 280:45–73.

Tárkányi, F., Ditrói, F., Takács, S., Csikai, J., Mahunka, I., Uddin, M. S., Hagiwara, M., Baba, M., Ido, T., Hermanne, A., Sonck, M., Shubin, Y., and Dityuk, A. I. (2005). Excitation functions for production of ^{88}Zr and ^{88}Y by proton and deuteron irradiation of Mo, Nb, Zr, and Y. *AIP Conference Proceedings*, 769(1):1658–1661.

Tárkányi, F.and Takács, S., Gul, K., Hermanne, A., Mustafa, M., Nortier, M., Obložinský, P., Qaim, S., Scholten, B., Shubin, Y., and Youxiang, Z. (2001). Beam monitor reactions. In *Charged Particle Cross-Section Database for Medical Radioisotope Production, IAEA TECDOC 1211*, pages 49–152.

Tolmachev, V. and Stone-Elander, S. (2010). Radiolabelled proteins for positron emission tomography: Pros and cons of labelling methods. *Biochimica et Biophysica Acta - General Subjects*, 1800(5):487–510.

Tuli, J. K. (2011). *Nuclear Wallet Cards*. NNDC, Brookhaven National Laboratory, 8th edition edition.

Uddin, M. S., Baba, M., Hagiwara, M., Tárkányi, F., and Ditrói, F. (2007). Experimental determination of deuteron-induced activation cross sections of yttrium. *Radiochimica Acta*, 95(4):187–192.

Vértes, A., Nagy, S., Klencsár, Z., Lovas, G. R., and Rösch, F., editors (2011). *Handbook of Nuclear Chemistry*, volume 4, Radiochemistry and Radiopharmaceutical Chemistry in Life Sciences. Springer, second edition.

Von Seggern, H., Voigt, T., Knüpfer, W., and Lange, G. (1988). Physical model of photostimulated luminescence of x-ray irradiated bafbr: Eu2+. *Journal of applied physics*, 64(3):1405–1412.

Wang, M., Audi, G., Wapstra, A. H., Kondev, F. G., MacCormick, M., Xu, X., and Pfeiffer, B. (2012). The Ame2012 atomic mass evaluation. 36(12):1603.

Weisskopf, V. F. (1957). Nuclear physics. *Reviews of Modern Physics*, 29:174–181.

Wenrong, Z., Weixiang, Y., Xiaogang, H., and Hanlin, L. (1998). Excitation functions of reactions from d+Ti, d+Mo, p+Ti and p+Mo. In *COMMUNICATION OF NUCLEAR DATA PROGRESS No. 19*, pages 17–20. China Nuclear Data Center.

West, H. L. J., Mustafa, M. G., O'Brien, H., and Lanier, R. G. (1993). *Some Light-Ion Excitation-Function Measurements on Titanium, Yttrium, and Europium, and Associated Results*, chapter Some Excitation Functions of Proton and Deuteron Induced Reactions on ^{89}Y, pages 4–1–4–15.

Wolterbeek, B., Kloosterman, J. L., Lathouwers, D., Rohde, M., Winkelman, A., Frima, L., and Wols, F. (2014). What is wise in the production of ^{99}Mo? a comparison of eight possible production routes. *Journal of Radioanalytical and Nuclear Chemistry*, 302(2):773–779.

Yoshioka, Y. (2009). Current status and perspectives of brachytherapy for prostate cancer. *International Journal of Clinical Oncology*, 14(1):31–36.

Ziegler, J. F., Ziegler, M. D., and Biersack, J. P. (2010). SRIM - the stopping and range of ions in matter (2010). *Nuclear Instruments and Methods in Physics Research, Section B: Beam Interactions with Materials and Atoms*, 268(11-12):1818–1823.

List of Figures

1 Type and energy of corpuscular radiation versus the range in tissue. 3

1.1 Schematic diagram of a nuclear reaction. 9
1.2 Schematic view of a nuclear reaction in the lab and cm system. . . . 10
1.3 Forces and energy conditions when a charged projectile reacts 12
1.4 Example of probability function behavior for $E_{cb} < E_{th}$ and $E_{th} < E_{cb}$. 14
1.5 Conceptual view of the stages of a nuclear reaction. 15

2.1 Interaction between a particle beam and a target. 20
2.2 Examples of the production of ^{181}Re and ^{186g}Re. 23
2.3 A scattering event with momentum transfer $P_{\perp}$. 25
2.4 Trajectory of a moving ion past an electron. 25
2.5 Density of ionization along the particle path. 28
2.6 Intensity distribution or attenuation curve. 30
2.7 Range-energy curves for some charged particles in silicon 31
2.8 Graphical representation of the range-energy evaluation. 31
2.9 Example of calculated thick-target yield. 33
2.10 Efficiency curve using two calibration sources. 36

3.1 Ispra cyclotron building. 44
3.2 Ispra (Va) cyclotron. 45
3.3 Beam lines #1 e #2 of the Ispra cyclotron. 45
3.4 Irradiation chamber. 46
3.5 Faraday cup. 46
3.6 ARRONAX cyclotron building. 48
3.7 ARRONAX experimental vault, at the top right in Fig. 3.6 48
3.8 ARRONAX experimental irradiation station. 49

3.9 ARRONAX experimental irradiation station. 49
3.10 Perkin Elmer Cyclone. 50
3.11 An energy diagram of the excitation and photo-stimulated. 51
3.12 Beam "picture" of an almost distributed profile. 53
3.13 Beam "picture" of an almost Gaussian profile. 53

4.1 Excitation functions for ^{100}Mo(p,x)^{99}Mo nuclear reactions 60
4.2 Example of a γ-ray spectrum. The picture reports the emissions used to determine the activity. The other emissions belong to: ^{96}Nb/^{96}Tc, ^{95}Nb/^{95}Tc, ^{94}Nb/^{94}Tc, ^{93g}Tc produced by the isotopes of molybdenum contained in the target in a non-natural abundance and ^{99}Rh and ^{100}Rh produced by the impurities contained in the target. . . . 61
4.3 Excitation functions for ^{100}Mo(p,n)^{99m}Tc nuclear reactions 63
4.4 ^{99m}Tc experimental and fitted thin-target yield. 66
4.5 ^{99}Mo experimental and fitted thin-target yield. 66
4.6 Calculated Thick-Target Yields for the production of ^{99m}Tc 67
4.7 Calculated Thick-Target Yields for the production of ^{99}Mo 67
4.8 Excitation functions for ^{100}Mo(p,αn)^{96}Nb nuclear reactions. 70
4.9 Excitation functions for ^{100}Mo(p,α)^{97g,cum}Nb nuclear reactions. . . 70
4.10 Excitation functions for ^{100}Mo(p,n)^{99g}Tc nuclear reactions. 71

5.1 Excitation functions for ^{nat}Ti(p,x)^{48}V nuclear reactions. 75
5.2 Excitation functions for ^{27}Al(d,x)^{24}Na nuclear reactions. 76
5.3 Examples of γ-ray spectra, E = 17.9 MeV. 77
5.4 Excitation functions for ^{89}Y(d,2n)^{89}Zr nuclear reactions. 79
5.5 Excitation functions for ^{89}Y(d,3n)^{88}Zr nuclear reactions. 80
5.6 Excitation functions for ^{89}Y(d,x)^{88}Y nuclear reactions. 81

6.1 Excitation functions for ^{nat}Ti(p,x)^{48}V nuclear reactions. 86
6.2 Excitation functions for ^{27}Al(d,x)^{24}Na nuclear reactions. 87
6.3 Examples of γ-ray spectra for different targets and time. 88
6.4 Excitation functions for ^{103}Rh(d,2n)^{103}Pd nuclear reactions. 93
6.5 ^{103}Rh(d,2n)^{103}Pd experimental and fitted thin-target yield. 93
6.6 Thick-target yields for the production of ^{103}Pd 94
6.7 Excitation functions for ^{103}Rh(d,4n)^{101}Pd nuclear reaction. 95
6.8 Excitation functions for ^{103}Rh(d,x)^{102m}Rh nuclear reactions. 96
6.9 Excitation functions for ^{103}Rh(d,x)^{102g}Rh nuclear reactions. 96
6.10 Excitation functions for ^{103}Rh(d,x)^{101m,cum}Rh nuclear reactions. . . 97
6.11 Excitation functions for ^{103}Rh(d,x)^{101g}Rh nuclear reactions. 98

6.12 Excitation functions for ^{103}Rh(d,x)^{100g,cum}Rh nuclear reactions. . . 99
6.13 Excitation functions for ^{103}Rh(d,2p)^{103}Ru nuclear reactions. 99
6.14 EMPIRE-3.2.2: ^{103}Rh(d,x)$^{\bullet}$Pd excitation functions 100
6.15 EMPIRE-3.2.2: ratio on the ^{103}Pd nuclei on all the isotopes 100

List of Tables

3.1 Characteristics of the JRC Cyclotron extracted beam. 44
3.2 Characteristics of the ARRONAX Cyclotron extracted beam. 47

4.1 Decay data [Browne and Tuli, 2011] of ^{99m}Tc and ^{99}Mo radionuclides and contributing reactions. Branching ratio (BR) is reported from ICRP [2008]. Energy threshold (E_{th}) evaluation is based on Wang et al. [2012] 58
4.2 The ^{100}Mo(p,2n)^{99m}Tc and ^{100}Mo(p,x)^{99}Mo experimental cross sections 59
4.3 Relevant data: "–" is for an information not explicitly reported in the previous paper, "NA" is for the information not available, CF1 is the correction factor for the interference of the 140.511 keV peak (✓) and CF2 is the correction factor for indirect production of ^{99m}Tc as a result of ^{99}Mo decay, post irradiation (✓) or both during and post irradiation (✓✓). In the last two columns the are the energy and the maximum cross section. 64
4.4 ^{99m}Tc activity [GBq/100μA] for E = 14 MeV and ΔE = 5 MeV . . 68
4.5 Decay data [Browne and Tuli, 2011, NNDC, 2016] of ^{99g}Tc, ^{96}Nb and ^{97g}Nb radionuclides and contributing reactions. Branching ratio (BR) is reported from ICRP [2008]. Energy threshold (E_{th}) evaluation is based on Wang et al. [2012] 68
4.6 The ^{100}Mo(p,αn)^{96}Nb, ^{100}Mo(p,α experimental cross sections 69

5.1 Decay data [Firestone et al., 1999] of Zr and Y radionuclides and contributing reactions. The E_{th} evaluation is based on the mass defects of Wang et al. [2012]. 78

5.2 ^{89}Y(d,xn)^{89,88}Zr and ^{89}Y(d,x)^{88}Y experimental cross-sections 78

6.1 Decay data [Firestone et al., 1999] of Pd, Rh and Ru radionuclides and contributing reactions. The E_{th} evaluation is based on the mass defects of Wang et al. [2012]. 90
6.2 ^{103}Rh(d,xn)^{103,101}Pd, ^{103}Rh(d,2p)^{103}Ru and ^{103}Rh(d,p5n)^{100g}Rh experimental cross-sections 91
6.3 ^{103}Rh(d,pxn)$^{\bullet}$Rh experimental cross-sections 92